Transfer of Graphene under Ultra-High Vacuum

Darius Constantin MERK

École
polytechnique
fédérale
de Lausanne

2022

Acknowledgements

First and foremost, I would like to thank Harald Brune for the opportunity of working in his research group. These 4 years have had their ups and downs, but I am delighted to have been in this group. No less important, I am extremely grateful towards Stefano Rusponi, who through his wise advice and help, always helped me to solve problems I faced throughout my work. Just as importantly, Marina Pivetta and Francois Patthey, thank you for all the advice and expertise. All of you have contributed through your insightful feedback to sharpen my thinking and develop a scientific approach.

Thank you to all my fellow lab mates for their advice and help as well as making the tougher days more pleasant and making it all fun; Sébastien Reynaud, Edgar Fernandez, Alberto Curcella, Johannes Schwenk, Clément Soulard, Jean-Guillaume de Groot, Dante Sblendorio, Boris Sorokin, Tobias Bilgeri, Simone Borroni, Aparajita Singha, Fabio Donati, Romana Baltic and Oreste De Luca. I wish you all the best in your future research and work. For their help in growing and providing graphene, I'd also like to thank Arnaud Magrez, Florian Monnier and Anna Kukolova.

Messieurs des ateliers de mécanique et d'électronique, merci pour votre amabilité, votre excellent travail et votre bonne humeur. Merci Claude pour tout ce que tu as fait, tu as toujours trouvé une solution pour les problèmes que je t'ai demandé de m'aider à résoudre. Ton côté méticuleux m'a appris a faire les choses avec soin (au mieux). Mesdames Nathalie Guex, Carole Pascalon, Anh Eymann et Chantale Roulin, je vous ai toujours vues avec le sourire et ai toujours apprécié votre gentillesse, bonne humeur et votre travail, merci.

Finalement, ces remerciements ne seraient pas complets sans reconnaître le soutien et la motivation que m'ont apporté mes amis et ma famille, qui m'ont permis de mener jusqu'au bout l'épreuve de la thèse en Physique. Merci à tous.

Lausanne, October 29, 2021 Darius Merk

Abstract

This thesis reports on a novel method for graphene transfer that is fully UHV compatible, which has remained a challenge for a long time due to the necessity of supporting graphene for transfer and most often requiring supporting layer removal post-transfer. Our graphene transfer method is based on the wafer-bonding approach, where graphene is stamped onto a target surface, from a support to which it is weakly bound. We use a bilayer of graphene supported by a teflon tape for the low adhesion between graphene layers and the flexibility of teflon tape to allow adaptability to the target surface.

We demonstrate successful transfer onto Cu(100) and Ir(111) single crystal surfaces as well as on gr/Ir(111), thus forming a (partial) graphene bilayer on Ir(111). For *in-situ* characterization, we use Auger electron spectroscopy and STM. Auger measurements confirm that we are able to transfer an average 0.8-0.9 ML of carbon, by comparison to CVD grown samples. After transfer onto Ir(111), we show that by annealing to 1000 ℃, we are able to observe by STM the characteristic moiré pattern formed by CVD grown graphene on Ir(111). Auger spectra show that the graphene-Iridium interaction undergoes a change from physisorption to chemisorption upon annealing. XAS and Raman spectroscopy demonstrate that the annealing step taken post transfer to observe the moiré by STM is only necessary to induce a change in interaction strength but not to heal graphene defects, to increase its domain size, or to make it flat. After transfer onto Cu(100), Raman spectra show that the transferred graphene is of the same quality as the CVD grown graphene before transfer, without further annealing. Comparison of synchrotron based high resolution XAS spectra of transferred gr/Ir(111) to CVD grown samples confirms that the transferred graphene is flat on top of the Ir(111) crystal surface.

This enables sample and device fabrication, usually hampered by impurities, to be carried out in UHV leading to fully reproducible results. Clean twisted bilayer graphene samples can be made and studied in UHV. Further, surface science can be extended to the third dimension, by capping layers and continuing growth, etc., all under clean conditions.

Key words: Graphene, graphene transfer, ultrahigh vacuum, graphene moiré, scanning tunneling microscopy, Auger electron spectroscopy, Raman spectroscopy, x-ray absorption spectroscopy

Résumé

Cette thèse porte sur une nouvelle méthode de transfert de graphène entièrement compatible avec l'UHV, ce qui est resté un défi pendant longtemps en raison de la nécessité de supporter le graphène pour le transfert et le plus souvent nécessitant l'enlèvement de la couche de support suite au transfert. Notre méthode de transfert de graphène est basée sur l'approche wafer-bonding, où le graphène est pressé sur une surface cible, à partir d'un support auquel il est faiblement lié. Nous utilisons une bicouche de graphène soutenue par un ruban de téflon pour la faible adhésion des deux couches de graphène et pour la flexibilité du ruban de téflon qui permet de s'adapter à la surface cible.

Nous démontrons un transfert réussi sur des surfaces monocristallines de Cu(100) et Ir(111) ainsi que sur gr/Ir(111), formant ainsi une bicouche (partielle) de graphène sur Ir(111). Pour la caractérisation *in-situ*, nous utilisons de la spectroscopie d'électrons Auger ainsi que de la microscopie à effet tunnel. Les résultats Auger confirment que nous sommes capables de transférer une moyenne de 0.8-0.9 ML de carbone, par comparaison avec les échantillons obtenus par CVD. Après transfert sur Ir(111), nous montrons qu'en recuisant à 1000 °C, nous avons pu observer par STM le motif moiré caractéristique formé par le graphène obtenu par dépôt chimique en phase vapeur sur Ir(111). Les spectres Auger montrent que l'interaction graphène-Iridium subit un changement de physisorption à chimisorption lors du recuit. Les spectroscopies d'absorption des rayons X (XAS) et Raman démontrent que l'étape de recuit prise après le transfert pour observer le moiré par STM est seulement nécessaire pour induire un changement dans la force d'interaction, mais pas pour réparer les défauts du graphène, pour augmenter la taille des domaines ou pour le rendre plat. Après le transfert sur Cu(100), les spectres Raman montrent que le graphène transféré est de la même qualité que le graphène obtenu par CVD avant le transfert sans recuit. La comparaison des spectres XAS haute résolution, obtenus au synchrotron, des échantillons de gr/Ir(111) transférés avec ceux obtenus par CVD confirme que le graphène transféré est plat sur la surface du cristal Ir(111).

Ainsi, la fabrication d'échantillons et de dispositifs, généralement entravée par les impuretés, peut être effectuée dans l'UHV, ce qui permet d'obtenir des résultats entièrement reproductibles. Des échantillons propres de graphène bicouche torsadé peuvent être fabriqués et étudiés sous UHV. De plus, la science des surfaces peut être étendue à la troisième dimension, en recouvrant les couches et en poursuivant la croissance, etc., le tout dans des conditions propres.

Résumé

Mots clés : Graphène, transfert de graphène, ultravide, moiré, microscope à effet tunnel, spectroscopie d'électrons Auger, spectroscopie Raman, spectroscopie d'absorption des rayons X

Contents

Contents

List of Figures

List of Figures

2

List of Tables

Frequently Used Abbreviations

a-C	Amorphous carbon
AES	Auger Electron Spectroscopy
BLG	Bilayer Graphene
CVD	Chemical Vapor Deposition
DI water	Deionized water
HOPG	Highly Oriented Pyrolytic Graphite
LEED	Low-Energy Electron Diffraction
MBE	Molecular Beam Epitaxy
MLG	Monolayer Graphene
PDMS	Polydimethylsiloxane
PMMA	Polymethyl methacrylate
PTFE	Polytetrafluoroethylene (Teflon)
PVA	Polyvinyl Alcohol
RT	Room Temperature
SiC	Silicon Carbide
STM	Scanning Tunneling Microscope
UHV	Ultra High Vacuum
vdW	van der Waals
XAS	X-ray Absorption Spectroscopy

Frequently Used Abbreviations

Throughout this thesis we will refer to the following chemical elements :

Argon (Ar), Carbon (C), Copper (Cu), Iridium (Ir), Iron (Fe), Nickel (Ni), Oxygen (O), Platinum (Pt), Silicon (Si) and Tungsten (W).

And the following molecules and compounds :

Alumina (Al_2O_3), Ethylene (C_2H_4), Methane (CH_4), Iron Chloride ($FeCl_3$), PDMS ((C_2H_6OSi)$_x$), PVA((C_2H_4O)$_x$), Sodium Hydroxide (NaOH) and Teflon ((C_2F_4)$_x$).

Introduction

The history of graphene dates back to no less than 160 years ago, in 1859, when Sir Benjamin Collins Brodie described the lamellar structural property of reduced graphite oxide. His observations were the first to reveal the stacking of "minute brilliant plates" forming graphite [1]. It was however not before 1947 that a theoretical study of the electrical properties of graphene, "a single graphite sheet", was introduced by P.R. Wallace [2].

In the 2000s, the semiconductor industry, traditionally based on silicon, was reaching a limit in performance. In the quest to increase the performance, new materials whose properties could be controlled by an electric field were sought. Chasing this goal in 2004, two Physicists, Geim and Novoselov developed a simple method to isolate monocrystalline graphitic films with a thickness of a few atoms from graphite using mechanical cleavage [3]. They were the first to report on this simple isolation process involving pressing a piece of scotch tape on the surface of a lump of graphite and exfoliating by lifting the tape. Shortly after, they were able to isolate a single graphene layer using the same procedure and using a combination of optical microscopy, scanning electron microscopy and atomic-force microscopy [4]. In 2010, thanks to their work demonstrating the exceptional properties of graphene, they were awarded the Nobel prize in Physics "*for groundbreaking experiments regarding the two-dimensional material graphene*".

The simplicity of the method demonstrated by Geim and Novoselov was revolutionary and unlocked a worldwide frenzy of graphene-related research. Among other properties, this new wonder material conducts electricity better than copper, is almost perfectly transparent (2 % absorption) and is 200 times stronger than steel while six times lighter. The delamination process, although simple, yields small samples and is time consuming, making it unsuited for commercial mass-production. More scalable processes for graphene production including liquid-phase exfoliation [5,6], synthesis on SiC [7] or chemical vapor deposition (CVD) and many others [8] have been introduced, each with its own advantages and drawbacks [9].

The most commonly used graphene synthesis method is CVD growth, which has rapidly evolved, yielding large-area (wafer-scale single crystal graphene on Ge [10]) and high quality graphene on catalytic metallic substrates such as nickel [11], copper [12] or

iridium [13, 14]. The facile self-limited process of graphene growth on polycrystalline Cu by CVD has been widely used, with graphene areas limited only by the size of the polycrystalline Cu substrate and of the reactor. The quality of the graphene obtained with this method strongly depends on the Cu substrate roughness and monocrystalline domains as well as on the growth parameters [15].

The interest in graphene was initially motivated by its interesting electronic structure and its unusual transport properties, and a lot of effort has been put into transforming the zero bandgap semiconducting behaviour of freestanding graphene into a gapped semiconductor, similarly to Si, that can be integrated in electronics devices [16–18].

Over time, graphene has found many additional applications [19]: in electronics [20] for instance, for flexible touchscreens [21], for organic light emitting diodes (OLEDs) [22] or flexible solar cells [23]. Alternatively, the moiré pattern formed by it on single crystal metal surfaces has been used as a template for the self-assembly of nanostructures [24–30] or graphene has been used as a decoupling layer for the realization of single atom magnets [31–33].

Applications may also involve the transfer of graphene on a surface where it does not grow, or stacking of graphene layers to produce multilayered nanostructures such as van der Waals homo [34, 35] and heterostructures [36–38]. The advancement of fabrication methods enabled the control of the relative twist angle between successive layers of 2D materials and opened up the field of twistronics [39]. In 2018, P. Jarillo-Herrero & al. demonstrated that at the predicted magic angle $\theta_M \approx 1.1°$ between two layers, twisted bilayer graphene (tBLG) becomes a superconductor [40], tBLG has been shown to be characterized by flat bands and to exhibit van Hove singularities [34, 35]. The fabrication of large areas of tBLG remains a challenge; small twist angle tBLG can only be obtained by transfer of a single graphene layer on top of another graphene layer either grown by CVD or previously transferred [41–43].

Other applications can be imagined. For example, in the field of magnetic data storage, the thermal stability of the magnetization of the nanomagnets used for the bits is a challenge posed by the continuous demand for increased areal density. Thermal stability of the magnetization is limited by the so-called blocking temperature (T_b) above which the magnetization vector fluctuates randomly. Blocking temperatures of 40 K have been reached for superparamagnetic islands of Co on Au(788)Co/Au(788) [44]. Co islands on Au(11,12,12) have a blocking temperature of 85 K [45], and surrounding the Co with Fe increases the blocking temperature to 105 K [46].

In order to increase the magnetic stability (blocking temperature) of these systems, magnetic structures can be extended in the third dimension. We refer to these structures as magnetic pillars. Attempts have been made to form magnetic pillars, by stacking of consecutive layers of Au(111) with Co islands on top, which showed limited spatial order

(hundreds of nm) [47], or by growing graphene on top of an IrNi superlattice of clusters grown on a gr/Ir(111) moiré template by *in-situ* decomposition at high temperature of ethylene, which only yielded small patches of graphene [48]. An alternative to *in-situ* growth consists of transferring a sheet of graphene onto such a superlattice of clusters, followed by redeposition of clusters and so on, forming a mille-feuille structure of magnetic clusters as depicted in figure 1. In addition to opening the possibility of growing pillars, this would also allow one to cover samples, protecting them from atmospheric conditions, acting as a capping layer.
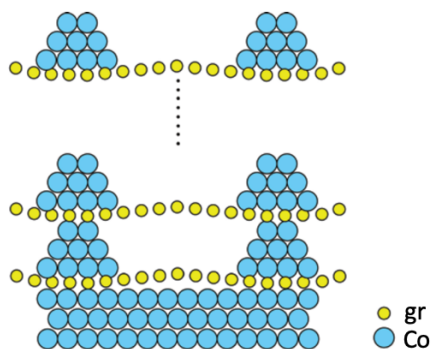
Figure 1 – Schematic illustration of "Mille-feuille" stacking

To enable advances in the multiple applications of graphene, a multitude of graphene transfer methods from the growth substrate to the target surface have been developed [49, 50]. These range from the mechanical exfoliation of graphene from its growth substrate to the chemical etching of the substrate under the graphene. Most of these transfer techniques, however, require the use of a supporting layer to prevent the atomically-thin graphene layer to break or roll up. The most common transfer technique involves covering the CVD grown graphene with Polymethyl methacrylate (PMMA) and subsequently etching the metallic growth substrate, leaving behind graphene supported on PMMA, which is then transferred to a target before removing PMMA by immersion in hot acetone [51].

Alternatively, graphene transfer from a polycrystalline Pt growth substrate has been demonstrated by electrochemical bubbling [52]. Not only does this technique avoid contamination of the graphene with metallic atoms that remain of the substrate etching, but the graphene grown on a Pt(111) substrate is of high quality [53] and the growth substrate can be reused since the PMMA-supported graphene is peeled off the Pt with hydrogen bubbles formed by electrolysis in an NaOH solution [52]. These transfer methods are known as "wet transfers" because the process of isolating graphene and its supporting layer from the growth substrate is done in a liquid environment.

Dry transfer procedures do not require an aqueous environment for graphene isolation. Instead, graphene is covered with a supporting layer and delaminated from its growth substrate in air or in a controlled atmosphere. One of these transfer techniques uses Polyvinyl alcohol (PVA) as a supporting layer and a Polydimethylsiloxane (PDMS) stamp for graphene/PVA delamination from the growth substrate [54]. This procedure does not require etching of the metallic substrate, making the transferred graphene, in the ideal case of a perfect detachment, free of metal ions. The PDMS stamp is then detached after the transfer from the PVA by heat activation. The PVA, however, must be removed by immersion in hot water after transfer.

In this thesis, we present a method to deposit large areas (up to 5 x 5 mm^2) of high quality (structural defect and adsorbate free) graphene in Ultra-high vacuum (UHV) onto a desidered target surface without any further steps of support removal. We use bilayer graphene (BLG) supported on teflon (PTFE) as source wafer for the transfer. The weak van-der-Waals interaction between the two graphene layers [55] compared to the interaction of graphene with the target wafer (or single crystal sample) enables the transfer of exclusively the top layer of BLG.

The first chapter of this thesis focuses on the main properties of graphene as well as synthesis and transfer methods. We first describe graphene's atomic structure before introducing electronic and phononic properties and the most commonly observed defects. These properties allow us to probe the presence and quality of graphene through experimental methods which we describe in the second chapter. We then present the most common graphene synthesis and transfer methods before finally giving a brief description of multilayer graphene systems and their different configurations.

The second chapter covers all the characterization and experimental methods employed in our work. We first give a description of Raman spectroscopy and describe the origin of the main Raman peaks that characterize graphene. The principle of synchrotron based x-ray absorption spectroscopy is then explained and our experimental setup is described; a typical spectrum obtained for graphene is shown. Scanning tunneling microscopy (STM) and Auger electron spectroscopy (AES), both of which are carried out *in-situ*, are explained and a typical STM image of the gr/Ir(111) moiré is shown with the corresponding Auger spectrum. The combination of all these methods enables full characterization of graphene after growth and after transfer. Our experimental setup is then presented, with emphasis on the components vital to the transfer procedure. Finally the graphene growth techniques employed in our work are presented.

In the third chapter, we describe in detail each of the transfer procedures that were attempted towards reaching our UHV-compatible transfer goal. Each procedure we worked on led to a conclusion which allowed us to move onto the next step. At the end of this chapter, we present a PVA-assisted transfer procedure which was our first transfer of graphene within UHV, but which required taking the sample out of UHV to remove the PVA support layer.

In the fourth and final chapter, we describe our UHV-compatible teflon-assisted graphene transfer method. Gr/Ir(111) samples obtained by our transfer method are characterized *in-situ* by AES and STM. We carried out XAS measurements at the EPFL-PSI XTreme end-station. Graphene was transferred to Cu(100) in UHV and Raman spectra were acquired in air post-transfer. To conclude, we demonstrate the versatility of our transfer method by transferring graphene in UHV onto a gr/Ir(111) sample, making BLG/Ir(111).

1 Graphene properties, synthesis and transfer

The first part of this chapter provides the theoretical background necessary to understand the experimental data obtained with the different characterization techniques used in our work; the structural, electronic and phononic properties as well as the most common defects in graphene are described in section 1.1.

The second part of this chapter focuses on the most common techniques for monolayer graphene (MLG) production and transfer (sections 1.2 and 1.3). Multilayer graphene production techniques are described in section 1.4 with emphasis on BLG. These production and transfer methods provide the foundation for the successful transfer method we present in this thesis.

1.1 Graphene atomic structure, electronic and phononic properties

1.1.1 Atomic structure

Graphene is a single layer of sp^2-bonded carbon atoms arranged in a honeycomb lattice with a lattice constant of 2.462 Å [56]. There are two triangular sublattices composed each of (non-equivalent) atoms A and B respectively (see fig. 1.1). The lattice vectors $\mathbf{a}_1$ and $\mathbf{a}_2$ are defined as :

$$\boldsymbol{a}_1 = \sqrt{3}a\boldsymbol{e}_x, \quad \boldsymbol{a}_2 = \frac{a}{2}\left(-\sqrt{3}\boldsymbol{e}_x + 3\boldsymbol{e}_y\right) \tag{1.1}$$

where $a = 1.42$ Å is the C-C bond length.

The unit cell of graphene (highlighted in gray in figure 1.1) contains two atoms and although graphene is a 2D material, the thickness of a graphene monolayer is considered to be the same as the interlayer spacing in graphite, $d = 3.35$Å [57]. This definition of thickness is however not unequivocal and is related to the spatial extension of the electronic
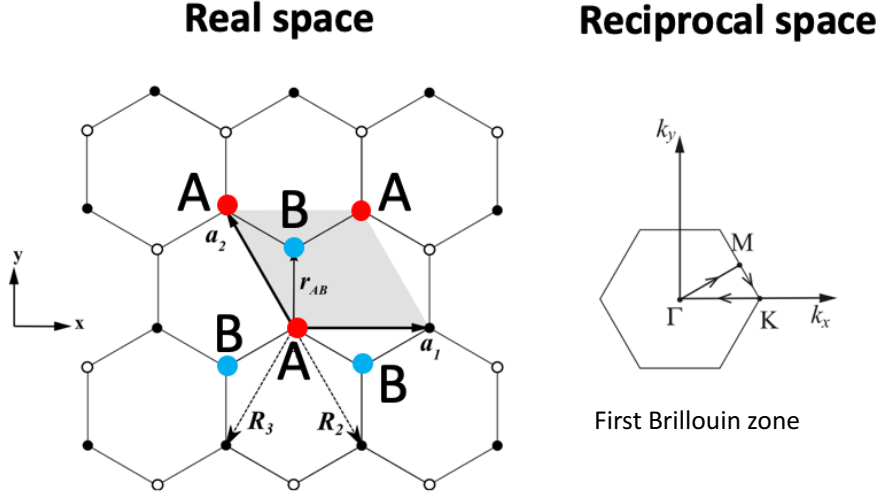
Figure 1.1 – Graphene atomic structure: (left) in real space, and (right) in reciprocal space. Each carbon atom binds to 3 carbon neighbors, with $r_{AB} = a = 1.42$ Å and $||a_1|| = ||a_2|| = 2.46$ Å. Adapted from [60].

clouds. Graphite is part of the category of van der Waals materials, characterized by strong interatomic in-plane bonds and by weak vdW interactions between layers. Graphene is accordingly also a vdW material.

The vdW force is a distance-dependent electrostatic interaction between polar molecules (the fluctuations in the polarization induced by the electron motions in non-polar molecules also induce this interaction, referred to as the London-van der Waals interaction). The vdW energy potential can be described by the Lennard-Jones potential [58, 59] with a minimum energy at an interlayer distance $d = 0.335$ nm in the case of graphite. It is not the result of a chemical bond and is therefore weak.

Each carbon atom has 6 electrons in total, 2 in the 1s inner-shell and 4 valence electrons which form bonds with neighboring atoms in graphene. All carbon atoms are sp^2 hybridized, meaning that the 2s, 2p$_x$ and 2p$_y$ orbitals form 3 identical lobes in one plane (yellow lobes in figure 1.2). These sp^2 orbitals form strong covalent bonds (σ bonds) with the sp^2 orbitals of neighboring carbon atoms, giving graphene high stability and tensile strength. The fourth outer-shell electron occupies the 2p$_z$ orbital (π orbital) above and below the plane containing the carbon atoms (blue lobes in figure 1.2). These π orbitals merge with their neighboring π orbitals creating a "plane" of electrons above and under the graphene layer. These free electrons enable graphene to absorb light by photon absorption, such that each layer of graphene absorbs 2.3 % of light in the visible range. The absorption increases linearly with increasing numbers of layers [61]. In some cases, this property can be used for rough determination of layer number.
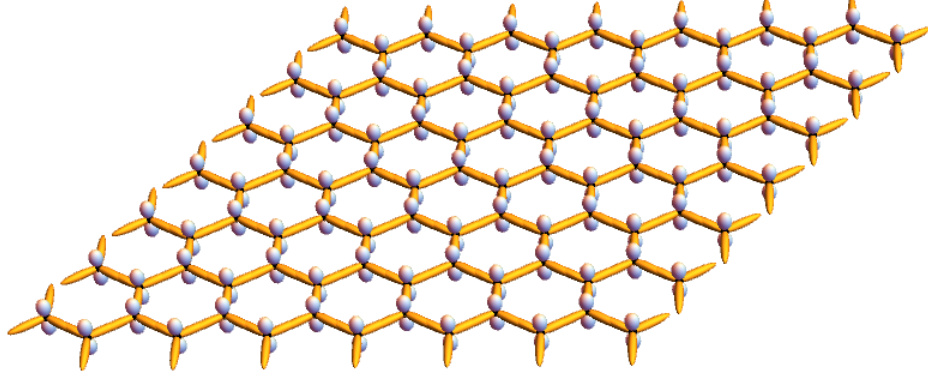
Figure 1.2 – Representation of the honeycomb structure with electronic orbitals. In-plane C-C sp^2 σ bonds in yellow and out of plane p$_z$ orbitals (π electrons) in blue.

1.1.2 Electronic properties (band structure)

Although the band structure of graphene is not indispensable for this work, the (approximated) energy dispersion relation is presented for completeness of the description of graphene. As the in-plane covalent bonds have fully filled valence bands they are disregarded for the calculation and only the p_z out-of-plane electron orbitals, described by the wave function ϕ_p obeying Schrödinger's equation with energy ϵ_p are considered. The atomic orbitals ϕ_p are eigenfunctions of the hamiltonian H_{at} of a single isolated atom.

$$H_{at}\left|\phi_p\right\rangle = \varepsilon_p\left|\phi_p\right\rangle \quad \text{with} \quad \left\langle\phi_p\,|\,\phi_p\right\rangle = 1 \tag{1.2}$$

To determine the energy dispersion relation, the two non-equivalent atoms A and B are considered and a separate Bloch wave function is defined for each of the p_z electron orbitals, respectively $\phi_A^{\mathbf{k}}$ and $\phi_B^{\mathbf{k}}$, where $\mathbf{k}$ is the wave vector of the electron :

$$\begin{cases} \phi_A^{\mathbf{k}}(\mathbf{r}) = \frac{1}{\sqrt{N}}\sum_R e^{i\mathbf{k}R}\phi_p(\mathbf{r}-\mathbf{R}) & \left\langle\phi_A^{\mathbf{k}}\,|\,\phi_A^{\mathbf{k}}\right\rangle = \left\langle\phi_B^{\mathbf{k}}\,|\,\phi_B^{\mathbf{k}}\right\rangle = 1 \\ \phi_B^{\mathbf{k}}(\mathbf{r}) = \frac{1}{\sqrt{N}}\sum_R e^{i\mathbf{k}(\mathbf{R}+\mathbf{r}_{AB})}\phi_p(\mathbf{r}-\mathbf{r_{AB}}-\mathbf{R}) & \left\langle\phi_A^{\mathbf{k}}\,|\,\phi_B^{\mathbf{k}}\right\rangle = 0 \end{cases} \tag{1.3}$$

The total wave function of the system is the linear combination of both wave functions :

$$\psi^{\mathbf{k}}(\mathbf{r}) = a^{\mathbf{k}}\phi_A^{\mathbf{k}}(\mathbf{r}) + b^{\mathbf{k}}\phi_B^{\mathbf{k}}(\mathbf{r}) \tag{1.4}$$

This wave function is the solution of the Schrödinger equation where in the basis defined by ϕ_A and ϕ_B the Hamiltonian is given by :

$$H^{\mathbf{k}} = \begin{bmatrix} \left\langle\phi_A^{\mathbf{k}}|H|\phi_A^{\mathbf{k}}\right\rangle & \left\langle\phi_A^{\mathbf{k}}|H|\phi_B^{\mathbf{k}}\right\rangle \\ \left\langle\phi_B^{\mathbf{k}}|H|\phi_A^{\mathbf{k}}\right\rangle & \left\langle\phi_B^{\mathbf{k}}|H|\phi_B^{\mathbf{k}}\right\rangle \end{bmatrix} \tag{1.5}$$
$$H = H_{\text{at}} + \Delta V$$

Where ΔV represents the electrostatic potential due to ion cores on adjacent atomic sites. In order to solve this hamiltonian, the tight binding model introduces hypotheses which allow one to obtain the energy eigenstates $E(\mathbf{k})$. It is first considered that for tightly bound atoms, the crystal field integral is neglected (see eqn. 1.6 (a)). Second, the transfer (hopping) integral γ terms are non-zero only for first neighbors (see eqn. 1.6 (b)) and finally, the p orbitals on different sites do not overlap (see eqn. 1.6 (c)).

$$(a) \quad \langle \phi_p | \Delta V | \phi_p \rangle = 0 \quad \rightarrow \quad \int \phi_p^*(\mathbf{r}) \Delta V \phi_p(\mathbf{r}) d\mathbf{r} = 0$$

$$(b) \quad \begin{cases} \gamma(\mathbf{r}) = \int \phi_p^*(\mathbf{r}) \Delta V \phi_p (\mathbf{r} - \mathbf{r}') \, d\mathbf{r} = -\gamma \text{ nearest neighbors} \\ \gamma(\mathbf{r}) = 0 \qquad\qquad\qquad\qquad\qquad \text{all other sites} \end{cases} \qquad (1.6)$$

$$(c) \quad \int \phi_p^*(\mathbf{r}) \phi_p(\mathbf{r} - \mathbf{x}) d\mathbf{r} = 0 \text{ for } \mathbf{x} \neq \mathbf{0}$$

The first two conditions imply that the diagonal terms of the matrix defined previously are equal $\varepsilon_A^k = \varepsilon_B^k = \varepsilon_p$ (they are equal because atoms A and B are chemically identical). This term represents the energy of the p_z orbital in an isolated atom. The transfer integral $\Delta^{\mathbf{k}}$ in the case of nearest neighbors reduces to

$$\Delta^{\mathbf{k}} = -\gamma \sum_{d_i} e^{i\mathbf{k}d_i} = -\gamma \left(e^{i\frac{k_y a}{\sqrt{3}}} + 2 e^{-i\frac{k_y a}{2\sqrt{3}}} \cos\left(\frac{k_x a}{2}\right) \right) \qquad (1.7)$$

Schrödinger's equation can then be rewritten as

$$\begin{bmatrix} \varepsilon_A^k & \Delta^k \\ \Delta^{k*} & \varepsilon_B^k \end{bmatrix} \begin{pmatrix} a^k \\ b^k \end{pmatrix} = E(\mathbf{k}) \begin{pmatrix} a^{\mathbf{k}} \\ b^{\mathbf{k}} \end{pmatrix} \qquad (1.8)$$

The solutions to this system give the electronic band structure of graphene.

$$E_\pm(\mathbf{k}) = \varepsilon_p \pm \gamma \sqrt{1 + 4\cos^2 \frac{k_x a}{2} + 4\cos \frac{k_x a}{2} \cos \frac{k_y a\sqrt{3}}{2}} \qquad (1.9)$$

This solution is plotted in figure 1.3 for a Fermi energy of 0 ($\varepsilon_p = 0$) and a hopping parameter $\gamma = 3$ eV [62]. Figure 1.3 (b) is the contour plot of the band structure of graphene and inequivalent Dirac points K and $K' = -K$ are marked.

The band with positive energy values (above the Fermi energy of 0 eV, in yellow in fig. 1.3 (a)) is referred to as the anti-bonding π^* band and the bonding π band corresponds to the negative energies (in blue in fig. 1.3 (a)). With one p_z electron per atom, the
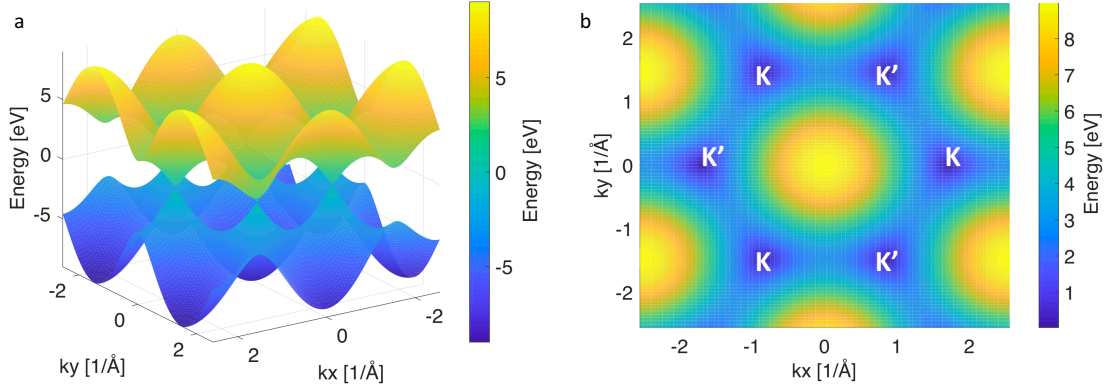
Figure 1.3 – Graphene tight binding electronic band structure (a) in 3 dimensions and (b) contour plot of the band structure of graphene with inequivalent K and K' Dirac points highlighted.

bonding band is fully occupied, while the anti-bonding band is entirely empty. These two bands touch at the K and K' points, making graphene behave like a zero band-gap semiconductor (or semi-metallic).

1.1.3 Phononic dispersion relation

The phonon dispersion relation of graphene is crucial to understand its Raman signature. Because there are two atoms in the first Brillouin zone, there are six phonon branches, three of which are acoustic phonons (A), originating from the Γ-point of the Brillouin zone, and three are optical phonons (O). Of these six, four are in-plane (i) phonon branches and two are out-of-plane (o) branches. The in-plane modes are either longitudinal (L) or transverse (T), depending on whether the direction of the atomic motion is along or perpendicular to the carbon-carbon bonds, respectively. These branches are labelled in figure 1.4, which shows the DFT-calculated phonon dispersion relation [63]. The analytical expression of the phonon dispersion relation of graphene can be obtained within the framework of the Born-von-Karman model considering interactions between first and second nearest neighbors [64], which we do not elaborate on.

Zone-center phonons are characterized by zero momentum in contrast to the non-zero momentum K and M (high symmetry points) phonons. Those responsible for the main Raman bands of graphene are highlighted and labelled in figure 1.4. The vibrational modes leading to the Raman spectrum of graphene are described in detail in section 2.1.1.
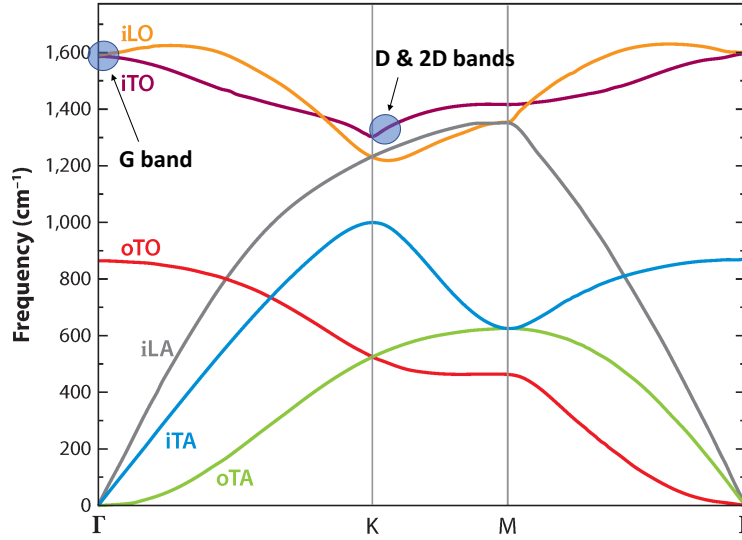
Figure 1.4 – Calculated phonon dispersion relation of graphene. Graphene has six phonon branches, four out-of-plane (o) modes and two in-plane (i) modes. The main phonons that can be excited for Raman transitions are highlighted (G band in zone-center, D and 2D bands in zone-edge). Adapted from [65].

1.1.4   Defects in CVD grown graphene

In the theoretical atomic structure of graphene presented previously, defects in the lattice were not considered, but are inevitable in real graphene samples due to the growth processes, transfer methods and adsorbates. In general, defects in three-dimensional crystals can be intrinsic, when the breaking of the symmetry is caused by an atom of the same nature as the bulk, or extrinsic when due to an impurity. These terms apply to graphene although it is a 2D-material and can be further classified by their dimensions (0D, 1D, 2D). For graphene, typical point defects (0D) include single vacancies or interstitial atoms whereas dislocations are typical line defects (1D) [66–68]. This section focuses on the most common defects which appear during CVD growth of graphene. Defects induced by the transfer process are discussed in section 1.3.

The most common intrinsic 0D defect is the Stone-Wales defect (see fig. 1.5 (a)), in which the in-plane rotation of 90° of a single carbon bond results in two pairs of pentagonal (in green) and heptagonal (in red) rings instead of the typical honeycombs, leading to the displacement of the atoms in immediate vicinity of the defect and to out-of-plane wavelike structural defects extending over nanometers [69].

The absence of one or more carbon atoms in the typical carbon rings forming the graphene layer are referred to as single or multiple vacancy defects. These defects are less common than the Stone-Wales defects due to their higher energies [66]. The simplest vacancy defect is when a single C atom is missing in the lattice. This leads to both a five-sided ring
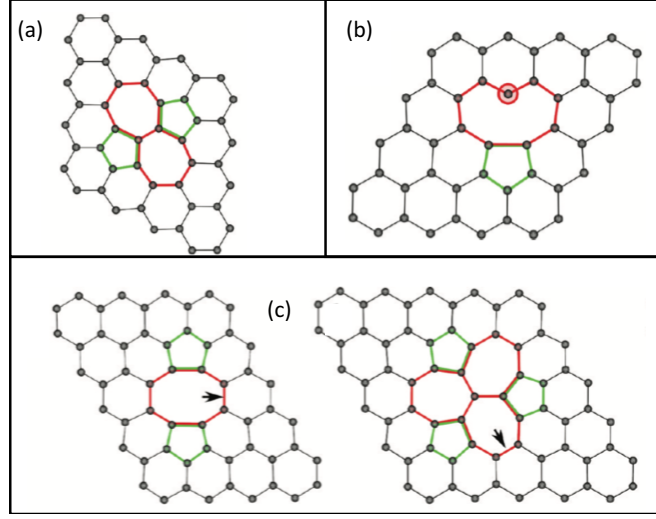
Figure 1.5 – Schematic representations of defects in the graphene lattice (a) Stone-Wales defect (b) Single vacancy with the dangling bond represented as a red circle (c) Double vacancies. Adapted from [66].

and a nine-sided ring as is shown in figure 1.5 (b). In this single-vacancy configuration, a dangling bond always remains (indicated by a red circle in figure 1.5 (b)). For double vacancies, as shown in figure 1.5 (c), unlike the single vacancy, there are no dangling bonds and the network remains more coherent with minor perturbations in the bond lengths around the defect. The double-vacancy is energetically more favorable and more commonly observed [66].

Two other types of defects may occur when growing graphene by CVD on polycrystalline Cu as is the case in most of our work. First, because the graphene begins its growth in different positions on the Cu substrate, domains of different crystallographic orientations are formed and grow until they join. Upon merging with surrounding patches of graphene, differently oriented patches yield line defects (1D), along which a chain of pentagons, hexagons and heptagons may appear. The density of these defects can be minimized by growing graphene on single-crystals such as Ir(111), although they may seldom appear as shown in figure 2.16.

Second, impurities such as nitrogen may generate substitutional defects (0D), where a C atom is replaced (most commonly) by a N atom, which forms chemical bonds with neighboring C atoms. This substitution is enabled by the chemical similarity between C and N atoms, which have similar atomic radii (less than 10 % difference) and have 6 and 7 electrons respectively. Other atoms that do not easily fit into the graphene layer, instead find it more energetically favorable to lie on top of the graphene surface. These atoms may be carbon atoms which were generated from the single or multiple vacancy defects or metal atoms or oxygen-containing functional groups [66].

As will be shown in section 2.1, Raman spectroscopy enables one to probe the defect density in graphene by the appearance of characteristic peaks generated by the presence of defects.

1.2   Monolayer graphene synthesis

Monolayer graphene can be obtained on a variety of substrates with a multitude of techniques, each having characteristic carbon sources, pressure and temperature parameters. In some cases, with a modified set of parameters, similar techniques can be used to yield multilayer graphene which we will discuss further in this chapter. All synthesization techniques can be classified in two categories, depending on whether the approach is top-down (where a single layer of graphene is isolated from bulk graphite) or bottom-up (where graphene is formed by assembly of carbon atoms). Most of these growth techniques are summarized in figure 1.6. Deposition of carbon atoms and segregation from the bulk are not depicted in the figure but are explained hereafter.
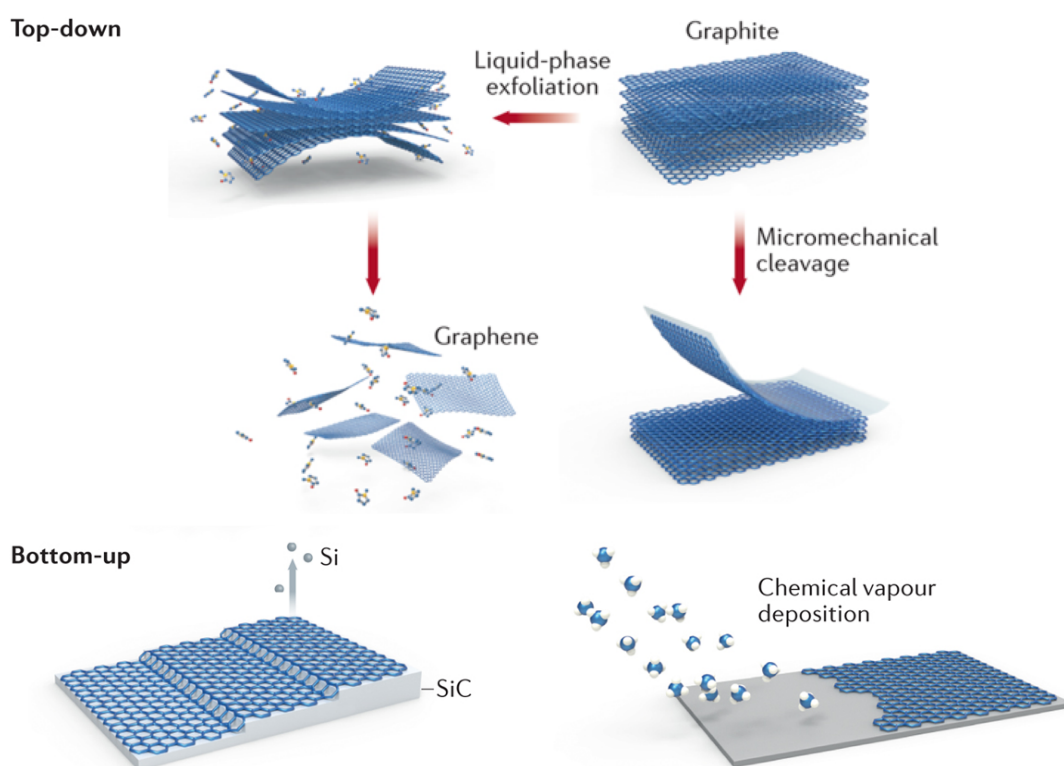
Figure 1.6 – Graphene synthesis approaches. The top-down approaches are based on the exfoliation in liquid phase or by mechanical cleavage of graphite sheets. Bottom up approaches include the evaporation of Si from SiC layers or the chemical vapor deposition of a carbon-containing precursor gas on the target surface. Figure adapted from [70].

Top-down approach

The original method developed to isolate a single layer of graphene, presented by Professor Sir Andre Geim and Professor Sir Kostya Novoselov, consisted in using a piece of tape

to repeatedly remove graphene layers from bulk graphite until a single layer was left on the tape [3]. Although this mechanical exfoliation process performed on highly oriented pyrolytic graphite (HOPG) yields high quality graphene and is very simple, it is time consuming and yields small samples, with very little control on domains, limiting its potential for commercial mass-production, although used in research. Similar in principle to mechanical exfoliation, liquid phase exfoliation (LPE), a three-step process, is a scalable technique which yields flakes of mono and multilayer graphene [5, 6, 71]. First, graphite is chemically oxidized, which reduces the binding energy between layers and enables separation of the graphene oxide layers in the second step by providing energy through sonication or electrochemical processes. Finally, the graphene oxide must be reduced in order to obtain graphene, which increases the tendency to regroup with other layers and also induces defects in the lattice.

Both of these top-down techniques mainly suffer from difficulty in controlling the number of graphene layers obtained, which is incompatible with our work aiming to transfer a single layer at a time and for this reason are not discussed further.

Bottom-up approach

Alternatively, graphene can be grown with a bottom-up approach, where single atoms of carbon combine to form a layer (or more) of graphene on a substrate. The source of carbon atoms can either be the growth substrate, a solid C source, or a carbon-containing (precursor) gas.

In the first case, graphene growth is generated by thermally induced segregation of carbon atoms to the surface in bulk carbon-soluble materials such as nickel [72], platinum [73, 74], ruthenium [75–77] or SiC [78] and enables growth of single and multilayers of graphene. In the cases of nickel, platinum and ruthenium, the samples must first be annealed and exposed to hydrocarbons, which dissociate and allow the C atoms to diffuse in the bulk. The carbon-containing sample can then be annealed and the cooling rate of the sample dictates the mobility of carbon atoms that migrate to the surface of the sample [79]. Rapid quenching freezes the mobility of C atoms and allows a single layer of graphene to be grown. In contrast, slow cooling enables multilayers of graphene to form. In the case of SiC, high quality graphene films have been demonstrated by annealing SiC samples at temperatures in excess of 1650 °C in an argon environment [80, 81].

Alternatively, carbon atoms can be deposited on the surface, either by CVD or by molecular beam epitaxy (MBE). For growth by CVD, a catalyzing substrate, such as Cu, Ni or Ir, usually kept at high temperature, is exposed to a carbon-containing gas (such as methane (CH_4) or ethylene (C_2H_4)) which decomposes on the substrate surface, leaving adsorbed C atoms that diffuse and aggregate to form the graphene layer [11, 13, 82]. Large area graphene has been demonstrated using CVD, with wafer-scale single crystal graphene on Germanium [10], 30 inch graphene on polycrystalline Cu [83] or ultra-high

oriented grains of graphene on a Cu(111) foil of dimensions up to 5 x 50 cm^2 [84]. For growth by MBE, carbon atoms are evaporated from a solid C source onto the growth substrate surface at high temperature, not requiring catalyzing activity [85–88].

Depending on the substrate, the process is self-limiting or not, and a single layer of graphene or multiple layers are formed. For our work, we describe the detailed procedure in the case of growth on a Cu substrate in section 2.6.1 and on an Ir(111) substrate in section 2.6.2.

For a complete description of growth processes, the reader is referred to graphene growth and applications reviews [8, 89–91].

1.3   Graphene transfer

Since graphene growth requires specific conditions, it cannot be obtained on any given surface. Instead, on surfaces where it cannot be grown, the only possible solution is to transfer a CVD-grown or an exfoliated layer of graphene onto that surface. The basic components for graphene transfer are a graphene source, such as CVD grown graphene on Cu, a transfer medium to support the graphene layer, a technique to isolate it from its growth substrate and a target sample. There are various combinations that are used, each with their advantages and disadvantages. In general, graphene transfer processes are known to introduce defects and contamination to the graphene layer as shown in figure 1.7.
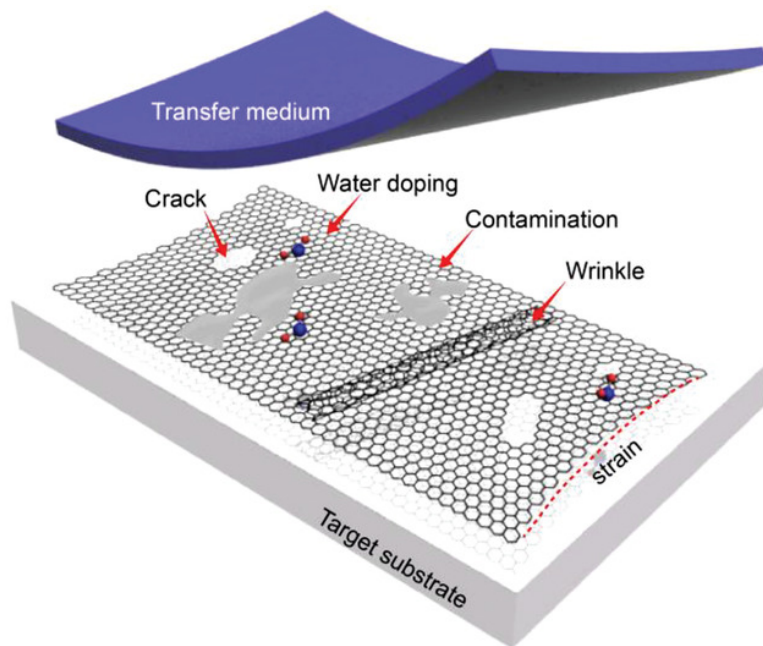
Figure 1.7 – Schematic of the defects and contamination due to the graphene transfer process [92]. The transfer medium (carrier layer) can be PMMA, PVA, PET, PDMS, etc...

Generally, the supporting layer is required in order to conserve the quality and continuity of the graphene layer during the transfer procedure. Indeed, it has been shown that the yield of suspended graphene over a hole drastically decreases with increasing hole dimension, such that for holes larger than 8 μm in diameter, more than 40 % of the suspended graphene breaks [93], making a support-layer-free transfer prone to damaging the graphene. However, the support layer (transfer medium) is known to leave behind residue. PMMA is the most commonly used polymer for the support layer. Once the transfer is completed, the supporting PMMA layer can be removed by immersing it in hot acetone. Studies have, however, shown that this transfer procedure introduces PMMA residue which is impossible to completely remove [94]. However, optimizing the PMMA

preparation results in the minimization of residue [95] and using low pressure air plasma for PMMA removal has also demonstrated a 71 % decrease in residue content [96]. The residual polymer amount impacts the electrical and thermal properties of graphene [97]. In the cases where graphene is rinsed in water post-transfer, there may be doping of the surface with water. This can however be removed by annealing to temperatures in excess of 100 ℃.

In addition to residue, various strains and imperfections in the supporting layer may induce defects in the form of cracks in the sheet or wrinkles, where the graphene forms bunches or rolls up. Additionally, depending on the anchor points during transfer, the graphene sheet also experiences strain.

The minimization of residue amount and defects is key for a high quality transfer procedure. Minimizing contamination from both the etching solution and the support layer can be achieved by adopting a low-residual support layer and by performing multiple etchings to remove contamination of previous etchings. Further, cracks, wrinkles and strain can be minimized by choosing a support layer that is sufficiently flexible to adapt to both the graphene layer and the target surface at atomic scale and which during removal (for example by immersion in hot acetone for PMMA) does not cause excessive strain on the graphene layer.

Graphene transfer methods can be classified in two categories depending on whether the graphene isolation technique is based on chemical etching of the metal growth substrate or if instead the technique is etching-free. We present other approaches that do not use PMMA as a supporting layer. This section does not present all known transfer methods. For a more in-depth review of all transfer methods, the reader is referred to graphene transfer method reviews [49, 98, 99].

1.3.1   Chemical etching transfer

In most chemical etching transfer methods, the growth substrate is chemically etched away from under the graphene. For a Cu substrate, $FeCl_3$ is generally used as the etchant, although other Cu-etching solutions can be used. The etching procedure is a process described by three reactions :

$$FeCl_3 + Cu \rightarrow FeCl_2 + CuCl \tag{1.10}$$

$$FeCl_3 + CuCl \rightarrow FeCl_2 + CuCl_2 \tag{1.11}$$

$$CuCl_2 + Cu \rightarrow 2CuCl \tag{1.12}$$
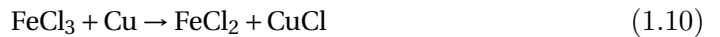
The Cu reacts with the $FeCl_3$ by forming a solution of $FeCl_2$ and $CuCl$, which further reacts with the $FeCl_3$ forming copper chloride, which in turn also reacts with the Cu, further etching it. This procedure, although simple and preserving the quality of graphene,

has been shown to leave behind substrate residue as well as metallic ions from the etching solution (typically Fe atoms) [100,101], which can mostly be removed by a second chemical etching with acid etching solutions such as HCl or HNO_3 [102]. Low etching solution concentrations are preferred as slow dynamics cause less damage to the graphene layer. In the case where the CVD graphene lies on both sides of the Cu growth substrate, before the chemical etching, the graphene layer on one side is removed by Oxygen Plasma if a single layer of graphene is targeted [103].

Instead of PMMA, thermal release tape (TRT) can be used as a supporting layer [104]. Although simple, the transfer procedure using TRT has been shown to leave residue and is not as well adapted to large area transfer due to inconsistent adhesion of the tape [105].

1.3.2   Etching-free transfer

Etching-free transfer methods involve the delamination of graphene from its growth substrate. The first obvious advantage of such methods is that the Cu or Fe residual atoms that are a by-product of the chemical etching processes are avoided. However, in order to support the graphene, a supporting layer is still required and may introduce residue. Further, the growth substrate can theoretically be reused after delamination for a new growth.

One of these etching-free methods is electrochemical bubbing, which is based on the principle of electrolysis. A sample of CVD grown graphene on a metal such as copper [106,107], platinum [52], or iridium [108] is covered with PMMA and used as the cathode of an electrolysis cell. A platinum wire is used as the anode. Both are immersed in an NaOH solution and a voltage is applied to the system. This leads to the formation of hydrogen bubbles at the interface between the metal substrate and the graphene layer, peeling off the graphene/PMMA from its growth substrate in a matter of minutes [109]. The PMMA layer is removed post-transfer by immersion in acetone.

Alternatively, dry transfer procedures do not require the sample to be placed in a liquid solution for delamination. Instead, graphene is mechanically delaminated from its growth substrate by means of a polymer stamp. The (generally CVD-grown) graphene layer is first covered with PVA and subsequently covered with PMMA for extra support. In this way, PMMA residue can be avoided as it is not in contact with the graphene directly, but with the PVA buffer layer that can be removed by immersion in hot water [110]. Similarly to this PVA/PMMA approach, it has been shown that PDMS can be used as a supporting layer for delamination [111], or that one can also use only PVA [54]. Once covered with PVA the gr/PVA stack is delaminated from the Cu growth substrate using a PDMS stamp. This transfer procedure is described in detail in section 3.4.

1.4 Multilayer graphene types and synthesis

The most common example of multilayer graphene is graphite. Indeed, graphite consists of multiple layers of graphene stacked on top of each other with an interplanar spacing of 3.35 Å [57]. In graphite, the most common stacking type between layers is of type AB (see fig. 1.8 (b)), also referred to as Bernal stacking, where atom B of the top layer lies directly on top of atom A of the lower layer (atoms A and B in fig. 1.1). The center of the hexagon between two layers is displaced such that a hexagon centre of one layer is aligned with a carbon atom from the layer below it. This type of stacking is an energetically favorable configuration. Less commonly, because energetically less favorable, graphite may exist in an AA stacking configuration where the two layers are aligned on top of each other as is shown in figure 1.8 (a).

Configurations that are not AA or AB stacked are referred to as tBLG. In this case, the relative orientation between two graphene layers is defined by an angle (α in fig. 1.8 (c)). This type of stacking is observed typically when two graphene layers are stacked mechanically with a controlled (or not) relative angle, but have also been shown to appear for multilayer graphene growth on Ir(111) [112–114] or on Pt(111) [115].
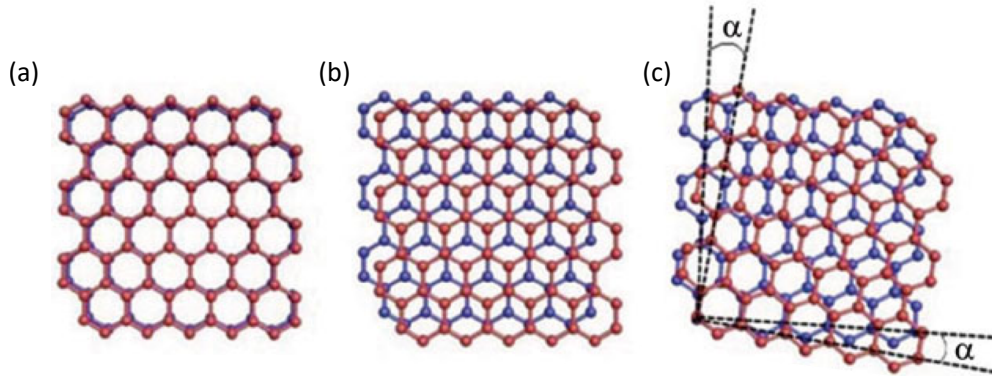
Figure 1.8 – Stacking types of bilayer graphene. The lower layer of graphene is blue, the upper is red. (a) AA stacking. (b) AB stacking. (c) Twisted bilayer graphene, characterized by twist angle α. Adapted from [116].

The simplest (top-down) technique for multilayer graphene production is exfoliation from bulk HOPG. Using this technique, there is however very little control on the number of layers. Alternate bottom-up techniques, which allow better control on the number of layers, include CVD of a carbon-containing gas or segregation of carbon atoms from bulk of a carbon-soluble substrate such as ruthenium [42, 117, 118] which can also be combined to yield multi-layer graphene as is done in the case of platinum, where varying the cooling rate leads to a control on the amount of graphene formed [79].

The growth process of the multilayer graphene on a given substrate depends on the carbon solubility of the substrate, its ability to form stable carbides, and its reactivity to carbon [119]. A high carbon solubility sample will have the ability to form multiple layers of graphene by segregation of the carbon atoms from the bulk towards the surface in specific growth conditions. The multilayer systems relevant to our work are discussed in what follows.

BLG grown on Cu

Multilayer graphene can be obtained using Cu as a growth substrate. The process involved uses a high hydrogen pressure to passivate the graphene on its edges with H_2, such that the edges are detached from the catalyst surface, allowing the diffusion of carbon into the area beneath the monolayer to form the second layer underneath [119, 120].

Multilayer graphene grown on SiC

In recent years graphene on SiC has been the center of attention for nanomaterials because of the large-area, high-quality graphene and because of its compatibility with current semiconductor manufacturing technologies [81]. Similarly to the growth method for single layer graphene on SiC, multilayer graphene is formed on SiC by thermal decomposition. The number of layers depends on the annealing temperature, time, and on surface polarity, but is difficult to control. On the C-terminated surface, the graphene layers often are rotated with respect to each other, whereas on the Si-terminated surface, the multilayered graphene has Bernal (AB) stacking [121].

BLG by mechanical stacking or folding

As mentioned in the introduction, stacking two layers of graphene generally involves covering graphene with a supporting layer and transferring one layer on top of another. This can be done in the simplest form with graphene grown by CVD on polycrystalline Cu and yields multiple domains of random orientations [41]. Alternatively, higher control over the twist angle has been demonstrated using the tear and stack method [122], which is based on the separation of a graphene domain in two parts, selective picking of one, and transfer with a controlled rotation angle onto the other part, yielding tBLG [35, 42, 123]. Alternatively, instead of tearing and stacking the graphene, tBLG samples have been obtained by folding the graphene layer [43, 124].

We demonstrate BLG made by mechanical stacking of two single graphene layers in section 3.4.2. In general, graphene bilayers obtained by mechanical stacking, however, inevitably suffer from defects and contamination, both of which are induced by the transfer procedure (see fig. 1.7) and thus minimization of contamination is essential. We demonstrate a fully-UHV compatible procedure for stacking in chapter 4, with reduced residue.

2 Graphene synthesis and characterization methods

This chapter focuses on the experimental methods employed to characterize the graphene transfer process in our work. In section 2.1, Raman spectroscopy is described with emphasis on graphene's Raman signature. In section 2.2, X-ray Absorption Spectroscopy and how we used it for graphene transfer assessment is presented. In sections 2.3 and 2.4, Auger Electron Spectroscopy and Scanning Tunneling Microscopy are introduced, both of which can be used in the Ultrahigh vacuum (UHV) experimental chamber in our EPFL laboratory, which we describe in section 2.5. In section 2.5.3, we describe the mechanism used for graphene transfer in our chamber. Finally, the MLG growth techniques (graphene on Cu and on Ir(111)) used in our work are described in section 2.6.

2.1 Raman spectroscopy

Raman spectroscopy is a technique used to determine the vibrational signature of molecules and is typically performed in air. When light interacts with the molecules of a material that can be present in the solid, liquid, or gas phase, the oscillating electromagnetic field of the incident photons induce a polarization of the electronic cloud, which places the molecule in a higher energy state, as shown in figure 2.1.

A photon arrives on the sample with wavelength λ_i and is scattered at a wavelength λ_s. A majority of the photons undergo elastic scattering, where the energy (or wavelength) of the scattered photons is the same as the incident photons. This type of scattering is also referred to as Rayleigh scattering. These photons give no information on the molecules and are filtered out. When the energy of the exciting photon is close to the transition energy between two real states, the molecules can be excited to an electronic state that is an eigenstate of the system and relax back into a lower energy level by emission of a photon ($\lambda_{\text{emission}}$) of wavelength characterized by the energy difference between the two electronic states, referred to as fluorescence. This process depends on the
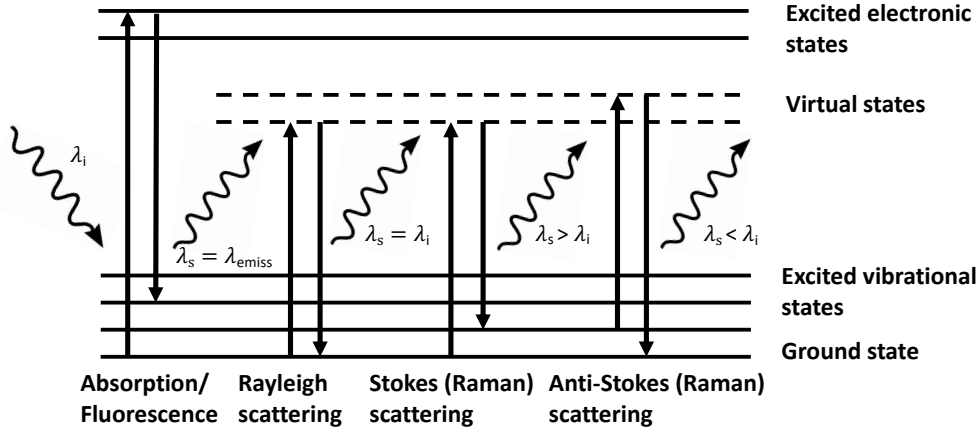
Figure 2.1 – Scattering processes involved when a photon interacts with a sample. The electromagnetic field of the incident photon (λ_i) excites the molecule to a real or virtual higher energy level, from which it then decays with photon emission to a level with the same or different energy from its initial state. The majority of the photons are scattered elastically (Rayleigh). A small fraction of them are absorbed and emit photons (λ_{emiss}) to decay to a lower energy state (fluorescence) and another small fraction are scattered with a different energy (Raman processes).

energy levels of the atoms of the sample as well as laser energy. Fluorescence generates a background which in some cases may completely cover the Raman signal of graphene on top (gr/Ir(111) for example [125]).

A small fraction of photons will scatter at a different energy than the incident photon (inelastic scattering). The molecules are excited to a virtual energy state (a state that is not a free eigenstate of the system and is very short-lived), before decaying to another level (same as initial, higher or lower energy state). The change in the photon energy is converted into energy in the vibrational or rotational state. Because the energy states are virtual, the non-resonant Raman signature of a molecule is independent of the laser excitation. Raman-active modes must conserve both energy and momentum to exist and thus impose conditions on possible processes as will be shown in section 2.1.1.

If the emitted photon is of lower energy ($\lambda_s > \lambda_i$) than the incident radiation, the scattering is referred to as Stokes scattering. On the contrary, if the emitted photon's energy is higher than the excitation energy ($\lambda_s < \lambda_i$), the process is referred to as anti-Stokes scattering.

For these types of scattering, Raman shift is defined as the change in frequency undergone by monochromatic light scattered by a sample :

$$\Delta\nu = \left(\frac{1}{\lambda_i} - \frac{1}{\lambda_s}\right) \times 10^7 \qquad [\text{cm}^{-1}] \tag{2.1}$$

Where λ_i and λ_s are expressed in nanometers and the multiplication factor accounts for the conversion to cm^{-1}.
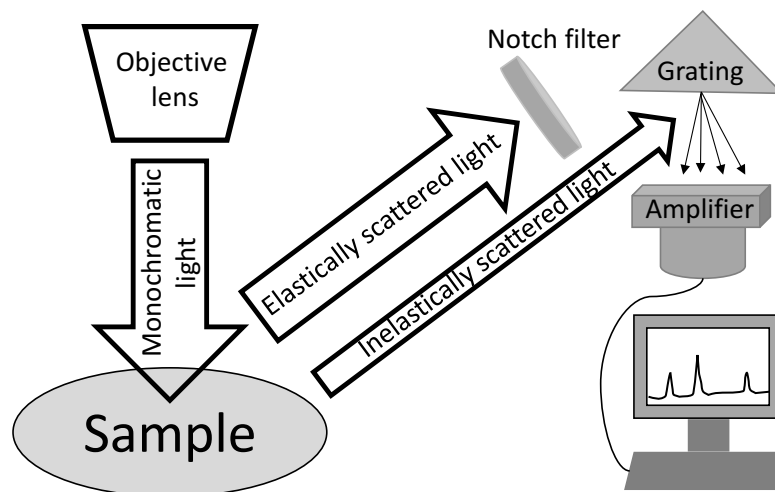
Figure 2.2 – Schematic of Raman spectroscopy showing the main components of a Raman spectrometer. A monochromatic laser light interacts with a sample. The inelastically scattered light is directed onto a grating and through an amplifier communicating with a data acquisition software with user interface.

Experimentally, the sample is exposed to a laser beam through the objective lens (see figure 2.2). The chosen laser wavelength depends on the analyzed sample. Laser wavelengths range from ultraviolet to near infra-red. The Renishaw inVia confocal Raman microscope [126] we used is equipped with three lasers with wavelengths 488 nm, 532 nm, or 785 nm. Higher wavelength lasers such as the 785 nm laser are less affected by fluorescence (which increases with the energy of incoming photons), but the Raman scattering intensity being proportional to λ^{-4}, lower wavelength lasers such as the 488 nm wavelength laser are far more sensitive (throughout most of our work, the 488 nm wavelength laser was used). The depth sensitivity of Raman spectroscopy also strongly depends on the selected laser wavelength. On a silicon sample, the penetration depth of a 785 nm laser is about 12 μm, at 532 nm it is 0.7 μm while in the UV range (10-400 nm) it can drop to 5–10 nm [127].

To avoid damaging samples, the intensity of the beam is fixed by the user in measurement settings. The elastically scattered photons are then filtered out with a notch filter. The inelastically scattered photons are reflected onto a grating (the density of the grating in lines/mm defines the spectral resolution). The photons diffracted from the grating reach a CCD camera and the signal is amplified before being plotted as Raman intensity (in a.u.) vs. Raman shift (in cm^{-1}). The acquired spectrum yields the vibrational signature of a molecule, giving insight into the bonds between atoms and in the case of graphene, into eventual defects.

In our measurements using a 488 nm wavelength laser, two gratings of respectively

2400 l/mm and 600 l/mm were available. The 600 l/mm grating covers a far broader spectrum of wavelengths in a single acquisition, but sacrifices resolution to do so. In order to maximize resolution of the peaks we used a 2400 l/mm grating. The range of the acquired spectrum is, however, not sufficient to cover the total range between the D and 2D bands (1350 cm^{-1} to 2700 cm^{-1}). For each measurement, two separate spectra centered around the G and 2D bands respectively were acquired and assembled.

In practice, the two spectra are acquired successively on the same spot without modifying the sample position and laser focal. The first spectrum ranges from 840 cm^{-1} to 2250 cm^{-1} and the second one ranges from 2065 cm^{-1} to 3275 cm^{-1}, with an overlap region between 2065 cm^{-1} and 2250 cm^{-1}. Each spectrum is separately normalized to the area (approximated by the trapezoidal rule) under the overlap region (between 2065 cm^{-1} and 2250 cm^{-1}), allowing for comparison between G and 2D band intensities or areas, after background subtraction (due to fluorescence of the underlying substrate).

2.1.1   Raman spectrum of graphene

As an example for graphene analysis using Raman spectroscopy, the Raman spectrum of a commercially available graphene suspended on a TEM grid (Ted Pella Inc. [128]) is shown in figure 2.3. There are 3 main bands originating from both zone-center and zone-edge phonons (see figure 1.4), which are used for assessment of graphene quality and number of layers [129–131]. The processes generating these bands are sketched in an energy-momentum graph in figure 2.4.
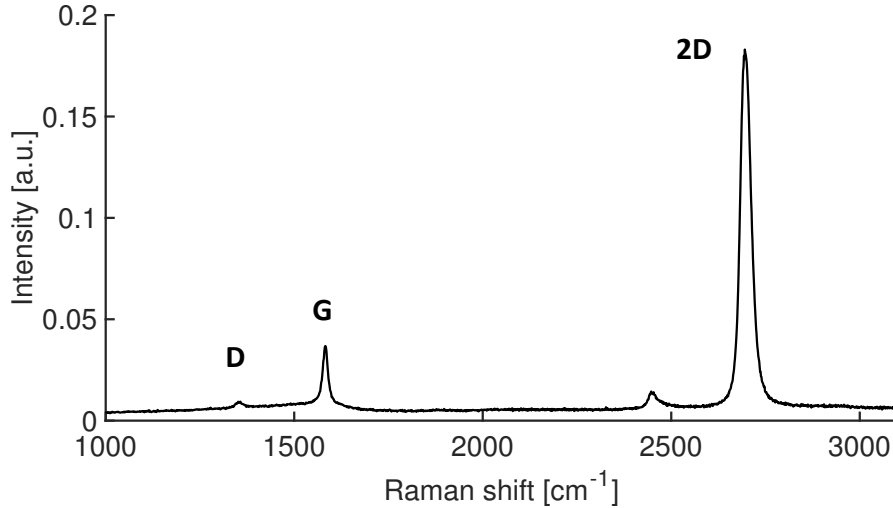
Figure 2.3 – Raman spectrum of a commercial single layer of graphene on TEM grid (Ted Pella Inc. [128]). The 3 main bands (D, G and 2D) are labelled. 488 nm laser wavelength, 2400 l/mm grating, 25 mW power, exposition time of 50 s, averaged over 10 sample regions.

The G band, characterized by a Raman shift of 1580 cm^{-1}, represents an in-plane
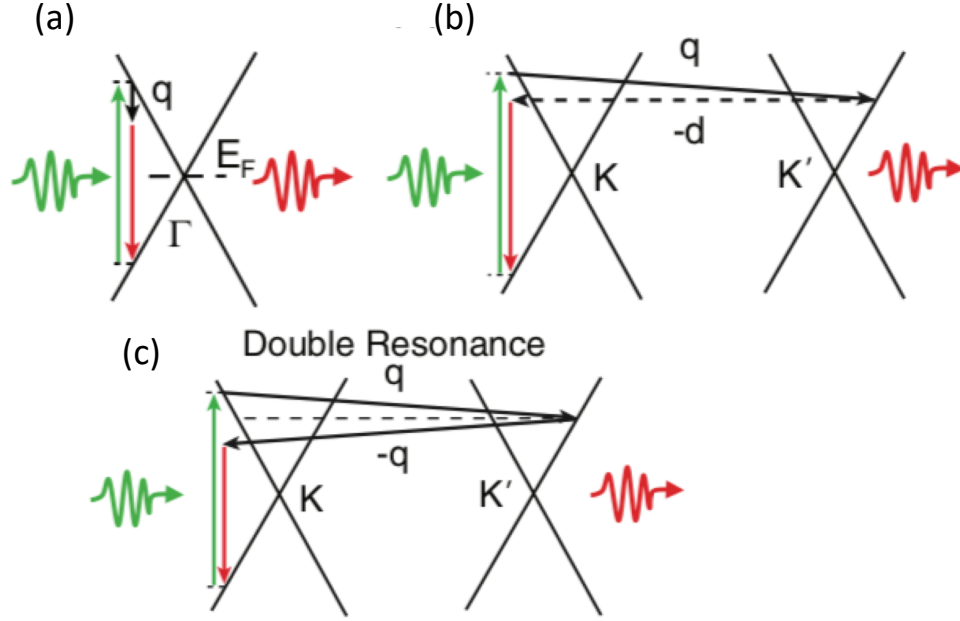
Figure 2.4 – Energy-momentum schematic graph showing Dirac cones with Raman scattering processes of photons on the sample for the (a) G band, (b) D band and (c) 2D band. The Fermi energy is noted E_F, the phonons $\mathbf{q}$ and the defect $\mathbf{d}$. In green, the incoming photon and in red the outgoing photon. Adapted from [131].

vibrational mode involving the sp^2 carbon atoms. It is a one phonon process where the incident photon resonantly excites a virtual electron-hole pair in graphene, which is then scattered by an iTO (in-plane Transverse Optical phonon) or iLO (in-plane Longitudinal Optical phonon) zone center phonon (zero momentum). The electron-hole pair then recombines and emits a photon redshifted by the amount of energy given by the phonon. Due to the zero momentum, this is an intra-valley process. The intensity of this band is proportional to the area probed by the laser and has been shown to increase with increasing numbers of layers (more atoms contribute to the vibration mode), to about 10 layers where it is maximal and then decreases again and tends towards G band values of graphite [132]. Our work involves only a maximum of three layers of graphene; it is considered that the G band intensity increases with increasing layer number.

The 2D band, characterized by a Raman shift of 2700 cm^{-1}, represents an in-plane breathing-like mode of carbon rings. It is a two-phonon inter-valley process where an electron-hole pair is created by the incident photon near K point and the electron is inelastically scattered by an iTO phonon ($\mathbf{q}$) to the K' point. In order to conserve energy and momentum, it has to be scattered back to the K point by another phonon ($\mathbf{-q}$) before recombining with the hole.

The shape of the 2D band has been shown to be an indicator of the number of layers of graphene [129]. Indeed, in the case of Bernal stacked (see section 1.4 bilayer graphene

(BLG) a splitting of the 2D peak into four sub-peaks is expected due to the interaction between graphene planes causing the π and π^* bands to divide into four. This is not necessarily observed in misaligned bilayer graphene [133]. In our work, the assessment of layer number, generally between a single layer and bilayer of graphene, relies instead on the evolution of the peak intensities and FWHM (shown to vary with layer number [133]) as well as the ratios between peak intensities. The $I(G)/I(2D)$ peak intensity ratio increases as the number of layers increases [134]; however, comparison between results obtained on various substrates also shows that this ratio is dependent on the underlying substrate [135, 136]. Therefore, the $I(G)/I(2D)$ ratio can only be used for comparison of graphene layers on identical substrates as will be discussed in section 4.

The D band, characterized by a Raman shift of 1350 cm^{-1}, is also called the defect peak. Similarly to the 2D-band, it involves an iTO phonon ($\mathbf{q}$) around the K-point. However, the electron inelastically scattered by the iTO phonon to the K' point is then elastically scattered back to K point by a defect ($\mathbf{-d}$). Only one phonon is involved thus the energy shift is half of the 2D band's. This process is also an inter-valley process and its intensity is proportional to the defect density in the area probed by the laser. The larger the band relative to the G band (an sp^2 vibration), the higher the defect density [130, 131, 137, 138]. It has been shown that different types of defects have specific influences on the D band shape and position [131] and in the case where the defect density is low and the distance between defects L_D is larger than 10 nm, the ratio between D and G band intensities, $I(D)/I(G)$ is proportional to the defect concentration defined as $1/L_D^2$. On the other hand, when the defect density is high, the $I(D)/I(G)$ ratio increases proportionally to L_D^2 [129].

Similarly to the inter-valley processes that generate the D and 2D bands (see fig. 2.4), there exist intra-valley mechanisms that generate the D' band (defect activated, shift of 1620 cm^{-1}) and the 2D' band (shift of 3240 cm^{-1}), which are typically much weaker in intensity than the D and 2D bands. The ratio between D and D' bands was shown to be maximal for sp^3-defects, to decrease for vacancy-like defects and to reach a minimum for boundaries in graphite [139]. In general, these bands were not observed in our work, implying that the defects in our graphene samples were in majority sp^3 type defects. Although the most commonly encountered defects were described in section 1.1.4 we do not focus on the effect they produce on the D and D' bands as the defect density is more relevant for our work.

Finally, in figure 2.3, the peak located at 2450 cm^{-1} is believed to be an overtone, a combination between a band around 1100 cm^{-1} and the D band (1350 cm^{-1}) [140].

In practice, to study the uniformity of graphene, spectra are acquired over multiple regions of the sample. The averages are then given with a confidence interval evaluated as the standard deviation of the dispersion of the values measured in different spots. The measurement error on the fits of the peak intensities is 3 %, which in most cases is much

smaller than the confidence interval and is therefore neglected.

In summary, by analyzing multiple points on the surface using Raman spectroscopy, one can assess the quality, continuity and uniformity of the graphene layer as well as determine (to a certain extent) the number of layers. In practice however, in our work, the limitations of Raman spectroscopy lie in the impossibility to obtain spectra of graphene on highly fluorescent samples such as platinum or iridium.

2.2 X-ray Absorption Spectroscopy (XAS)

X-ray Absorption Spectroscopy is an extremely sensitive surface analysis technique based on the absorption of photons by core electrons. While the spectrum in vicinity of an absorption edge (X-ray absorption near edge structure (XANES) or Near-edge X-ray Absorption Fine Structure (NEXAFS)) is used for determination of the local electronic state of atoms, the portion well above an absorption edge, referred to as extended X-ray Absorption Fine Structure (EXAFS) gives access to interatomic distances and coordination level of atoms [141]. Characterization of orbital polarization can be carried out by X-ray linear and circular dichroism (XLD and XCD), which are based on the difference in absorption with respect to incident photon polarization. In a magnetic field, X-ray magnetic circular dichroism (XMCD) or X-ray Magnetic Linear Dichroism (XMLD) give information on the magnetic properties of atoms [142].

When a photon strikes an atom, a core electron can either be ejected from the atom into a vacuum continuum (used in X-ray Photon Spectroscopy (XPS)) or promoted to an unoccupied electronic state. XAS is based on the change in absorption coefficient of the studied sample while scanning the energy of incident photons. Indeed when the energy of incoming photons matches that of a transition from core electron to an empty valence level or to eject the electron into a continuum, the absorption coefficient increases sharply. Each edge occurs at its own characteristic absorption energy, given by the electron binding energies in the different shells of the atom (K,L,M...) [141]. The high sensitivity of XANES is also used to detect surface contamination by tuning the photon energy to match the absorption energies of suspected contamination molecules.

In practice, a high intensity beam of photons (x-rays) is guided to the surface of a sample mounted in a UHV chamber. The x-ray (photon) energy is tuned to the values of the absorption edges of the atoms that are being studied. For instance, probing graphene on a surface requires the x-ray energy to be swept around the K-edge absorption energy of C (284 eV). X-ray absorption can be acquired in different ways; in this thesis we use the total-electron-yield (TEY) mode given its strong surface sensitivity.

Our experiments were performed at the end-station of the EPFL/PSI X-Treme beamline of the Swiss Light Source at the Paul Scherrer Institute in Villigen, Switzerland [143]. The end-station is equipped with an *in-situ* preparation chamber where samples can be prepared and cleaned. For measurement, the sample is mounted on a rotating sample-holder where it is exposed to the incoming x-rays (a magnetic field can be applied for XMCD or XMLD). The photons can be polarized either circularly (+ or -) or linearly (0° or 90°). A schematic representation of the relative orientations of the sample and x-rays is shown in figure 2.5; the 0° ($\vec{E}$ field) polarization vector is in the plane defined by the surface normal and the x-ray beam and the 90° polarization is parallel to the sample surface. The angle θ between surface normal and incident photon beam can be adjusted with a precision of 2-3°.
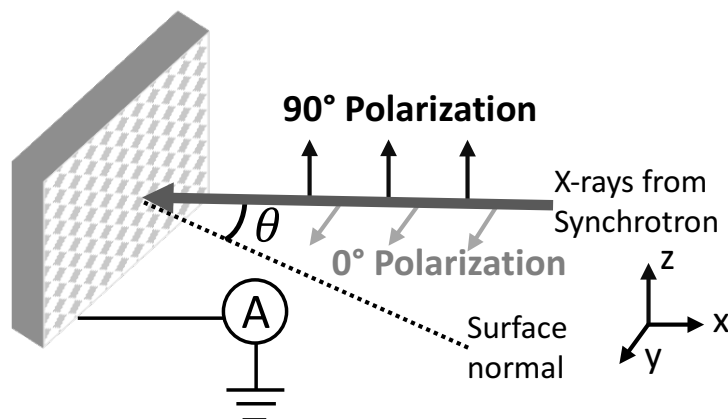
Figure 2.5 – Schematic of sample and beam geometry for XAS at the X-treme beamline [143]. The incidence angle θ is 60° for grazing incidence and 0° for normal incidence.

As shown in section 1.1, the electronic orbitals of graphene are in-plane sp^2 (σ) bonds between carbon atoms and the out-of-plane π electron orbitals. There are therefore 2 main transitions that characterize the graphene XANES. The π electron orbital absorption peak, corresponding to a C 1s→$\pi*$ transition, at 285 eV, and the σ electron orbital peak, corresponding to a C 1s→$\sigma*$ transition, at 292 eV. At fully grazing incidence, one can in principle select one of these two transitions by choosing the linear polarization direction. At 0° polarization, only the out-of plane π orbitals of the carbon atoms in graphene are detected, and in 90° polarization, only in-plane σ bonds contribute to the XAS. However, the cross section at fully grazing incidence is very small, and for this and other experimental reasons, the maximum angle of incidence is 60° off surface normal. Thus at 0° polarization, both the σ and π orbitals of graphene are detected.

Figure 2.6 shows the XANES spectrum of graphene on a polycrystalline Cu sheet at the carbon K-edge transition measured in grazing (60°) incidence at the X-Treme beamline. The Cu background was acquired on a clean Cu sample and subtracted. The two main π and σ electron orbital absorption peaks are visible in the spectrum as clearly separate peaks. These XANES spectra can be used to determine if the sample is highly crystalline or amorphous (as will be shown in sections 3.4.2 and 4.4) and determine if graphene is flat or if it is wrinkled. Further, the intensities of the peaks enable us to distinguish a monolayer from a bilayer of graphene on a substrate as will be shown in section 3.4.2.
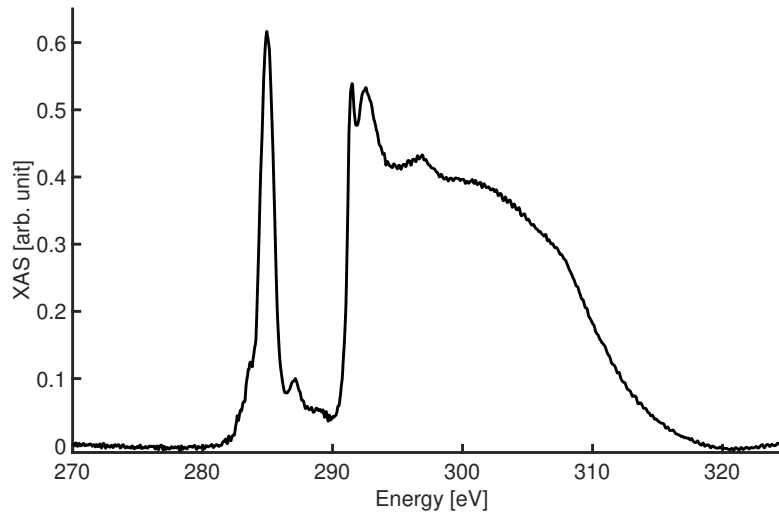
Figure 2.6 – Grazing incidence XANES at carbon K-Edge for a sample of monolayer graphene on Cu. The 0° and 90° polarizations have been summed. Graphene π orbital absorption peak at 285 eV and σ orbital peak at 292 eV. The spectra were acquired at 60° incidence at room temperature the X-treme beamline. Cu background was acquired on clean Cu single crystal and subtracted.

2.3 Auger Electron Spectroscopy

Auger electron spectroscopy can be used to reveal the chemical composition of surfaces. The interaction of a surface atom with a high energy electron beam or with x-rays may cause an electron of the atom to be ejected into the vacuum. When the ejected electron is a core electron, an electron on a higher level may decay into the vacancy (core hole) whereby it releases energy. This generally occurs by photon emission. However in some cases the energy can be transferred to another electron from the same atom, kicking it out into vacuum. This effect is called the Auger effect and the ejected electron is the Auger electron [144, 145]. Auger electron spectroscopy (AES) relies on the measurement of the kinetic energy of Auger electrons. Due to the limited escape depth of electrons from the solid for typical electron energies (see fig. 2.7 (a)), AES is a surface sensitive technique. The Auger intensity originating from atoms forming layers up to a depth z in the sample depends exponentially on the depth z [146] :

$$I(z) = I_\infty \left(1 - exp\left(-\frac{z}{\lambda}\right)\right) \tag{2.2}$$

where the constant I_∞ is the Auger intensity measured for a thick sample and λ is the mean free path of Auger electrons (which depends on electron energy). The total depth from which 95 % of the signal is emitted can be obtained by imposing that the signal $I(z_{95}) = 0.95 \cdot I_\infty$ and yields $z_{95} \simeq 3\lambda$.

The kinetic energy of the Auger electrons corresponds to the difference in energy between initial electronic transition into the vacancy and the energy required for ejection of the Auger electron into vacuum. Suppose E_A, E_B, and E_C are the binding energies (measured with respect to vacuum) of electrons in A, B, and C levels, respectively, of the neutral atom (see fig. 2.7 (b)). The energy released $(E_A - E_B)$ when the second electron decays from level B to level A is transferred to the third electron. Taking into account the work function (ϕ_S) of the spectrometer, the kinetic energy of the Auger electron E_{Aug} is then given by [147] :

$$E_{Aug} = E_A - E_B - E_C - \phi_S \tag{2.3}$$

The work function ϕ_S depends on the characteristics of the analyzer and on the geometry of the setup.

Auger transitions are denoted with the x-ray notation, using the shell notations (K,L,M,N,O,P), where K is the principal quantum number n = 1, L is n = 2 and so on. For example, in a $KL_1L_{2,3}$ transition, K is the core level hole (A in fig. 2.7 (b)), L_1 is the initial state of the relaxing electron (B in fig. 2.7 (b)) and $L_{2,3}$ the initial state of the ejected electron (C in fig. 2.7 (b)).
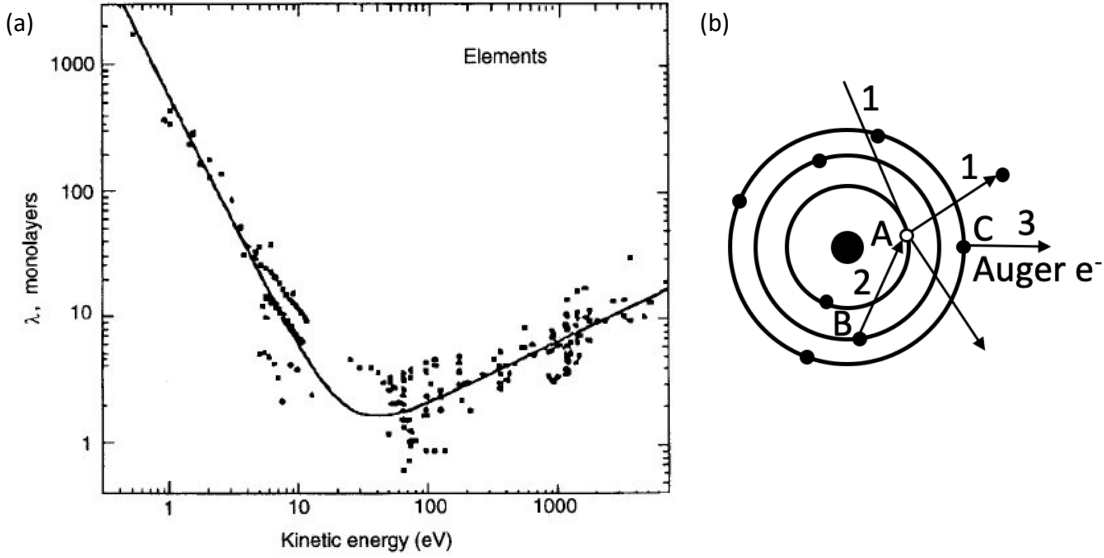
Figure 2.7 – (a) Mean free path of electrons in solid as a function of electron energy [148]. (b) Schematic of the auger electron generation process with electrons A,B and C in 3 steps : First the incoming electron kicks out a core electron A (1). Then, electron B decays into a lower energy level and transfers energy to electron C (2). Finally, Auger electron C is ejected into continuum (3).

The relationship between mean free path and the electron energy as shown in figure 2.7 (a) depends on the type of sample studied (element, organic or inorganic compound) [148]. For elements, the most accurate relation for λ (in monolayers) is $\lambda = 538E^{-2} + 0.41\sqrt{d \cdot E}$ whereas for inorganic compounds the relation is $\lambda = 2170E^{-2} + 0.72\sqrt{d \cdot E}$, where d is the monolayer thickness in nm and E the electron energy above the Fermi level in eV. For most elements, where the main peak's energy is higher than tens of eV, these two relationships are governed by the second term.

Using these equations, the mean free path of electrons can be calculated in the cases of electrons from the Iridium bulk, at an energy of 54 eV ($\lambda_{\text{Ir}}(54)$), electrons from the Iridium bulk travelling through a layer of graphene ($\lambda_{\text{C}}(54)$), and electrons from the graphene layer, at 272 eV energy ($\lambda_{\text{C}}(272)$) [148]. For graphene, the layer thickness is $d = 0.335$ nm and for Ir(111), the layer thickness is $a_{\text{Ir}} = 0.22$ nm.

$$\begin{cases} \lambda_{\text{Ir}}(54) = a_{\text{Ir}} \cdot \left(\frac{538}{54^2} + 0.41 \cdot \sqrt{(a_{\text{Ir}} \cdot 54)}\right) = 0.35\text{nm} \\[2mm] \lambda_{\text{C}}(54) = d \cdot \left(\frac{538}{54^2} + 0.41 \cdot \sqrt{(d \cdot 54)}\right) = 0.65\text{nm} \\[2mm] \lambda_{\text{C}}(272) = d \cdot \left(\frac{538}{272^2} + 0.41 \cdot \sqrt{(d \cdot 272)}\right) = 1.31\text{nm} \end{cases} \qquad (2.4)$$

As was shown previously, the analyzed depth is approximately 3λ and hence less than six monolayers of graphene on top of Ir(111) should completely mask the signal from

bulk iridium Auger electrons at 54 eV. Indeed, the analyzed depth at 54 eV is 1.95 nm and 6 layers of graphene should be 2.01 nm thick.

Our Omicron AES system consists of an electron source (NGE 52), a cylindrical mirror analyser (CMA 100), a lock-in amplifier and matching unit, all controlled by an Auger control unit (ACU) connected to a computer equipped with DATAuger data acquisition software. By scanning a specified range of energies of Auger electrons arriving on the detector, the resulting spectra can be used to determine the nature of the surface atoms, their concentration and environment. However, because of the large background during acquisition of the distribution function N(E), one records its derivative $\frac{dN(E)}{dE}$. For determination of Auger peak intensities, the sensitivity S_X (relatively to Ag) of an element X is calculated as [149] :

$$S_X = \frac{I_X}{I_{Ag}} \qquad (2.5)$$

Where I_X and I_{Ag} are the reference peak intensities for bulk material given in the handbook of Auger electron spectroscopy [149]. The $\frac{dN(E)}{dE}$ spectrum is also directly related to the power settings (filament current and voltage) of the electron beam, as well as analyzer parameters [149].

Calibration of the spectrometer is performed by acquiring the elastic peak (due to elastically scattered electrons) by scanning the analyzer energy around the incoming electron beam energy. Both sample-detector distance and x-y deflector values are changed in order to obtain the optimal elastic peak shape as proposed by Omicron's reference sheets.

In our work, AES is first used as a technique to assess cleanliness of target samples before transfers. Indeed, before attempting a graphene transfer, the quantity of carbon on the target must be below our detection threshold. Second, once the transfer has been attempted, AES not only gives information about if and how much carbon (graphene) was transferred, but also about eventual contaminants such as oxygen or traces of the graphene support residue. The measurement spot is approximately 2 mm in diameter and the crystals used in our work are 7 mm in diameter. We could therefore in theory measure 3 regions without overlap on the sample, but the alignment between sample and the electron source can be done with at best a few degrees precision, implying that we can only measure on 2 distinct areas before measuring outside of the sample, which gives a strong signal of the insulating sapphires holding the sample down on the sample holder (see section 2.5.1).

As an example, the Auger spectra acquired on a clean Ir(111) crystal and on CVD grown graphene on Ir(111) (grown in our UHV chamber, see section 2.6.2) are shown in figure 2.8. The iridium main transition peak (at 54 eV) corresponds to an NOO transition [150].

The main transition peak of carbon (around 271 eV) originates from the carbon KLL transition [151]. The peak positions are affected by the sample position relative to the detector, the detector work function as well as possible chemical shifts. The latter may be used to detect changes in graphene-surface interaction as will be discussed in section 4.2. In our experiments, the Ir main transition peak was located within 53 eV and 60 eV depending on experiments and this was attributed to a combination of the measurement configuration and chemical shifts. The main carbon peak was located within 270 eV and 280 eV, for the same reasons. The ratio between peak-to-peak intensities of carbon and iridium main transitions can be used for assessing relative quantities of graphene (or carbon) on the iridium surface. According to the spectrum shown in figure 2.8, a monolayer of graphene on a clean Ir(111) crystal was characterized by a peak-to-peak ratio $I_C/I_{Ir} = 1.75$. This value was however not a constant throughout our whole work. For reasons we were unable to explain, after some repairs to our experimental setup and consequent bakeout to recover the UHV conditions, the peak-to-peak ratio changed from a value of $I_C/I_{Ir} = 2.7$ (used as a reference in the first part of our work in chapter 3) to $I_C/I_{Ir} = 1.75$ (used as a reference in our work with PTFE in chapter 4). We were unable to explain this variation in the ratio, but a test conducted by C. J. Powell et al. on multiple Auger spectrometers had revealed that there may be large variations in obtained spectra depending on the model and experimental conditions used [152]. Indeed, kinetic-energy values (peak positions) variations between instruments and groups of up to 32 eV were reported at 2025 eV. More importantly, peak intensity ratios for the main peaks of Cu (60 eV peak intensity / 920 eV peak intensity) and Au (70 eV peak intensity / 2025 eV peak intensity) were found to vary in most cases by a factor of 2 (for Cu) and 5 (for Au) compared to the average values over all experiments (in some cases the factors would be in excess of 38 and 120 respectively, but were attributed to measurement issues) [152]. Although these results date from 1982, a change in the spectrometer may have induced a variation in the peak-to-peak ratios, which fits within this range. To avoid erroneous data interpretation due to variation in the AES spectrometer, reference spectra on CVD grown graphene were frequently acquired for comparison with spectra acquired on samples produced by transfer methods. The equivalent amount of transferred graphene was then calculated in ML, with respect to the most recent reference.

These reference I_C/I_{Ir} values have been used to rapidly assess and quantify graphene transfers *in-situ*. The transfer of a clean layer of graphene onto a clean sample of Ir(111) should be characterized by a I_C/I_{Ir} ratio identical to the calibration one in the case of a full monolayer transfer. A higher value of the ratio is obtained for carbon contamination on the surface and a lower value for a sub-monolayer transfer (both effects may coexist and annealing may reduce surface contamination). For sub-monolayer ratio values, the equivalent monolayer amount was supposed to vary linearly with the ratio. The presence of impurities on the surface prior to or post-transfer (such as oxygen, main peak at 520 eV) can be detected by extending the analysis to energy values corresponding to the suspected elements. In our work, most measurements were carried out between 30 eV
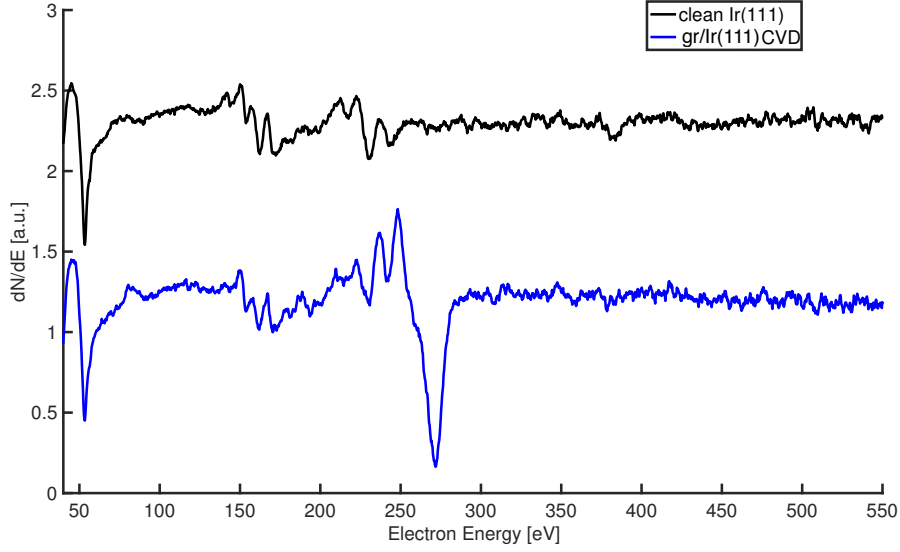
Figure 2.8 – AES spectra of clean Ir(111) and CVD grown graphene on Ir(111). The intensities are normalized to the Ir peak height (at 54 eV) and the spectra are offset for clarity. Primary electron energy 3 kV, 0.3 eV step in analyzer energy. $I_C/I_{Ir} \simeq 1.75$.

and 1000 eV. The minimum detectable quantity is limited by the signal to noise ratio of the experimental setup, as will be discussed in section 4. This ratio is made better by increasing channeltron voltage, which in turn further multiplies the electrons in the electron multiplier before the detector, at the cost of reducing the lifetime of the electron multiplier.

In theory, the ratio of main carbon and iridium peaks can be approximated using the exponential decay of intensity with increasing thickness as mentioned previously [146]. Assuming that graphene is a continuous layer completely covering the Ir(111) surface, the intensities for both C (I_C) and Ir (I_{Ir}), are given respectively by :

$$
\begin{cases}
I_C = S_C \cdot I_0 \cdot \lambda_C(272) \cdot \left(1 - \exp\left(\frac{-d}{\lambda_C(272)}\right)\right) \\
I_{Ir} = S_{Ir} \cdot I_0 \cdot \lambda_{Ir}(54) \cdot \left(\exp\left(\frac{-d}{\lambda_C(54)}\right)\right)
\end{cases}
\tag{2.6}
$$

The relative sensitivities for the C peak at 272 eV and the Ir peak at 54 eV are calculated with equation 2.5 and the reference values in the handbook of Auger electron spectroscopy [149]:

$$
S_C = 0.2 \quad \text{and} \quad S_{Ir} = 0.25
\tag{2.7}
$$

The carbon to iridium main peak intensity ratio can then be calculated using equations 2.4, 2.7, the thickness of graphene and the interlayer spacing in Ir(111) (0.335 nm and

0.22 nm respectively) :

$$\frac{I_{\mathrm{C}}}{I_{\mathrm{Ir}}} = \frac{0.0592}{0.05225} = 1.13 \tag{2.8}$$

This value is smaller by 35 % than the lowest experimental value we obtained, even if the moiré superstructure observed in our STM analysis confirmed that we had only a single layer of graphene on Ir(111). In addition, we carefully checked that after cleaning the Ir crystal by sputtering and annealing, no carbon had segregated to the surface (confirmed by both Auger and STM). The discrepancy can be related to the simplicity of the model treating the gr/Ir(111) as a continuous system, and thus neglecting the real atomic structure.

An estimation for the Auger main peak ratio that should be observed for two layers of graphene on Ir(111) can be obtained by setting $d = 2 \cdot 0.335$ in the previous equations, the ratio is then given by :

$$\frac{I_{\mathrm{C}}}{I_{\mathrm{Ir}}} = \frac{0.105}{0.03125} = 3.36 \tag{2.9}$$

Comparison to the MLG/Ir(111) theoretical value suggests that BLG/Ir(111) should be characterized by a $I_{\mathrm{C}}/I_{\mathrm{Ir}}$ ratio 3 times larger. This result is used as a reference for the transfer of a single layer of graphene on top of gr/Ir(111) in sections 3.5.1 and 4.7. Similarly to the sub-monolayer case, the estimated coverage between a single and two layers was considered to vary linearly with the ratio.

Throughout our measurements, the electron gun parameters were 2.4 A and 3 kV and the channeltron (electron multiplier) high voltage was set to 1300 V.

2.4 Scanning Tunneling Microscopy

Scanning Tunneling Microscopy is a very powerful tool enabling atomic-resolution probing of an electrically conducting surface. Invented in 1982 by researchers at IBM in Switzerland [153], their invention earned them a Nobel Prize in 1986 and has since then unlocked the door to understanding phenomena taking place at surfaces at the atomic scale. The principle on which this technique relies is the quantum tunneling effect, in which electrons can tunnel through a potential barrier. Indeed, by bringing a conductive pointed tip (STM tip) in proximity (less than 1 nm) to a conducting sample surface, the electrons from the tip may tunnel through the vacuum to the sample or vice-versa. The distance at which this effect can be observed is limited by the overlap of the quantum wavefunctions of both the tip apex atom electrons and the underlying surface atoms' electrons. In general, there are two operation modes for an STM, in the first, constant height STM, the surface of the sample is scanned and the tip is maintained at a constant distance from the sample, supposing the sample is flat. In this mode, the tunneling current is then acquired as a function of the tip (x-y) position (determined by piezoelectric transducers). In the constant current operation mode, the tip is approached to the surface or retracted from it while scanning to keep the tunneling current constant by means of a feedback loop which outputs the control voltage to the z axis transducer based on the difference between the measured current with respect to the target current. In this mode, the control voltage required to maintain constant current is acquired as a function of the tip position. This is the mode in which our experiments were carried out.

Typically an STM consists of a sharp metal tip mounted onto a head equipped with an approach and scanning mechanism, connected to an electronic control unit as is shown in figure 2.9. Our home-made STM head [154, 155] features an approach mechanism consisting of semi-spherical "feet" that allow the whole STM head to move up and down the ramps on the sample holders (see fig. 2.12). Inside the STM head, the tip is inserted into a piezoelectric tube (see fig. 2.9) which enables scanning of surfaces by applying a control voltage to the piezoelectric transducers (two for x,y sample plane and one for tip height (z)).

Because of the proximity of the tip to the surface (sub-nm distance), the system is extremely sensitive to vibrations and both STM head and sample must be decoupled from the exterior. This is performed by using air dampers for the UHV chamber in which the STM and sample are mounted, as well as decoupling the STM head laying on the sample ramps from the chamber by using a damping stack [45].

In order to obtain an atomically sharp tip, a commonly used technique consists of electrochemically etching a tungsten (W) wire [156]. A meniscus of an etching solution (typically KOH) is formed in a metal loop by dipping in the solution (as one would make soap bubbles). The W wire is connected to the cathode of a generator whilst the metal loop is connected to the anode. As current is fed into the loop and to the wire by ions in
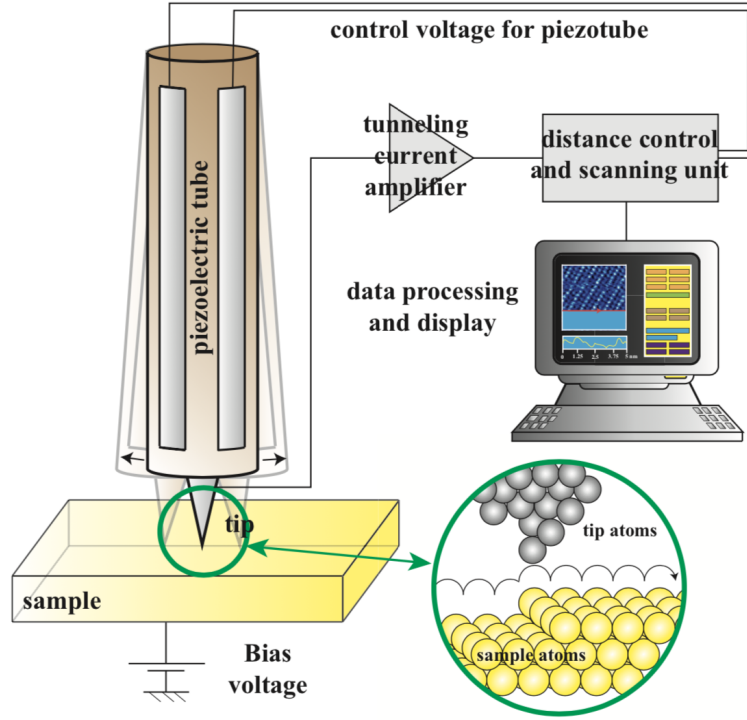
Figure 2.9 – Schematic of an STM [46]. The main components are an atomically sharp tip in a piezoelectric tube, controllable in x,y and z directions, a current amplifier, and a control unit for feedback. The tip height z needed to provide constant current is recorded as a function of the lateral position x and y.

the etching solution, the W wire is etched at the meniscus and becomes very thin until the bottom part drops by gravity into a beaker filled with foam. The top part of the dropped piece of wire is then used as the tip, which at that point has only a few atoms at the point of rupture.

Tunneling current :

The Fermi levels of both tip and sample can be represented as shown in figure 2.10. Without bias voltage, electrons tunnel through the gap in both directions with equal probability. Applying a bias voltage between the sample surface and the tip shifts the relative Fermi levels and a current can be measured since more electrons tunnel from the sample to the tip through the vacuum gap (represented by the distance d) or vice-versa (depending on which Fermi energy is higher). This tunnelling current is proportional to the local density of states (LDOS).

An approximate model of the tunnelling observed in an STM setup was proposed by Tersoff and Hamann [157], based on the Bardeen transfer hamiltonian theory [158]. To simplify the problem, the model considers the separation of the Hamiltonian describing the system into subsystems with known hamiltonians and neglects the interaction transfer
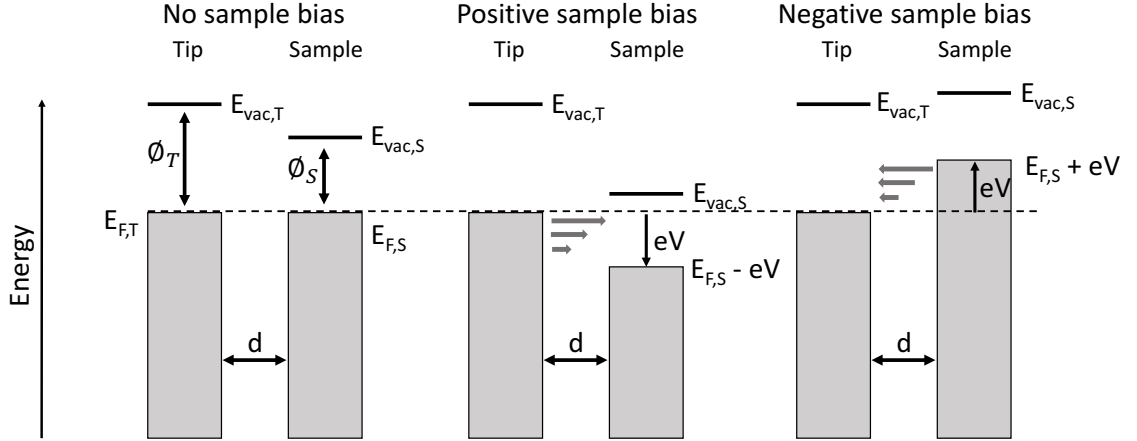
Figure 2.10 – Schematic of the Fermi levels, vacuum levels and work functions for both tip and sample atoms. Without bias voltage, the work functions of both the sample and the tip are assumed equal ($\Phi_S = \Phi_T$). Bias applied to the sample (positive or negative) shifts the Fermi level of the sample with respect to the tip and allows tunneling (gray horizontal arrows).

hamiltonian. This however allows sufficient understanding of the ability of STM to reach atomic resolution. More accurate models have been proposed, but will not be explained in this thesis. All models, however, agree on the exponential dependence of the tunnelling current on the sample-tip distance defined in equation 2.10.

$$I_t \propto e^{-2\kappa d} \qquad \text{with} \qquad \kappa = \frac{\sqrt{2m\phi}}{\hbar} \tag{2.10}$$

Where m is the mass of an electron and ϕ is the work function for tunneling. The exponentially decaying tunneling current with distance d (between sample and tip) is what allows the STM to sense picometer variations in height. Indeed, increasing the distance by only one Å leads to a decrease by almost an order of magnitude in the tunneling current.

47

2.5 UHV experimental setup and sample preparation

Transfer experiments were carried out and characterized in the UHV environment. In this section, we briefly describe the home-made UHV chamber, designed and assembled by Nicolas Weiss [154, 155]. We then describe the sample preparation technique we use in our work.

2.5.1 The UHV chamber
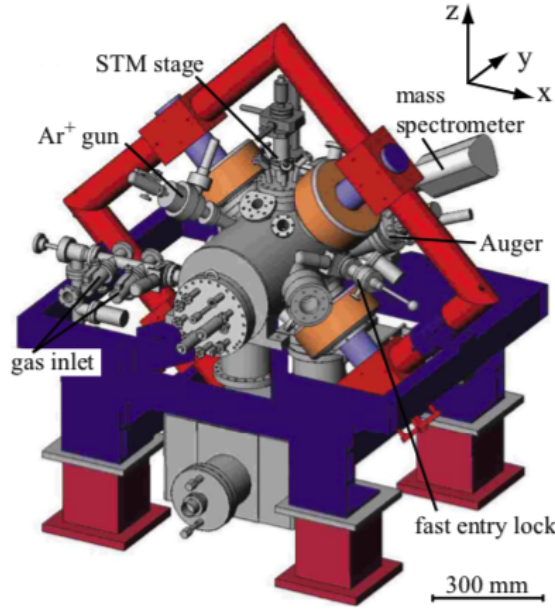
Figure 2.11 – Drawing of the UHV chamber showing how the poles, coils, and yoke are mounted on the chamber. The positions of STM, Auger, Ar$^+$ ion gun, and fast entry lock (load-lock) are indicated. Adapted from [45].

Our home-built UHV experimental setup in the LNS laboratory at EPFL consists of a large UHV chamber capable of reaching pressures lower than $1 \cdot 10^{-10}$ mbar after baking. It is equipped with a main preparation stage, on which samples can be prepared as described in section 2.5.2. A variable temperature STM (see section 2.4) can be lowered onto the sample (on the main preparation stage) and a Magneto-Optical-Kerr-Effect (MOKE) detector can be used for assessment of magnetic properties of samples. This stage is also used for the CVD growth of graphene or for atom deposition by MBE. Using a rotating wobble stick adapted for the experimental chamber, samples can be moved onto a second stage, which consists of an L-shaped manipulator, with a vertical axis holding the sample holder and a horizontal axis which allows to rotate the sample holder in order to place it in the desired position (for either AES or MBE with a second evaporator). This stage is also equipped with a heating filament.

Samples are mounted onto sample-holders as depicted in figure 2.12 and are electrically

isolated from the holder with sapphire rings. Three springs hold the sample down by pressing on the sapphire and the ramps for the approach of the STM tip are mounted on top. These mounted samples are then inserted into the UHV chamber by means of a load-lock, which can be pumped to a pressure of $1 \cdot 10^{-7}$ mbar within a few hours.
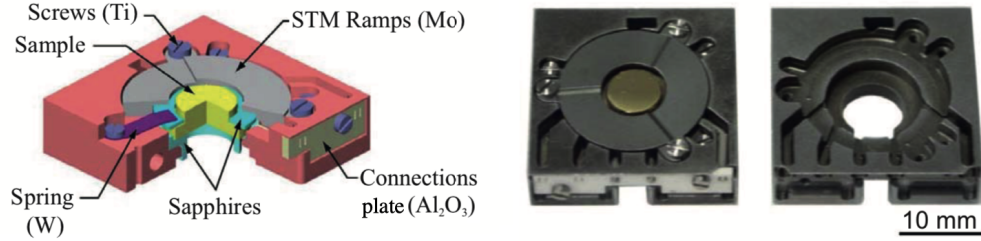
Figure 2.12 – Schematic (left) and images (right) of the sample holder used in our experimental setup. The sapphires isolate (electrically) the sample from the sample holder. Adapted from [159].

Our setup can accommodate 3 sample holders in UHV, with an extra parking spot allowing one to move the samples around. The sample holders are secured into the main stage using a spring locking mechanism, which ensures proper electrical (via 3 pins, one for sample bias and 2 for thermocouple) and thermal contact. A filament and application of a high voltage bias between sample and ground allow annealing to temperatures higher than 1600 K. Conversely, the sample can be cooled down to temperatures of about 70 K via a helium flux cryostat in thermal contact with the sample stage via Cu braids. The STM head, when lowered onto the sample holder, follows the variations in temperature of the main stage (and sample).

2.5.2 Sample preparation

All the single crystals used in this thesis (Ir(111), Ni(111) and Cu(100)) were acquired at the Surface preparation laboratory [160]. They are cylindrical and have a hat shape with the upper part having a diameter of 7 mm and the lower 9 mm. On that lower part, the samples are clamped between two sapphire rings into the sample holder shown in figure 2.12. Before each experiment, the single crystals are cleaned from adsorbates that formed after exposure to air, from previous MBE or CVD grown layers, or from transfer residues. This is done by repeated cycles of sputtering and annealing. During sputtering, the sample surface is bombarded by Ar^+ ions, which causes the surface to erode and to eject atoms into vacuum. We use Ar^+ ions with 1.2 keV kinetic energy and scan the beam over the sample for 10 to 120 mins at room temperature. The current on the sample during sputtering is in the range of $I \simeq 1$ μA. This is followed by annealing to a temperature roughly equal to 2/3 of the melting temperature for 30 - 120 seconds, during which the rough surface is smoothened to obtain large atomically flat terraces of the specified orientation. In our experiments, the Cu sample was annealed to 600 ℃, the

SiC   PDMS stamp   PTFE
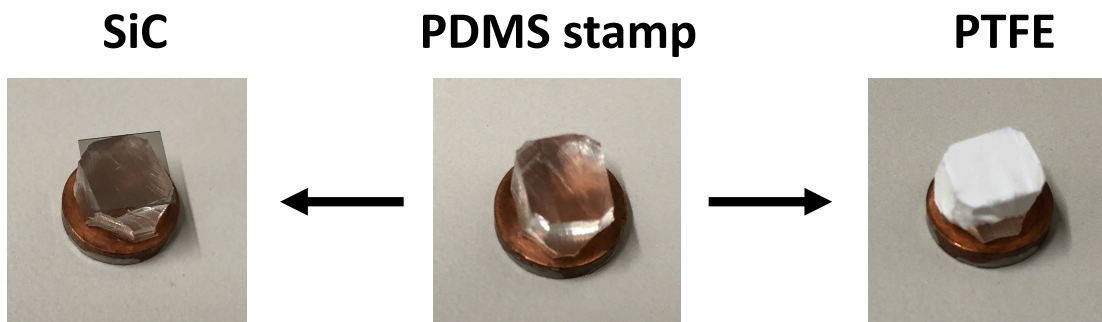
Figure 2.13 – Transfer stamp setup for transfers assisted by PVA, SiC or PTFE. The transparent PDMS stamp is glued to the Cu chip and used as the stamp for PVA-assisted transfer. On the left, the gr/SiC is glued on top of the PDMS for transfer from SiC. On the right, the gr/PTFE tape is wrapped on the surface of the PDMS for PTFE-assisted transfer.

Ni(111) to 900 ℃ and the Ir(111) to 1100 ℃. Temperatures were measured with a type K thermocouple on the base of the sample.

After multiple cycles, the cleanliness of the surface is checked with AES by comparison to reference Auger spectra found in literature [149]. After confirmation by AES that the surface is clean, graphene can either be grown on the single crystal as described in section 2.6.2 in the case of gr/Ir(111) or the clean crystal can be used as a target for graphene transfer as demonstrated in our work.

2.5.3   Graphene transfer process

For the transfer methods that we developed, a 5 mm-radius, 2 mm thick cylindrical piece (chip) of Cu was cut to fit the standard sample-holder shown in figure 2.12. A 5 mm thick piece of PDMS was molded using Sylgard 184 Silicone Elastomer [161] and roughly cut to a cylindrical shape of 3 mm radius before being glued on top of the Cu adapter with UHV-compatible silicone glue (DOWSIL 744 RTV Adhesive Sealant [162]) (see fig. 2.13 center image). This flexible stamp was used as a base to carry the supported graphene layer. As will be shown in our work, it was used for PVA-assisted transfer (see section 3.5), transfer from SiC (see section 3.7), where the SiC is glued on the PDMS stamp, and for PTFE-assisted transfer, where PTFE-supported graphene is wrapped on the PDMS stamp (see chapter 4).

For transfer, the target sample is placed on the L-shaped manipulator and the rotating wobble stick is used to stamp the supported graphene onto the target sample (inspired by the wafer-bonding principle). The pressing process is shown in figure 2.14.

The wobble stick to which the graphene-carrying stamp is attached can be moved in all three dimensions and is free to rotate around its longitudinal axis. The L-shaped
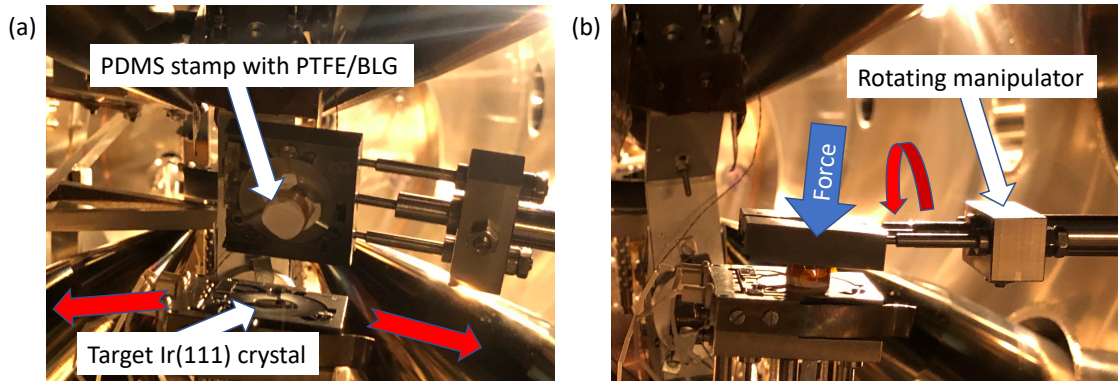
Figure 2.14 – UHV transfer procedure. (a) PDMS stamp with PTFE/BLG mounted, ready for transfer onto the target Ir(111). The target Ir(111) on the L-shaped manipulator can be rotated, giving it a motion along the red arrows. (b) Target and stamp in contact, the stamp is pressed against the target.

manipulator allows for rotation of the target sample around a pivot point 15 cm from the sample. The direction of motion for both the wobble stick rotation and the L-shaped manipulator are represented by red arrows in figures 2.14 (a) and (b). Once the target and stamp are properly (visually) aligned, the two are pressed (generally at RT with a force of approx. 30 N) against each other with the wobble stick and held in position for 10-20 seconds (fig. 2.14 (b)). For other transfers involving different supporting layers, the setup is identical.

2.6   Graphene growth on Cu and on Ir(111)

Graphene was grown by CVD, both on polycrystalline Cu in a reactor, and on Ir(111) in our UHV chamber. The graphene grown on Cu was used as our source of graphene for transfers, whereas the graphene on Ir(111) was either used as a reference or as a target for transfer in order to form BLG/Ir(111).

2.6.1   Graphene growth on polycrystalline Cu

Graphene growth by CVD on polycrystalline copper is the simplest way to grow large-area, low-defect graphene [82]. The growth method uses the Cu substrate as a catalyst for decomposition of a precursor carbon-containing gas to form a layer of graphene in a hydrogen environment [163]. The process is in general self-limited by the fact that once the Cu surface is covered by graphene, the catalyst Cu is no longer active and no more decomposition of the precursor gas occurs.

Changing the relative pressures of the precursor gas (CH_4) and the hydrogen influences the properties and growth quality of the graphene [164]. These parameters were optimized by A. Magrez for our reaction chamber in order to yield the highest quality monolayer graphene.

First, a 25 μm thin sheet of Cu is cut into a 1.5×4 cm^2 piece. For cleaning, it is placed in acetone for 3 minutes before being rinsed in isopropanol or methanol for 2 minutes. The sheet is then dried with a nitrogen gas gun.
Once clean and dry, the Cu sheet is placed at the center of a quartz tube in the reactor. The volume in the quartz tube is then pumped to a pressure inferior to 5×10^{-3} mbar. Once this vacuum has been reached, H_2 is added in the quartz tube to a pressure of 4 mbar.
The Cu sheet is heated up to 1031 ℃ in the reactor and annealed at that temperature for an additional 30 minutes (this temperature was determined by placing a thermocouple at the position of the sample with identical reactor settings). Methane (CH_4) is then added to the H_2 in the quartz tube until reaching a pressure of 18 mbar. At this temperature, on the catalyst Cu surface, the methane is decomposed and forms a monolayer of graphene on the Cu surface [82], [165].
After 3 minutes of growth, the methane and hydrogen are pumped out while slowly cooling the Cu sheet at a rate of 15 ℃/min.

After growth, the Cu sheet is covered with graphene on both sides, and because of the radial symmetry of the growth reactor, the graphene is of similar quality on both sides. After every growth, Raman spectroscopy was used to characterize the quality of the growth according to the discussion in section 2.1.1. In figure 2.15 the typical spectrum of

graphene on Cu grown with this method (averaged over 10 measurement points taken at different locations of the 1.5 × 4 cm^2 sample) is shown. The strong Cu background can be seen and the D, G and 2D bands are labelled. The resolution of the acquired Raman spectra do not allow us to distinguish the D' band from the G band suggesting that defects are dominated by sp^3 type defects (see section 2.1.1). In order to fit the peaks, the Cu background was subtracted. The main peak positions, FWHM and ratios are given in Table 2.1. Each one of the values is given with a confidence interval evaluated as the standard deviation of the dispersion of the values measured in the different spots.
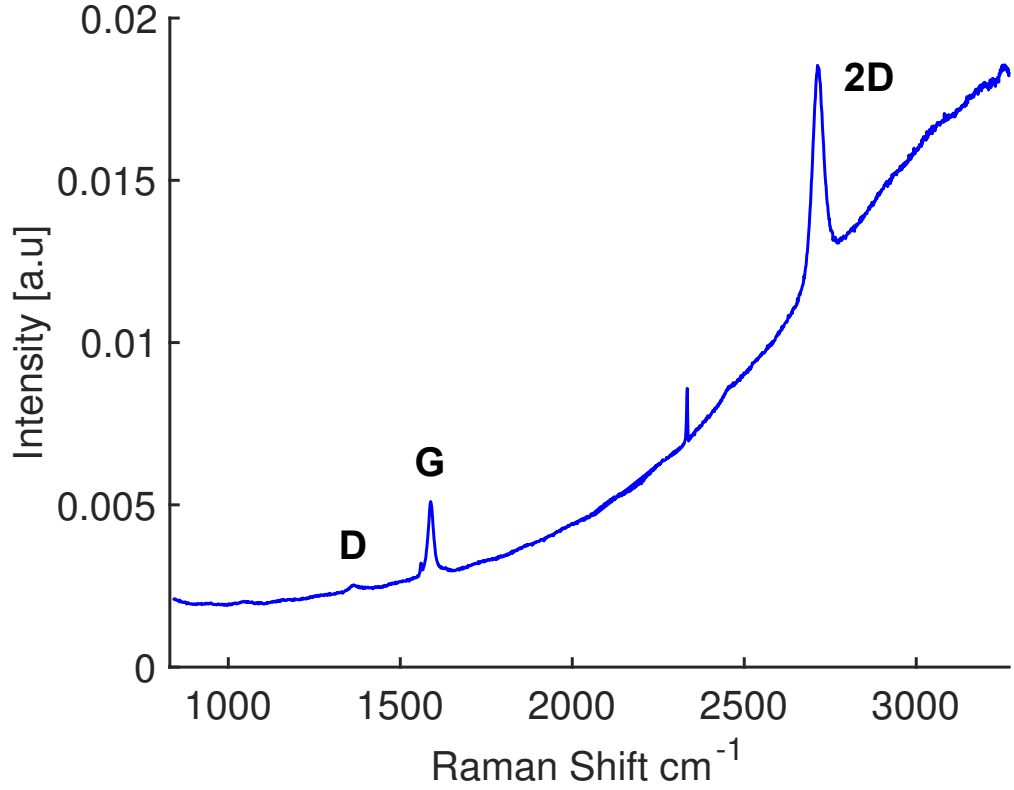
Figure 2.15 – Raman spectrum of CVD-grown graphene on Cu. The sharp peak at 2330 cm^{-1} is a measurement artefact. 488 nm laser wavelength, 2400 l/mm grating, 25 mW power, exposition time of 50 s, averaged over 15 sample regions.

Table 2.1 – Raman characterization of CVD grown graphene on polycrystalline Cu averaged over 10 sample regions. The values are given with a confidence interval evaluated as the standard deviation of the dispersion of the values measured in different spots. The FWHM and peak positions are given in cm^{-1}.

2D FWHM	2D position	G FWHM	G position	$I(G)/I(2D)$	$I(D)/I(G)$
34±3	2714±4	18±2	1588 ±2	0.35±0.07	0.10±0.03

The $I(G)/I(2D)$ ratio for this CVD grown graphene corresponds to what is expected for MLG (see Table 1 based on 50 references in [166]). The 20 % confidence interval is believed to be due to different substrate interactions depending on local variations in the

underlying Cu sheet quality.

The average $I(D)/I(G) = 0.10$, indicates that the graphene is of high quality [129–131] and the large (30 %) confidence interval is believed to be due to local variations in graphene quality, which may be due to the Cu substrate or to localized defects in the graphene lattice. This ratio varied between samples and more frequently our samples were characterized by $I(D)/I(G) \simeq 0.15$. Worse values of up to 0.3 were also observed, but in this case the gr/Cu was not used for our transfer procedures (we used CVD grown graphene with a maximum $I(D)/I(G) \simeq 0.15$). These large differences in defect density are attributed to the quality of the Cu growth substrate, variations in the partial pressures of methane and hydrogen, as well as post-growth cooling rates and Cu substrate placement in the quartz tube. Indeed, in some growths, if partial pressures varied by 20 % or more from the optimum parameters described previously, highly defective graphene was measured on the Cu substrate.

2.6.2 Graphene on Ir(111)

It is well known that high quality graphene with very large domains can be grown on Ir(111) by CVD in UHV [13, 14, 167]. Graphene on Ir(111) is characterized by a well aligned incommensurate (9.32 × 9.32) moiré superstructure that arises from the slight mismatch between the two lattice constants of graphene (a = 2.46 Å) and Ir(111) (in-plane a = 2.73 Å). There are (10.32 ± 0.17 × 10.32 ± 0.17) graphene cells per moiré cell, and the graphene layer has been shown to be slightly compressed (0.4 %) in comparison to a carbon layer in bulk graphite [167].

Considering the reciprocal lattice vectors $\vec{k}_{Ir}$ and $\vec{k}_{gr}$, the moiré reciprocal lattice vector is given by [167] :

$$\vec{k}_{Moir\acute{e}} = \vec{k}_{gr} - \vec{k}_{Ir} \tag{2.11}$$

And by expressing the vectors in real space, the distance between Moiré maxima ($d_{Moir\acute{e}}$) is given by :

$$\frac{2\pi}{d_{Moir\acute{e}}} = \frac{2\pi}{d_{gr}} - \frac{2\pi}{d_{Ir}} \leftrightarrow d_{Moir\acute{e}} = \frac{d_{gr} \cdot d_{Ir}}{d_{Ir} - d_{gr}} = 25.3 \text{ Å} \tag{2.12}$$

In our work, prior to growth, an Ir(111) single crystal is cleaned by repeated cycles of sputtering and annealing (see preparation method in section 2.5.2). The clean Ir(111) crystal is heated to 1400-1450 K in the UHV chamber with base pressure in the 10^{-10} mbar range and held at this temperature. After 20 seconds, a precursor gas (ethylene C_2H_4 in our case) is then added into the UHV chamber to a pressure of $1 \cdot 10^{-6}$ mbar and kept for 100 seconds (approximately 100 langmuir), after which the heating is shut off and the gas is pumped out.
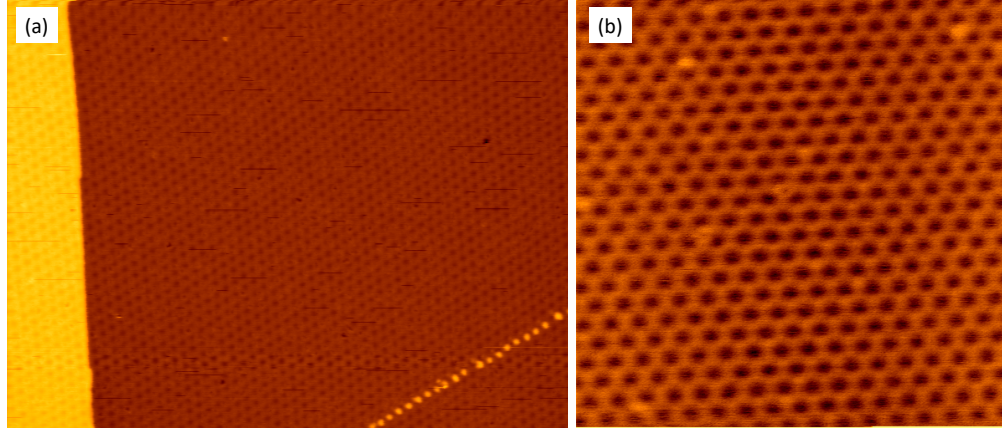
Figure 2.16 – 1500 Å × 1150 Å (a) and 600 Å × 600 Å (b) STM images of the moiré formed by CVD grown graphene on Ir(111) (V_t = +1.7 V, I_t = 10 nA, T = 300 K)

Figure 2.16 shows STM images of graphene on Ir(111) grown with this procedure in our UHV chamber. The moiré confirms that graphene covers the whole Ir(111) surface, and is continuous over the 2 Å iridium step on the left part of figure 2.16 (a). In our work, studying the moiré continuity and domain size constitutes a way to characterize the transfer of graphene onto Ir(111) by STM *in-situ*.

As was mentioned in section 2.1.1, the high fluorescence of Iridium makes Raman spectroscopy unsuited for the evaluation of graphene quality [125]), and thus gr/Ir(111) can be characterized by Auger spectroscopy (see section 2.3) and by STM in our lab, or by XAS at the SLS synchrotron facility.

3 Unsuccessful transfer methods

This chapter describes the different approaches and steps adopted to reach our goal of graphene transfer in UHV. Our approach is inspired by wafer-bonding, a method commonly used in the industry to bond one single crystal on-top of another when the two don't grow on each other by epitaxy, for example for Si on insulator technologies [168–173]. We use a variation of wafer bonding using the fact that the bonding to the target substrate, which can be chemical, as is the case for graphene on iridium, is stronger than to the support layer. Such a procedure is depicted for graphene transfer in figure 3.1. A substrate with graphene on top is placed face-down onto a target sample. The two are then pressed together with force **F** for time $t_{Transfer}$. The support layer is then lifted up, leaving only the graphene layer on the target.
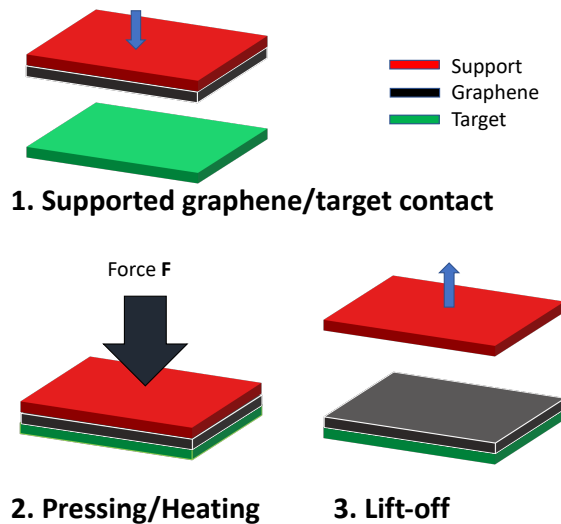
Figure 3.1 – Wafer bonding procedure, here with a support layer (in red) which can be for example a TEM grid, SiC, BLG on Cu. The supported graphene is pressed against the target with force **F** and the support is lifted after transfer.

Due to the atomic thickness of graphene, a supporting layer is mandatory; graphene cannot

Table 3.1 – Methods for isolation of graphene from its growth substrate and support layers for graphene transfer. Each line is a different graphene isolation method and each column is a different support layer. Experiments that were unsuccessful are marked with a (-), successful ones are marked with a (+) and those not attempted are marked as NA.

	Naphtha.	PVA	PTFE	MLG/metal	TEM grid	SiC
Electrochem. bubbling	-	-	NA	NA	NA	NA
Chemical etching	NA	NA	+	NA	NA	NA
Mechanical exfoliation	-	+	NA	-	NA	NA
Commercial	NA	NA	NA	-	-	-

be manipulated free-standing without being damaged. As was mentioned previously, performing a transfer in a UHV environment implies that the transfer procedure should not require the *ex-situ* removal of the support layer post-transfer. Therefore, the ideal transfer method should involve a supporting layer that is weakly bound to graphene and that would detach from it within the UHV environment.

Furthermore, only a single graphene layer should be detached upon transfer in order to have full control of the number of graphene layers on the target. Systems such as graphite, despite not requiring removal of a supporting layer after transfer, do not allow control of the number of layers.

Table 3.1 summarizes the methods that were attempted in order to isolate and support graphene for subsequent transfer. Each line shows a different process with which a graphene layer is detached from its growth substrate, or in the case where we did not perform the isolation, it is marked as commercial, and each column is a different support layer that was used. The MLG/metal column is for samples for which graphene was supported by another graphene layer on a metal, such as gr/Cu or gr/Ir(111). The experiments marked with NA were either not attempted for incompatibility reasons with respect to our goal, or they had not been prepared by us but were commercial. The other experiments, unsuccessful (-) and successful (+) are described in this chapter before we report in the following chapter on the most successful approach based on PTFE-assisted transfer.

Although the PVA-assisted transfer described in section 3.4 was successful at transferring graphene, it did not meet the UHV-compatibility condition since PVA had to be removed in hot water after graphene transfer.

3.1 TEM grid supported graphene for transfer

A commercially available TEM grid-supported graphene sample meets the requirements mentioned above. Indeed, the graphene is supported by the TEM grid and a holey (perforated) amorphous-carbon (a-C) film, which is necessary because graphene cannot be suspended over the TEM grid holes without breaking (see section 1.3). The benefits of having a holey a-C layer are two-fold. First, the interaction between a-C and graphene should be of the weak van-der-Waals type and second, the holey nature of the a-C sheet reduces the surface in contact, which should lower the total binding force with graphene, making it easier to detach.

Commercially available graphene on a TEM grid (PELCO Single Layer Graphene TEM Support Films on Lacey Carbon, 300 Mesh Copper Grids) was purchased from TED Pella [128]. The substrate consists of a TEM grid with equally spaced square holes of 54 μm width. On top of this grid, lies the layer of holey a-C with 5 μm wide holes and the graphene. According to the manufacturer, graphene was transferred onto the TEM grid/a-C using a wet method (see section 1.3).

The Raman spectrum of the suspended graphene (over a-C holes) on the TEM grid is shown in figure 2.3. The graphene is characterized by an average $I(\text{D})/I(\text{G}) = 0.077$, with values ranging between $I(\text{D})/I(\text{G}) = 0.09$ and $I(\text{D})/I(\text{G}) = 0.055$, indicating high-quality graphene.

3.1.1 Transfer to Cu in air

Following the wafer-bonding procedure, transfers were attempted in air using clean polycrystalline copper as a target. Copper was chosen because of the chemical bond it is expected to form with graphene, which should be stronger than the vdW force between graphene and a-C [174], therefore allowing detachment and transfer of graphene.

A 5×5 mm^2, 25 μm thick piece of copper (chosen for its flexibility and adaptability to other surfaces) was immersed for 24 hours in acetic acid (CH$_3$COOH) in order to eliminate the oxidized surface layer. The sample was then cleaned in DI water and dried with a nitrogen gun. The TEM grid was then placed on top of the clean Cu with the graphene facing downwards and the two were pressed against each other by placing a weight on top of the TEM grid at temperature T, during time t$_{\text{Transfer}}$, which also includes the heating time (approx. 10 minutes to ensure the Cu and TEM grid are at the target temperature).

Table 3.2 summarizes the transfer parameters for all experiments that were carried out, with transfer temperature ranging from -20 ℃ to 150 ℃, pressing force from 3 to 40 Newtons and transfer time between 30 minutes and 16 hours. To cool the sample down to -20 ℃, the Cu and TEM grid with the weight on top were placed in a freezer.

Table 3.2 – Temperature T, pressing force (F) and transfer times parameters attempted for graphene transfer from the TEM grid onto Cu.

T [℃]	F [N]	Transfer time [min]	Cooling time [h]
20	6.5	30	0
20	10	30	0
20	20	30	0
20	40	30	0
50	40	30	0
95	3	30	0
95	3	30	0.25
95	3	60	15
95	9	45	16
105	9	50	16
-20	3	120	0

After each transfer attempt, the TEM grid was lifted and the area of the Cu target that had been in contact with the graphene was marked. Raman spectroscopy was then used to assess whether graphene had been transferred by analyzing multiple points over the contact area.
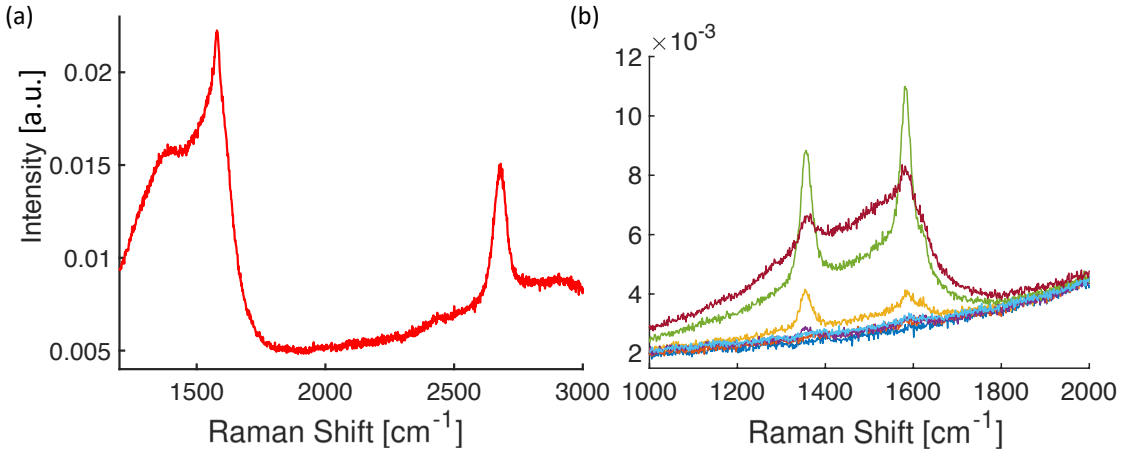
Figure 3.2 – (a) Raman spectrum of graphene supported by a-C. (b) Raman spectra of gr/Cu post-transfer from the TEM grid onto the Cu target (at RT with 40 N force). Each spectrum is acquired on a different area of the target Cu. 488 nm laser wavelength, 2400 l/mm grating, 25 mW power, exposition time of 50 s, averaged over 5 sample regions.

Figure 3.2 (a), shows the Raman spectrum measured on graphene on the a-C. The a-C spectrum is characterized by a large band that encompasses both D and G bands typically observed in graphene. Indeed, the distinct D and G bands of the suspended graphene shown in figure 2.3 are no longer distinct but mixed under one large peak with a shoulder

at around 1400 cm^{-1}.

In figure 3.2 (b), the Raman spectra around the G and D bands for 7 points measured on the contact area post-transfer at room temperature with 40 N pressing force are shown. The Cu background was not subtracted. The Raman spectra show that only 3 of the measured areas had visible D and G bands which are a combination between the suspended graphene and the graphene on a-C (compare figures 2.3 and 3.2 (a)). The spectra are characterized by $I(D)/I(G)$ values that correspond to those that would be obtained for an unordered structure such as a-C [175, 176], again suggesting a-C was transferred with the graphene. Its high thickness in comparison to the single layer of graphene makes its contribution large.
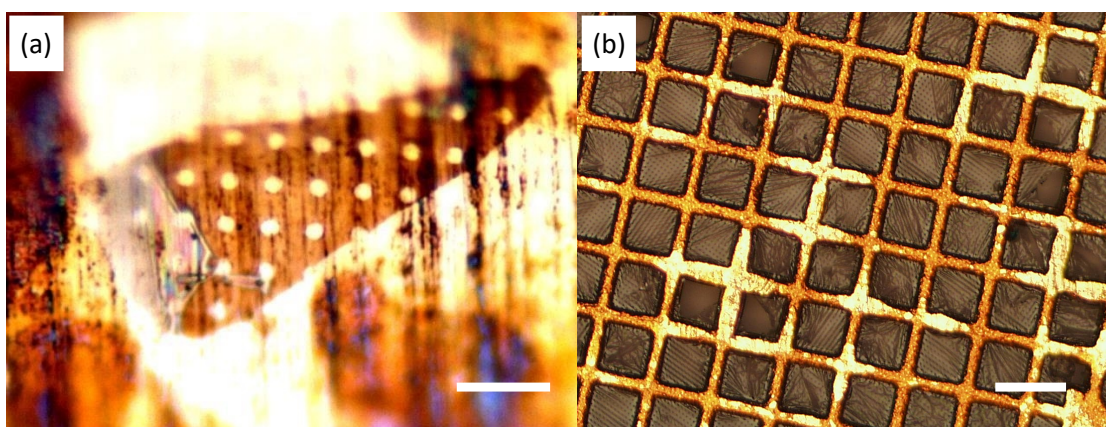
Figure 3.3 – Optical microscope images showing (a) a-C transferred onto the Cu surface and (b) The TEM grid (in gold) with the damaged holey a-C sheet on top. The white scale bars on each image measure respectively 10 μm and 100 μm.

Figure 3.3 (a) is an optical microscope image of the a-C on the Cu target after transfer at -20 °C with 3 N pressing force. Further inspection of the TEM grid post-transfer revealed that the a-C sheet had been broken and torn in multiple locations (see fig. 3.3 (b)), again suggesting that when graphene was transferred, a-C was also transferred with it, in varying amounts, depending on the parameters.

In order to determine whether graphene could be transferred without simultaneously transferring the a-C, a piece of scotch tape was applied to the surface of the gr/a-C/TEM grid and lifted to delaminate the graphene from the grid. This test revealed that graphene was detached, but the underlying a-C was too. Indeed, visual inspection of the TEM grid under a 20× objective microscope showed that the holey a-C was no longer on the TEM grid. This test shows that the binding force between the graphene and a-C is larger than that between a-C and the Cu TEM grid, making it impossible to transfer only the graphene sheet using this technique. This could be attributed to a stronger than vdW bond between graphene and a-C which could be due to contamination from the sample preparation, which according to the manufacturer is done by chemical etching.

Further, if a-C is only very weakly bound to the TEM grid, the weakest bond breaks, thus detaching both graphene and a-C from the TEM grid.

These negative results demonstrated the need of a support that could either be removed after transfer without residue, or a supported bilayer of graphene from which a single layer could be detached, both of which we describe in what follows.

3.2 Commercial BLG for transfer

A good candidate fitting the requirements for the UHV transfer is bilayer graphene. Indeed, two graphene layers in HOPG are bound by weak van der Waals forces and should transfer to a stronger-bonding surface such as Cu. Ideally, two stacked layers of graphene would be isolated from bulk HOPG and placed on a flexible support for transfer. However, as mentioned previously, the processes that are used to isolate graphene layers from HOPG give very little control on the number of layers. Alternatively, bilayer graphene can be obtained by CVD, by segregation of C atoms from bulk substrates or by mechanical stacking (see section 1.4).

In order to grow BLG/Cu, we applied the same experimental procedure as the one described in section 2.6.1, but with increased H_2 pressures (10-20 mbar), which has been shown to yield a higher amount of graphene layers [177, 178]. Raman spectra of samples grown that way showed overall a low quality of graphene and large spatial variations of quality and number of layers. We therefore abandoned the CVD approach for BLG and turned instead to a commercial option to guarantee a uniform bilayer of graphene.
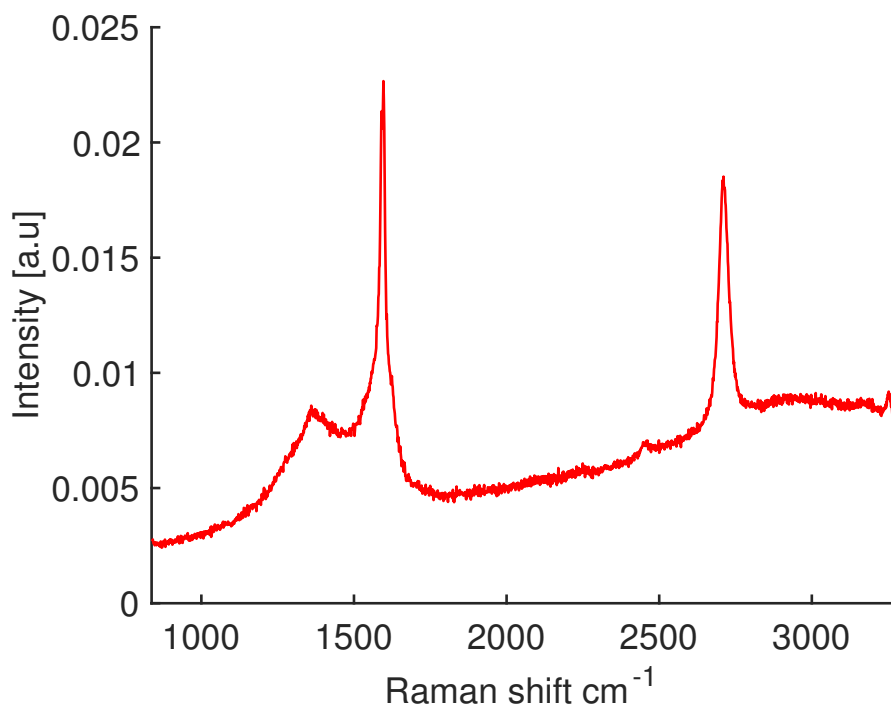
Figure 3.4 – Raman spectrum of commercial BLG on a TEM grid. Measurements acquired on the free-standing parts of graphene spanning over the 6.5 μm holes of the Cu support grid. 488 nm laser wavelength, 2400 l/mm grating, 25 mW power, exposition time of 50 s, averaged over 5 sample regions.

Bilayer graphene on a TEM grid was purchased from TED Pella (PELCO 2-Layer Graphene on Ultra-fine 2000 Mesh Copper TEM Grid supported by 1 x 2mm Synaptek

Slotted Grid) [128]. Raman spectra, as the one shown in figure 3.4, were acquired as a reference prior to any transfer attempts on the BLG/TEM grid. Although the G and 2D bands are sharp and are characterized by $I(G)/I(2D)< 2$, which is considered to characterize multiple layers of stacked graphene 2.1.1, the shape of the spectrum between the D and G bands (around 1500 cm^{-1}) is typically attributed to disordered systems such as a-C, as was shown for the graphene on a-C in the previous section (see fig. 3.2 (a)). Unlike the single layer graphene on a TEM grid, the BLG was not supported by an a-C layer, but was instead free-standing between the 6.5 μm holes of the ultra-fine copper grid, implying that the amorphous signal was due to the BLG, which was of low quality. Further, the 1 x 2 mm^2 bilayer graphene was slightly lower than the rest of the grid, making it impractical for transfer with the wafer-bonding approach. This motivated the homemade production of bilayer graphene by mechanical stacking of two monolayers grown by CVD (see section 3.4.2).

3.3   Naphthalene-assisted transfer

It was shown that polyaromatic hydrocarbons such as naphthalene ($C_{10}H_8$) could be used as a support layer for the transfer of graphene [179,180]. The advantage in using naphthalene lies in the fact that it should easily evaporate upon heating, leaving no residue, making it an ideal transfer supporting layer.

In the original method described by Chen & al., naphthalene is first drop-coated onto the graphene on its growth substrate. The naphthalene/gr/Cu is then immersed in an etching solution to remove the Cu and, after etching, the naphthalene/gr can be transferred to a target. The naphthalene/gr/target is then heated to 60 °C for 1 hour for naphthalene removal [179]. We adapted this method by delaminating the graphene from its growth substrate using the electrochemical bubbling method [52].

A 5×5 mm^2 piece of CVD grown graphene on Cu was placed on a heating plate with naphthalene crystals (manufactured by Sigma Aldrich [181]) placed on top of it. The sample was then heated to approximately 60°C. At this temperature the naphthalene melts and covers the whole gr/Cu surface under the effect of its own weight. Attempts were made to use a glass plate with teflon tape to press the Naphthalene and obtain a thin layer, but we were unable to detach the teflon tape from the naphthalene post-pressing. We therefore carefully placed the minimal amount of naphthalene on top of the graphene such that upon melting it would just cover the sample without making a visibly thick layer.

For electrochemical delamination, the naphthalene/gr/Cu sample was clamped with a small flat alligator clip and connected to the positive output of a DC power supply, while a 0.5 mm diameter platinum wire was connected to the negative output. Both the sample and the Pt wire were placed in a cold (10 °C) NaOH 1 M solution. When current is

applied (5 V and 5-15 mA), hydrogen bubbles (with size and number varying with the current intensity) form at the interface between Cu and graphene, and in less than 10 minutes, the graphene/naphthalene floats on the surface of the NaOH solution.

In order to evaluate the success of the transfer method, 25 μm thick polycrystalline Cu was chosen as a target, as it would allow direct comparison to our CVD grown samples by Raman spectroscopy. Once delaminated, the naphthalene-supported graphene was fished out with a pair of tweezers and placed (graphene facing down) on top of the target Cu and heated up to 60 ℃ for evaporation of naphthalene.

Multiple experiments were carried out with various currents during electrolysis. The time for delamination varied between 3 and 10 minutes depending on the current. In each case, Raman spectroscopy on the Cu sample post-transfer revealed that none of the characteristic graphene bands (D, G and 2D) were detected. No graphene had been transferred, and Raman spectroscopy performed on the Cu growth substrate further revealed that the graphene was no longer on the Cu surface either, implying it had been delaminated but had not remained attached to the naphthalene. It was concluded that the bond between the naphthalene and the graphene was not sufficiently strong to avoid graphene detachment from the naphthalene support film upon bubbling and that only naphthalene was fished out.

Furthermore, in our experiments we observed that this method wasn't as clean as described, as residue from the naphthalene assisted transfer was visible by eye even after sublimation. This could however be due to the fact that the graphene was separated from the naphthalene during the electrolysis procedure; the absence of graphene between the Cu and naphthalene could enable the naphthalene to stick to the Cu and be difficult to remove completely.

The electrolysis experiment was also carried out without the naphthalene support layer on top. Raman spectroscopy revealed that the graphene was not delaminated from its growth substrate. This could be explained by the fact that the graphene could flexibly detach and reattach to the Cu without the rigidity of the support layer and thus let the bubbles escape without being peeled off.

Taking these factors into account, the Naphthalene supporting layer was replaced by a Polyvinyl alcohol (PVA) layer, which was supposed to leave little residue after transfer [54, 110]. When the PVA-covered graphene on Cu was placed in the NaOH and the electrochemical reaction was initiated, the PVA reacted with the solution and foam was formed, degrading the PVA layer. PVA was not a compatible supporting layer for electrochemical delamination. Instead, the original PVA-supported mechanical exfoliation using a PDMS stamp was adopted as described in the following section.

PMMA could have been used as a support layer in this transfer procedure, but was discarded because of the residues shown to be left behind during transfer procedures [94].

3.4   PVA-assisted transfer in air

The PVA-assisted transfer method, illustrated in figure 3.5, is based on the mechanical exfoliation of graphene from its growth substrate [54]. To support the graphene layer upon delamination, ensuring the whole layer is transferred without breaking and wrinkling, PVA is drop-coated on the gr/Cu (step 1). For delamination, a PDMS stamp is used (steps 2 and 3) and the temperature-dependent adhesion between PDMS and PVA enables the release of PVA post-transfer (steps 4 and 5). The PVA supporting layer is removed post-transfer by immersion in hot water (step 6). This same transfer technique was also demonstrated at large scale using a commercially available PVA foil and a commercial hot-roll office laminator [182].
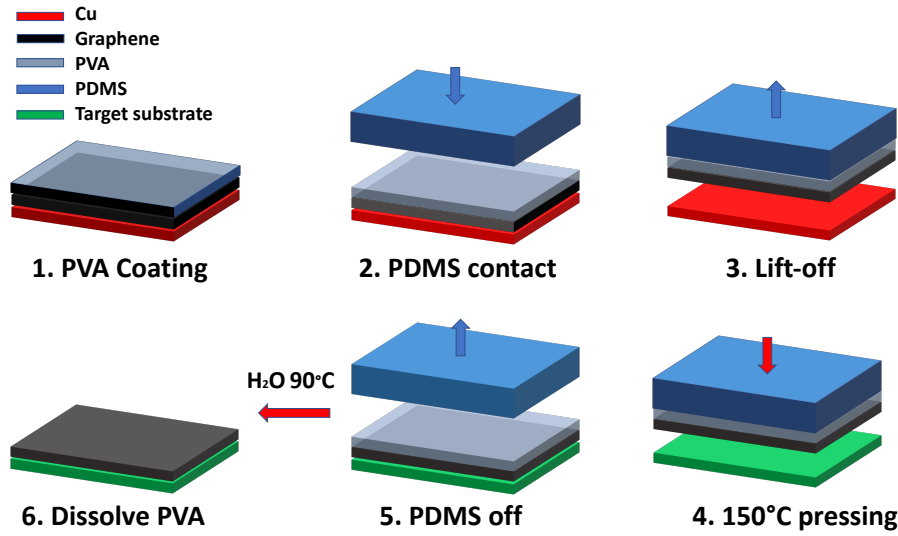
Figure 3.5 – Schematic illustration of the PVA-assisted transfer method. A gr/Cu sample is first coated with PVA. A PDMS stamp is used to delaminate PVA/gr from Cu. PVA/gr is stamped onto the target and PVA is removed by immersion in hot water.

For our experiments, a 0.1 M PVA solution was prepared by mixing PVA powder (Sigma Aldrich [183]) with deionized water in a beaker, and heating the solution to 90 ℃ while stirring with a magnetic stirrer for 4 hours.

The graphene used for these experiments was grown by CVD on a polycrystalline Cu foil according to the procedure described in section 2.6.1. Pieces of 5×5 mm^2 gr/Cu were cut and pretreated by placing them overnight in the PVA solution at 45 ℃. This process forms an ultra-thin layer of PVA on the graphene surface, which is said to improve the bond between PVA and graphene [54]. Comparison between samples with and without pretreatment did not show any evidence of improvement using this pretreatment step and it was therefore discarded from the procedure in our work.

For PVA drop-coating, a 5×5 mm^2 gr/Cu sample is placed on a heating plate and, using a syringe, a single drop of our 0.1 M PVA solution is dropped onto the surface of

the gr/Cu. Upon heating of the sample, the water in the solution evaporates, leaving behind a film of PVA. We found that for optimum coating, the temperature should be slowly increased (approximately 20 ℃ per minute) from room temperature once the drop of PVA is deposited up to a temperature of 70 ℃. If the heating is too quick or the temperature is higher than 70 ℃ when dropping the first PVA drop, bubbles will form, making the PVA film of lower quality and more difficult to transfer and possibly damaging the graphene. After 5 minutes at 70 ℃, when all the water has evaporated, a second drop is deposited at 70 ℃ on the surface while heating for another 5 minutes. The second drop can be deposited at 70 ℃ without damaging the graphene since it is protected by the PVA film from the first drop. The process is done with two drops in order to have a sufficiently thick PVA film that won't break upon delamination.

After the water from the second drop has evaporated, the PVA/gr/Cu sample is attached with double-sided scotch tape onto a flat support. A half-spherical PDMS stamp is then pressed by hand (approximately 30 N force) against the PVA surface of the sample. Quick removal of the stamp after pressing delaminates the PVA/gr stack from the Cu growth substrate and it remains attached to the PDMS stamp. This stack can then be transferred onto a target sample by pressing (approximately 10 N force)against the target with the graphene side facing down. To release the PVA/gr from the PDMS stamp, the target sample is heated to 130 ℃. At this temperature, the heat activates the release of the PVA from the PDMS and the PVA/gr is detached from PDMS and lies on top of the target sample.

Post-transfer, the PVA layer is removed by immersing the PVA/gr/target sample in DI water at 90 ℃, for 3 hours. Immersing the sample longer does not reduce the amount of residual PVA, which is inevitable, as will be shown in the following section. The DI water was changed multiple times during the process to minimize residue.

In the following we describe examples of PVA assisted transfer on different surfaces. First, onto a transparent Si sample, which enables optical analysis of graphene and then to create BLG on Cu, which may serve as a transfer medium. These experiments demonstrate the versatility of this PVA-assisted transfer procedure.

3.4.1 Graphene transfer on Al$_2$O$_3$

As was mentioned in section 1.1, a single layer of graphene absorbs approximately 2.3 % of visible light. By transferring graphene onto a polished Al$_2$O$_3$ crystal sapphire, transmission mode optical microscope images reveal the light absorption and the continuity of the graphene layer can be checked on the μm scale. Further, a second layer can be transferred and the optical images can confirm successful piling of the graphene layers. A 5×5 mm^2 Al$_2$O$_3$ sample was immersed in Isopropanol for 15 minutes and rinsed in DI water for cleaning. For transfer, the Al$_2$O$_3$ target was heated to 130 ℃ and stamped with the

PVA/gr. After PVA removal, Raman spectra were acquired over 10 different sample regions. Graphene covered the whole Al_2O_3 sample and the average Raman spectrum shown in figure 3.6 shows that the graphene is characterized by an average $I(D)/I(G) = 0.1$, indicating high quality with low defect density.
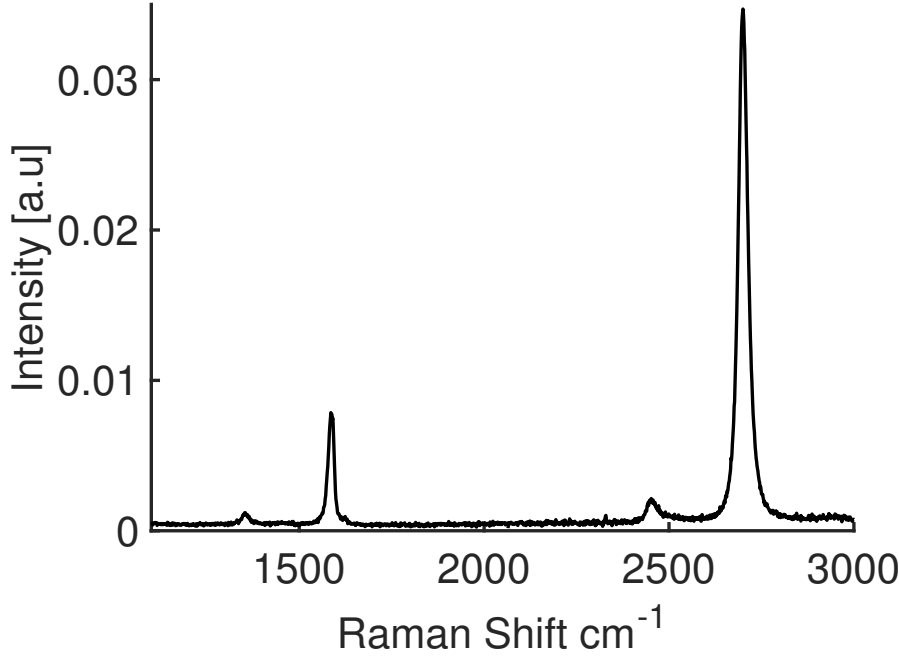
Figure 3.6 – Raman spectrum of graphene transferred onto Al_2O_3 using the PVA-assisted transfer method. 488 nm laser wavelength, 2400 l/mm grating, 25 mW power, exposition time of 50 s, averaged over 10 sample regions.

After characterization, a second layer of graphene was transferred on half of the MLG/Al_2O_3 sample for comparison in optical absorption. The optical microscope image shown in figure 3.7 (a) shows a 800×640 μm^2 region in the center of the sample, where both MLG and BLG can be seen on Al_2O_3. Round surface contaminations with a diameter of a few micrometers can be seen. They are supposed to be PVA residue, or surface contaminations stuck under the graphene layer. In order to assess the change in graphene thickness across the sample, we calculated the relative transmission by dividing the pixel intensities by those of areas with no graphene on top (100 % relative transmission). The relative transmissions for points between the two dashed red lines were calculated and are plotted as a function of the pixel number in figure 3.7 (b). Their mean values along the MLG and BLG parts are represented as blue lines at respectively 97.3 % and 93.3 %. The absorption on the MLG part is, at 2.7 %, slightly higher in average than the literature value of 2.3 %, which may be explained by residual PVA from the transfer procedure. It has been shown that the absorption increases linearly with graphene layers [184], thus according to our MLG measurement, two layers should absorb 5.4 %, according to the literature value, 4.6 %. On the BLG part of our sample the average absorption was 6.7 %, which again could be caused by PVA residue on the surface. The variations in

absorption with position also indicate that the residue is not evenly distributed, with regions absorbing more than others. This result however confirmed that we were able to transfer a second layer of graphene on top of the first one.
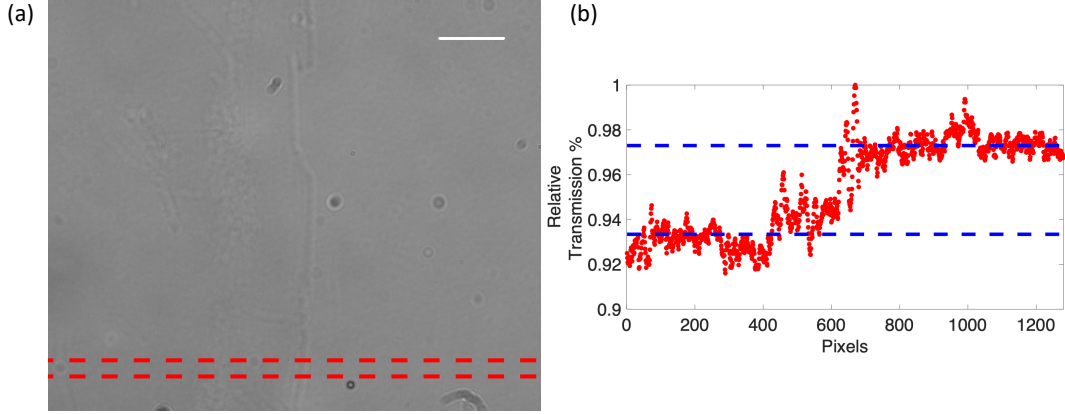
Figure 3.7 – (a) 800×640 μm^2 optical transmission microscope image of BLG (left half) and MLG (right half) on Al$_2$O$_3$. The white scale bar represents 100 μm and the red dashed lines show where the transmissions shown in (b) are calculated. (b) Relative transmission as a function of horizontal position. Average relative transmission of 93.3 % and 97.3 % for BLG and MLG respectively.

3.4.2 Mechanically stacked BLG/Cu

Bilayer graphene on Cu can be produced by mechanical stacking using gr/Cu grown by CVD as the target of the PVA-assisted transfer. Since in this case only a single transfer is necessary to obtain BLG/Cu, this sample should be less contaminated than the BLG/Si sample and could be used as support for transfer in UHV. For direct comparison between monolayer and bilayer graphene on Cu by Raman spectroscopy and by XAS, samples consisting of MLG/Cu on one half and BLG/Cu on the other were made as is shown in the procedure depicted in figure 3.8. Two pieces of CVD grown graphene on Cu are cut (one 5×5 mm^2 and one 10×5 mm^2). The smaller piece is covered with PVA (step (a)) and transferred onto half of the larger piece by the PVA-assisted transfer procedure (step (b)). After PVA removal, the resulting sample consists of MLG/Cu on one half and BLG/Cu on the other half, referred to as MLG after transfer (AT) and BLG AT (step (c)) respectively. The MLG AT is distinguished from the MLG by CVD because it has been immersed in water for the PVA removal, which may alter its spectrum. We now turn to the characterization of these samples by Raman spectroscopy and XAS.

Raman analysis

Prior to the PVA-assisted transfer, the Raman spectrum of the CVD-grown graphene on Cu (see section 2.6.1) was acquired. After transfer, both MLG/Cu and BLG/Cu areas were measured. These correspond to the MLG AT and BLG AT in figure 3.8. The
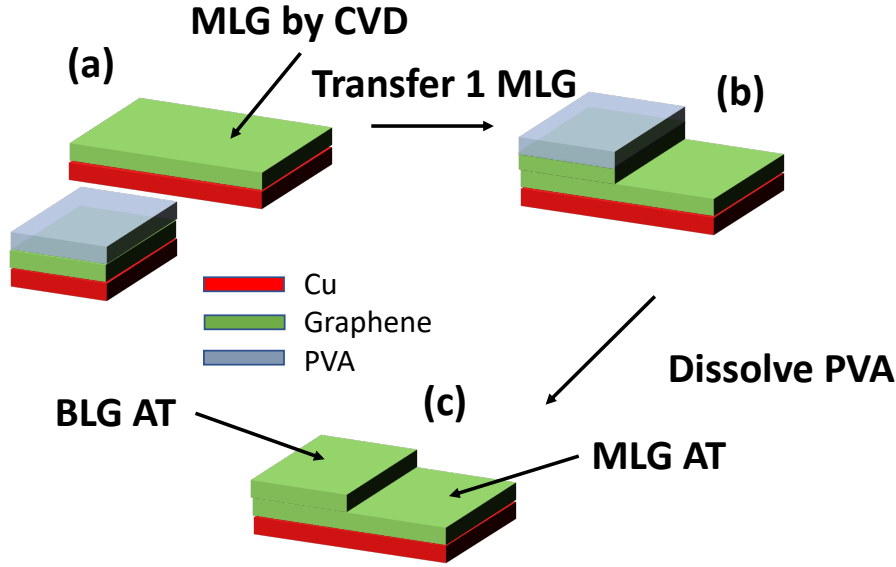
Figure 3.8 – Schematic illustration of the BLG/Cu stacking procedure. (a) One sample of gr/Cu is coated in PVA. (b) Graphene is transferred by the PVA-assisted method onto half of a MLG/Cu sample obtained by CVD. (c) After transfer (AT), a sample covered half with MLG and half with BLG is obtained.

Table 3.3 – Raman characterization of MLG and BLG on Cu obtained by the PVA-assisted transfer. The values are the averages on 5 measurement spots and are given with a confidence interval evaluated as the standard deviation of the dispersion of the values measured in different spots. The FWHM and peak positions are given in cm^{-1}.

Sample	2D FWHM	2D position	G FWHM	G position	$I(G)/I(2D)$	$I(D)/I(G)$
MLG CVD	34±3	2714±4	18±2	1588 ±2	0.35±0.07	0.1±0.03
MLG AT	34±3	2688±3	22±4	1583±1	0.33±0.08	0.11±0.04
BLG AT	40±4	2703±3	19±3	1585±2	1±0.7	0.08±0.06

MLG AT and BLG AT sample was annealed to 200 ℃ before measurements. In figure 3.9, the three spectra, each averaged over 5 sample regions, are plotted. The average values of FWHM, peak positions, $I(G)/I(2D)$ and $I(D)/I(G)$ ratios for these spectra are given in Table 3.3 with a confidence interval evaluated as the standard deviation of the dispersion of the values measured in different spots. The measurement error for a given spot is much smaller and is therefore neglected. The sharp peak at around 2330 cm^{-1} is a measurement artefact and the one at 1300 cm^{-1} is a background subtraction artefact.

Comparison between the 2D band of the CVD grown sample and the MLG AT shows that the 2D band is redshifted (by 26 cm^{-1}) after the transfer procedure, which indicates possible doping of the graphene [185], that may be due to PVA residue adsorbed on the surface that was not completely removed by immersion in water. For direct comparison with the BLG AT, the MLG AT is used instead of the CVD grown MLG/Cu such that the effects of these residues are taken into account. After transfer of the top graphene
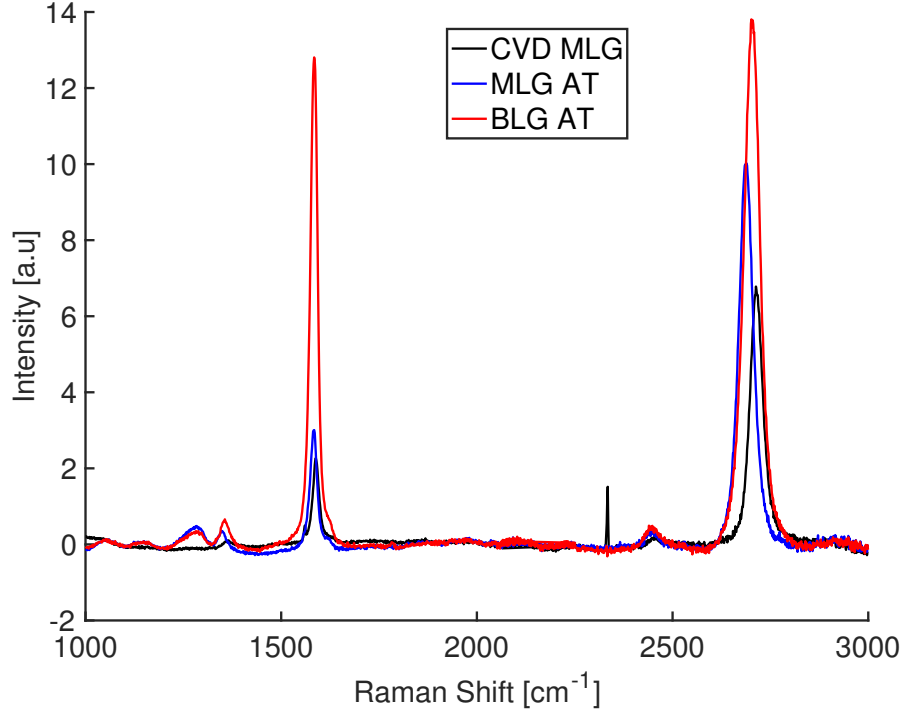
Figure 3.9 – Raman spectra of CVD grown MLG/Cu (in black), MLG AT(in blue) and mechanically stacked BLG AT (in red) on Cu. Sample annealed to 200 ℃. 488 nm laser wavelength, 2400 l/mm grating, 25 mW power, exposition time of 50 s, averaged over 5 sample regions.

layer, the FWHM of the 2D band increases from 34 cm^{-1} to 40 cm^{-1} and the $I(G)/I(2D)$ ratio increases from 0.33 to 1.0. These values are in agreement with typical values for monolayer and bilayer graphene samples (see Table 1 in [166]). Further, the 2D peak position for the MLG AT spectrum is 2688 cm^{-1} and for the BLG AT spectrum, the peak is at 2703 cm^{-1}, a blueshift that is typically attributed to the change in Fermi velocity in bilayer graphene [186]. The very large spatial variations of the $I(G)/I(2D)$ and $I(D)/I(G)$ ratios, expressed in the confidence intervals, are believed to be due to specific local twist angles between the two graphene layers that may induce very large G band intensities for some angles (a 12° twist angle has been shown to increase the G band intensity by a factor 4 with respect to other twist angles) [34]. These may appear due to the random alignment of the graphene domains during growth on polycrystalline Cu and the subsequent transfer of another multi-domain graphene layer on top. Nevertheless, these results suggest that we successfully stacked two high-quality layers of graphene on the polycrystalline Cu sheet.

XAS analysis

To further characterize the success and the cleanliness of the PVA-assisted transfer method, XAS measurements were carried out at the K-edge of C with linearly polarized

(0° and 90° polarizations) x-rays on both the MLG and BLG regions of the sample.

In figure 3.10 (a), the XANES spectrum of pristine MLG after transfer is compared to the same sample annealed to 420 ℃ in UHV for 30 minutes. The difference in intensity and peak shape of the XANES suggests the presence of an amorphous C contamination on the MLG after transfer. Indeed, the XAS intensity is strongly reduced on the annealed sample, leaving only the π and σ electron orbital absorption peaks. Annealing to lower temperatures was not sufficient to reduce the contamination and in subsequent experiments, the transferred samples were annealed to 420 ℃. This C contamination is supposed to be due to PVA, which contains carbon atoms that contribute to the XAS background signal depending on the bonds they form on the graphene surface.

In figure 3.10 (b), we show the XANES spectra of both MLG and BLG regions after annealing to 420 ℃. To compare the amount of graphene on both MLG and BLG parts, the π electron orbital XAS absorption peak intensities are measured in figure 3.10 (b). However, the masking of the signal of the first graphene layer by the second layer must be taken into account for proper comparison. Indeed, during the background subtraction, in order to take into account small variations in the x-ray beam intensity, the spectrum of the clean Cu and the one with graphene are normalized to unit in the pre K-edge of the C region. This normalization masks the difference in absorption of MLG and BLG. By checking the absolute absorption intensity in the pre K-edge of the C region, we found that each graphene layer reduces the substrate signal by about 25 %. Taking this factor into account, the spectrum for BLG has to be multiplied by a factor 1.25. After multiplication, the π orbital peak intensities are 0.6 and 1.2 for MLG and BLG respectively, confirming the presence of BLG on half the sample. Indeed, the peak intensity is a measure of the number of contributing π electron orbitals, which should theoretically be double in the case of BLG compared to MLG.

In summary, this transfer method is successful at making BLG samples, but the samples obtained by this transfer method need to be annealed to 420 ℃ in order to remove the C contamination from PVA. We were previously unable to detect this carbon contamination by Raman spectroscopy, which could be due to the fact that PVA Raman bands disappear upon thermal destruction while increasing background intensity [187] and could contribute very little to the Raman spectrum of the transferred graphene. The bilayer prepared this way is a potential candidate for transfer of graphene to a target surface since it no longer requires the removal of a support layer as the remaining Cu/gr would remain attached to the stamp. Furthermore, the thin polycrystalline Cu sheet on which the BLG is adsorbed is quite flexible, making it easily adaptable to the morphology of the target surface.
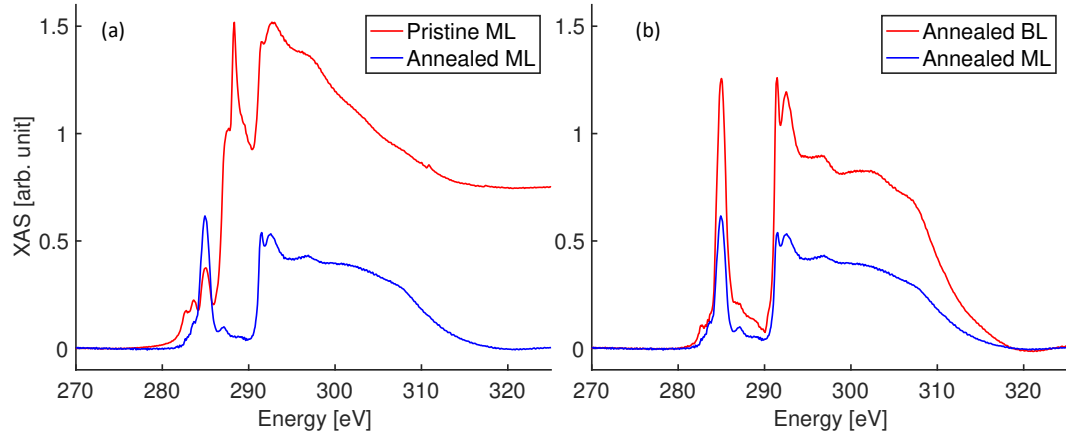
Figure 3.10 – Carbon K-Edge XANES of (a) pristine and annealed (420 ℃) MLG AT and (b) annealed (420 ℃) MLG AT and BLG AT regions. The 0° and 90° polarizations have been summed. Graphene π electron orbital absorption peak at 285 eV and σ electron orbital peak at 292 eV. The spectra were acquired at 60° incidence at room temperature at the X-Treme beamline. Cu background was acquired on a clean Cu(100) single crystal and subtracted.

3.4.3 BLG/Cu for transfer

Using the PVA-assisted method, mechanically stacked BLG/Cu samples were created to be used as a transfer medium. After PVA removal, the Cu/BLG was annealed to 420 ℃. For transfer in air, a 5×5 mm^2, 25 μm thick polycrystalline Cu sheet was immersed in acetic acid (CH$_3$COOH) for decapping and subsequently rinsed in DI water. Prior to transfer attempts, the clean Cu was checked by Raman spectroscopy to verify that the graphene-related D and G bands were not present. Using the wafer-bonding approach, the BLG/Cu was placed with the BLG facing down on the clean Cu and a weight was placed on the Cu/BLG/Cu stack. Pressing force and temperature were varied, but Raman spectroscopy performed on each target Cu post-transfer in air revealed the absence of transferred graphene in each of the attempts. This could either be due to a stronger bond between the two graphene layers than the graphene-Cu bond or to a contaminated interface which would not allow the top graphene layer to adhere to the target Cu.

To ensure the cleanliness of the target during transfer, the same experiment was repeated in UHV conditions using a clean Ir(111) target crystal. An Ir(111) target was chosen in hope of using STM imaging of the typical moiré pattern of graphene on Ir(111) to assess the success of transfer in addition to AES. The BLG/Cu was glued with silicone glue on top of a PDMS stamp adapted for our UHV setup (see section 2.5.1 and fig. 2.13). This setup preserves flexibility and adaptability of the BLG/Cu stamp for pressing onto the target.

Prior to transfer, the Ir(111) crystal was prepared according to the procedure described in section 2.5.2 and cleanliness was checked by means of AES. The BLG/Cu/PDMS

stamp was placed graphene-face down on the Ir(111) target at room temperature for transfer and pressed with 30 N using the wobble stick (see fig. 2.14). The force used for pressing is limited by the wobble-stick on which the stamp is mounted. The target and the Cu/BLG stamp were pressed together for approximately 30 seconds before lifting the stamp. Transfers were performed with the target at a temperature between RT and 80 ℃. After transfer at RT, no AES peaks other than Iridium were detected, suggesting no graphene was transferred. On the contrary, after transfer at 80 ℃, a carbon peak was detected on the Ir(111) surface, but oxygen was detected simultaneously on the surface as is shown in figure 3.11. During the transfer attempt, the pressure climbed to $1 \cdot 10^{-8}$ mbar, due to degassing of PVA or PDMS in contact with the hot target. Annealing to 430 ℃ leads to partial desorption of carbon and oxygen while maintaining the C and O ratio roughly equal as is shown in table 3.4. This suggests the presence of a large majority of adsorbents containing both C and O, which suggests PVA (C_2H_4O) or PDMS (C_2H_6OSi) lies on the surface. This hypothesis is supported by the fact that we were unable to image the surface with STM, even after annealing to 430 ℃, as the STM tip was too unstable.
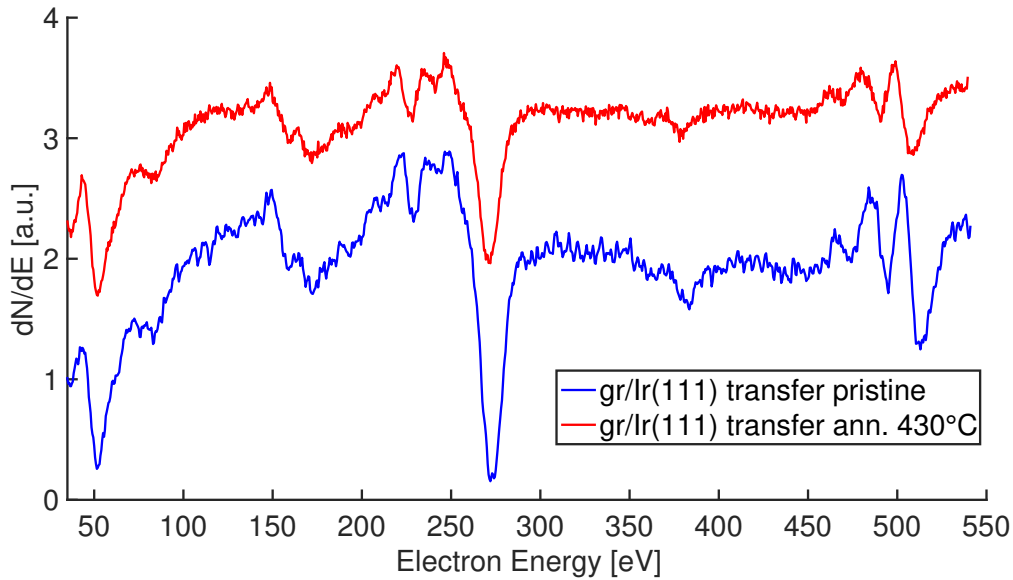
Figure 3.11 – Auger electron spectra after UHV transfer from BLG/Cu onto Ir(111). In blue after transfer at 80 ℃ and in red after subsequent annealing to 430 ℃. The intensity is normalized to the Ir peak height (at 54 eV). Primary electron energy 3 kV, 0.3 eV step in analyzer energy. Intensity ratios in table 3.4.

In conclusion, although it is possible that some graphene had been transferred when the target Ir(111) sample was at 80 ℃, PVA or PDMS account for a large part of the transferred material due to degassing and could not be removed, making this approach unsuited for our goal. The lack of success in transferring the top graphene layer at room temperature suggests that the adhesion between graphene layers is stronger than the adhesion at the gr/Ir interface, even though the target Ir(111) was clean. This could be due to interfacial contamination between the two layers due to the exposure to air or

Table 3.4 – Auger intensity ratios measured in figure 3.11 and equivalent amount of C in ML (calculated with respect to a reference CVD grown sample, see section 2.3) after transfer from BLG/Cu onto Ir(111). The ratio between carbon peak intensity and oxygen peak intensity $I_\mathrm{C}/I_\mathrm{O}$ is given.

Sample	$I_\mathrm{C}/I_\mathrm{Ir}$	Equivalent amount of C [ML]	$I_\mathrm{C}/I_\mathrm{O}$
Pristine	2.7 ± 0.1	1.0 ± 0.04	1.9 ± 0.1
Annealed 430 ℃	1.7 ± 0.1	0.6 ± 0.04	2.2 ± 0.1

to the PVA residue on top of the BLG, which should however act as a glue. Interface contamination can be reduced by carrying out the delamination process of graphene from Cu for bilayer stacking in UHV, but still requires the sample to be exposed to air and water.

3.5 Adaptation of the PVA-assisted transfer to UHV

Although the PVA-assisted transfer cannot be carried out completely in UHV, due to the necessity to remove PVA in water, the crucial steps of graphene delamination and transfer to the target can be at least partially adapted for UHV. By doing so, the interface between the graphene and the target surface can be kept clean, free from air contamination. In order to carry out the transfer in UHV, a PDMS stamp was adapted for our experimental setup (as described in section 2.5.3). 5×5 mm^2 pieces of CVD grown gr/Cu were cut, and PVA was drop-coated on each piece, as described in section 3.4. The PVA/gr/Cu was then stuck to an aluminium plate adapted for our sample stages with double-sided tape (see fig. 3.12 left).

The first step involves the delamination of the graphene from its Cu growth substrate in the UHV chamber. The PDMS stamp (see fig. 3.12 right) is pressed against the PVA/gr/Cu with the wobble stick (as shown in figure 2.14) and lifted in a quick motion, delaminating the PVA/gr from the Cu growth substrate.

The target sample is then placed on the L-shaped manipulator and heated to 130 ℃. For transfer, the PDMS/PVA/gr is placed on top of the target sample and pressed for 10 seconds (with 10 N force) before gently lifting the PDMS stamp.

Post-transfer, the target sample, covered with graphene and PVA, must be taken out of the UHV chamber and placed in water for PVA removal. After PVA removal in water, the sample is reinserted in the UHV chamber. Following our findings in the XAS analysis performed on PVA-assisted transfer of graphene, the sample was subsequently annealed to at least 400 ℃. This adapted PVA transfer technique was used to create mechanically stacked bilayers of graphene on Ir(111) as is described in the following section.
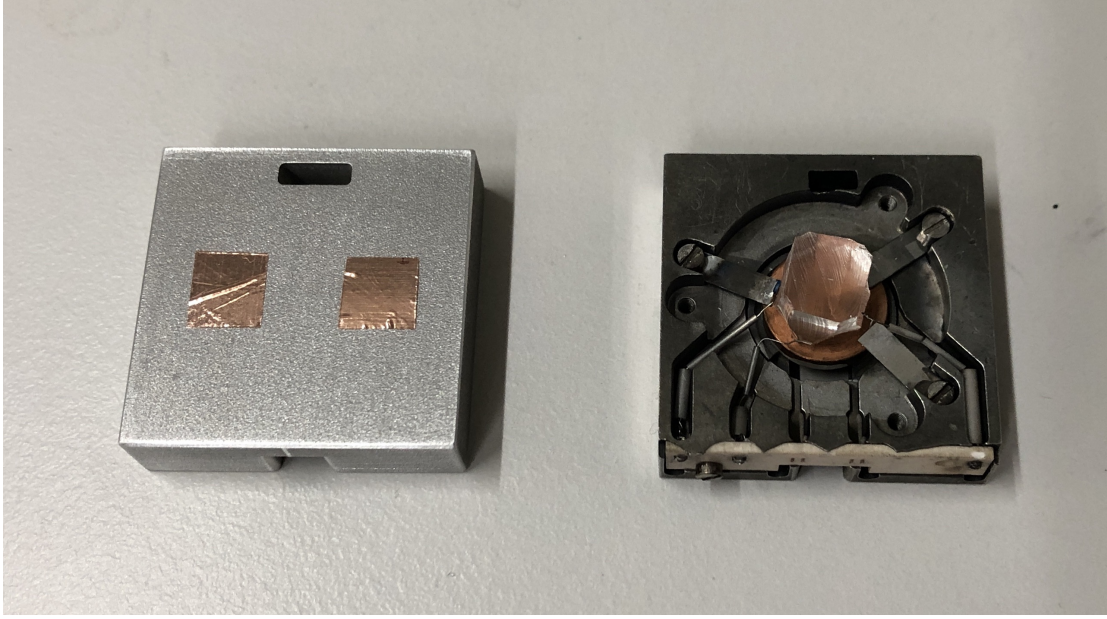
Figure 3.12 – Equipment for PVA-assisted transfer in UHV. On the left the aluminium plate on which two PVA-covered graphene on Cu samples are fixed with double-sided tape. On the right, the PDMS stamp used to delaminate the PVA/gr from the Cu.

3.5.1 BLG/Ir(111) for transfer in UHV

The unsuccessful transfers from BLG/Cu to an Ir(111) target motivated making a supported BLG with a clean interface between the two graphene layers. Since graphene can be obtained simply by CVD on Ir(111) (self-limited process yielding a single layer of graphene), gr/ Ir(111) was chosen as the support for the BLG. The disadvantage of using Ir(111) lies in the rigidity of the sample, which cannot perfectly adapt over the target surface upon transfer.

Graphene was grown by CVD on Ir(111) in our UHV chamber as described in section 2.6.2 and the I_C/I_{Ir} ratio of gr/Ir(111) was checked with Auger spectroscopy to confirm ML growth (see bottom spectrum in fig. 3.13). The PVA-assisted transfer technique adapted for UHV described above was then carried out using the CVD grown gr/Ir(111) sample as a target for transfer. The process yields a BLG/Ir(111) sample after PVA removal and annealing to 430 ℃ to remove the majority of PVA residue (see section 3.4.2). The two surfaces of graphene that are in contact with each other have not been exposed to air and should therefore theoretically be bound by vdW forces, supposing that no interlayer diffusion takes place when the sample is exposed to air and the PVA is removed in the hot water. Figure 3.13 shows the Auger spectra for gr/Ir(111) obtained by CVD and BLG/Ir(111) after PVA-assisted transfer and annealing to 430 ℃. The intensity ratio for I_C/I_{Ir} for the CVD-grown gr/Ir(111) is 2.6. For BLG/Ir(111), the ratio is 12. In section 2.3, comparison between a theoretical calculation of the Auger intensity

ratios for BLG/Ir(111) and MLG/Ir(111) shows that the signal intensity ratio is not simply multiplied by a factor of 2, but that the multiplication factor should be closer to 3. With the single layer on Iridium at 2.6, an intensity ratio of 8 was expected for BLG/Ir(111). Our ratio value of 12 is 50 % larger than the theoretical value, suggesting that we still had PVA residue on the surface. However, this sample was used as the graphene carrier for transfer using the wafer-bonding approach in UHV.
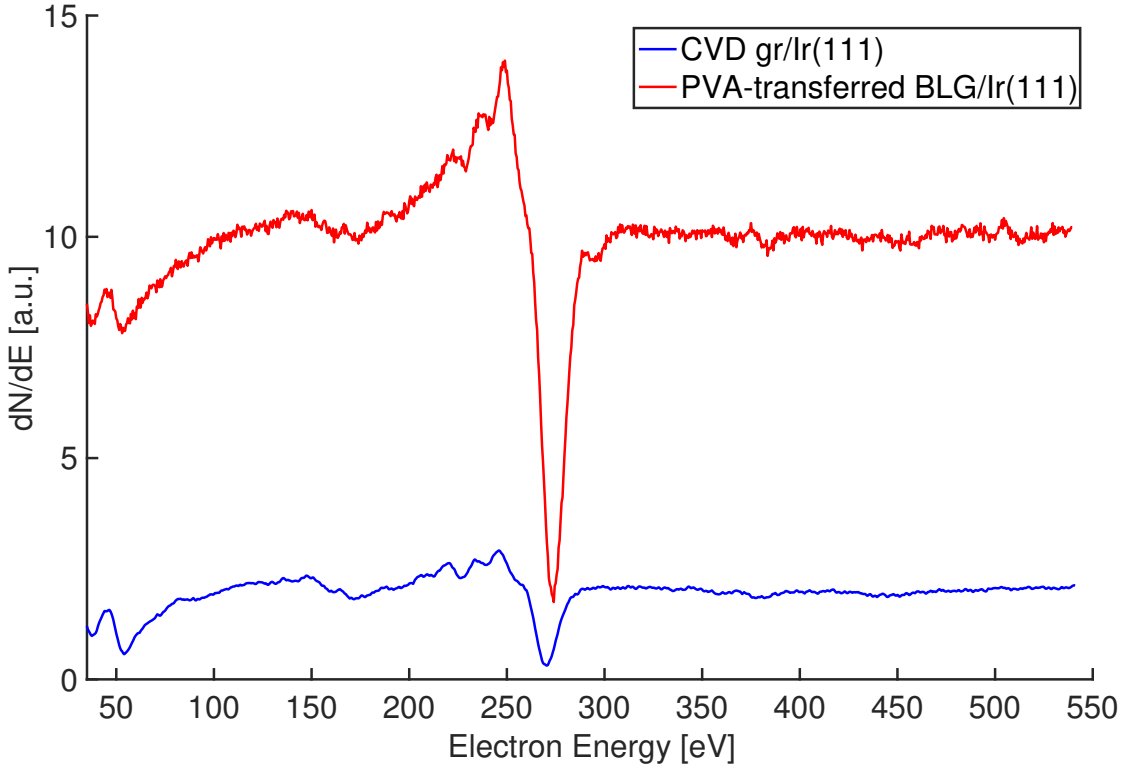
Figure 3.13 – Auger spectrum of PVA-assisted BLG/Ir(111). The first layer of graphene was grown by CVD, the second layer was transferred by the PVA-assisted method. The intensities are normalized to the Ir peak height (at 54 eV) and offset for clarity. Primary electron energy 3 kV, 0.3 eV step in analyzer energy.

In order to transfer the top layer of graphene from the BLG/Ir(111) to the target, the BLG/Ir(111) was flipped by 180° in the load-lock such that the BLG was facing downwards. The BLG/Ir(111) was pressed for 10 seconds against a second Ir(111) crystal used as the target, prepared as described in section 2.5.2. Following transfer attempts, AES was performed on the surface to check for the presence of carbon on the target Ir(111) sample. The procedure was repeated several times without success. This could either be due to a weaker bonding force between graphene and iridium with respect to the two layers of graphene (perhaps due to the use of PVA), or to imperfect alignment of the two crystal surfaces in contact. Indeed, both samples being rigidly mounted, with no PDMS stamp to allow the two surfaces to adapt to each other, an atomic-level alignment of the two surfaces is practically impossible to perform.

To check the first hypothesis, we tried the same procedure using Ni(111) as target since due to the hybridization of the π-orbitals of graphene with the nickel d-electrons [188] stronger adhesion than the graphene-iridium bond is expected. The Ni(111) target sample was again prepared as described in section 2.5.2 and the same transfer procedure using Ir(111)/BLG was performed, unsuccessfully, suggesting that a better alignment of the surfaces was necessary. Further, these results again seem to suggest that PVA enables a stronger bond between two graphene layers post-transfer. To test this hypothesis, a piece of scotch-tape was pressed on the Ir(111)/BLG, taking care to have a uniform adhesion to the surface before being lifted. Raman spectroscopy performed on the piece of tape post-delamination revealed that no graphene was delaminated, confirming that a strong bond had formed between the two graphene layers, making it impossible to transfer using this technique.

To further understand how PVA contaminates the transferred graphene layer, the transfer procedure was applied onto an Ir(111) target. Our results are presented in the following section.

3.6 PVA-assisted transfer from CVD graphene to Ir(111) in UHV

Transfer of a graphene layer on clean Ir(111) can be compared to a CVD-grown graphene on Ir(111) to assess the different graphene quality obtained with the two methods. In theory, a clean transfer should allow one to see the moiré that is formed when graphene is adsorbed on Ir(111) (see section 2.6.2).

Our UHV-adapted transfer method was applied to a clean Ir(111) sample according to the procedure described in section 3.5. Post-transfer, PVA was removed by immersion in hot water and the sample was reinserted in UHV via the load-lock. The gr/Ir(111) was first annealed to 100 ℃ to desorb water residue and AES was used to assess the amount of transferred graphene and carbon transfer residue by comparison to the reference AES spectrum of CVD-grown graphene on Ir(111), which was characterized by $I_C/I_{Ir} = 2.7$ during these experiments (see section 2.3)). A successful and clean transfer should be characterized by the same ratio since this value should be independent of whether the graphene was grown on the iridium by CVD or if it was transferred to it. On the contrary, contamination of the graphene layer or the gr-iridium interface would change the ratio because of the difference in electron absorption at different energies (54 eV vs. 270 eV).

Multiple transfers were performed following this procedure and in each case AES showed a very high carbon content (in some cases equivalent in quantity to more than 2 monolayers of graphene). This large amount of carbon was attributed to residues of PVA which were not removed by immersion in the hot water, as was also observed for our transfers in air.

In Table 3.5, the evolution of the I_C/I_{Ir} ratio with respect to annealing temperature is given for the sample on which the STM image shown in figure 3.14 was acquired. The equivalent amount of C (in ML) was estimated by assuming a linear dependence between I_C/I_{Ir} and the coverage (considering that $I_C/I_{Ir} = 2.7$ for 1 ML and $I_C/I_{Ir} = 8.1$ for 2 ML, according to the discussion in section 2.3).

Table 3.5 – Evolution of the Auger I_C/I_{Ir} ratio as a function of the annealing temperature for gr/Ir(111) obtained by PVA-assisted transfer. Estimated equivalent amount of C calculated with respect to a reference CVD grown gr/Ir(111). The error bars on the ratios and equivalent amounts of C are 5 %.

Annealing T [℃]	100	450	550	700	900	1100
Annealing time [min]	10	30	15	15	5	3
I_C/I_{Ir}	8.0	4.4	4	4.1	3.9	3.6
Estimated equivalent amount of C [ML]	1.98	1.32	1.24	1.26	1.22	1.17

In general, after being inserted in UHV, the samples are annealed to at least 100 ℃ to remove water contamination. Increasing the annealing temperature to 450 ℃ significantly

reduces the carbon quantity, which indicates a large quantity of residual amorphous carbon is desorbed from the surface. Annealing to higher temperatures further decreases the I_C/I_{Ir} ratio to a value of 3.6 (equivalent to 1.17 ML) at 1100 ℃. The annealing time was limited by the increase in pressure due to degassing; higher temperatures could be maintained for shorter times. The Auger spectrum for the sample annealed at 1100 ℃ is shown in figure 3.14 (a). The ratio in this figure is 3.3, equivalent to 1.11 ML, but the value of 3.6 (or 1.17 ML) was the average over 3 different measurement areas on the sample. The SNR of this spectrum is lower than the one shown in figure 2.8 (channeltron voltage 1200 V). This is due to the channeltron voltage that was 1000 V for this spectrum and was later increased to improve the SNR. On the same annealed sample, STM shows multiple domains with multiple moiré orientations and periodicities and islands pinned to the domain boundaries (see fig. 3.14 (b)). The standard deviation of the dispersion of the different domain orientations is 21°. It is not certain whether the multiple domains and periodicities are due to the growth method of the graphene, which is grown on polycrystalline copper, inducing small domains of graphene [15], or if they appear during transfer, due to the stress put on the graphene layer, which may lead to deformations and thus modify the graphene as described in section 1.1.4. The large white islands seen on the STM image shown in figure 3.14 (b) are interpreted as carbon residue from the PVA support layer (in accordance with the higher I_C/I_{Ir} Auger ratio of the sample compared to CVD grown gr/Ir(111)). These residues get stuck and accumulate at the boundaries of graphene domains probably due to residue reorganisation during annealing.

Based on the chemical composition of PVA (C_2H_4O) and the fact that no oxygen peak was detected (no O_2 peak at 520 eV in 3.14 (a)), we suppose that the residue is carbon left over from the annealed PVA, which is supported by our XAS experiments (see 3.4.2), which also showed that carbon residue was adsorbed on the surface. The residue coverage measured on this image is 14 % (projected area on the surface) and the average apparent height of the residue islands is 15 Å.

To increase the size of the transferred graphene grains, we attempted to transfer a layer of graphene grown on Iridium directly in the UHV chamber. The graphene layer was grown on Ir(111) as described in section 2.6.2 (exposure of Ir(111) heated to 1400 K to 100 Langmuir of C_2H_4). The sample was then taken out of UHV and covered with PVA before being reintroduced in the UHV chamber for delamination. We were unable to detach the graphene/PVA from the Iridium sample after multiple attempts, suggesting the adhesion force between graphene and Ir(111) was larger than the PVA/PDMS bonding strength.

In conclusion, although we are able to transfer graphene to Ir(111) and see the moiré pattern, the sample must be brought to air and then annealed to high temperatures upon reintroduction in UHV, and is still covered with PVA residue. This makes it unsuited for capping or building 3D heterostructures based on graphene without contamination from air and PVA. Note that we speak here about amounts of contaminants in the 10 % of a monolayer range, which is relatively clean compared to conventional transfer methods.

(a)

(b)
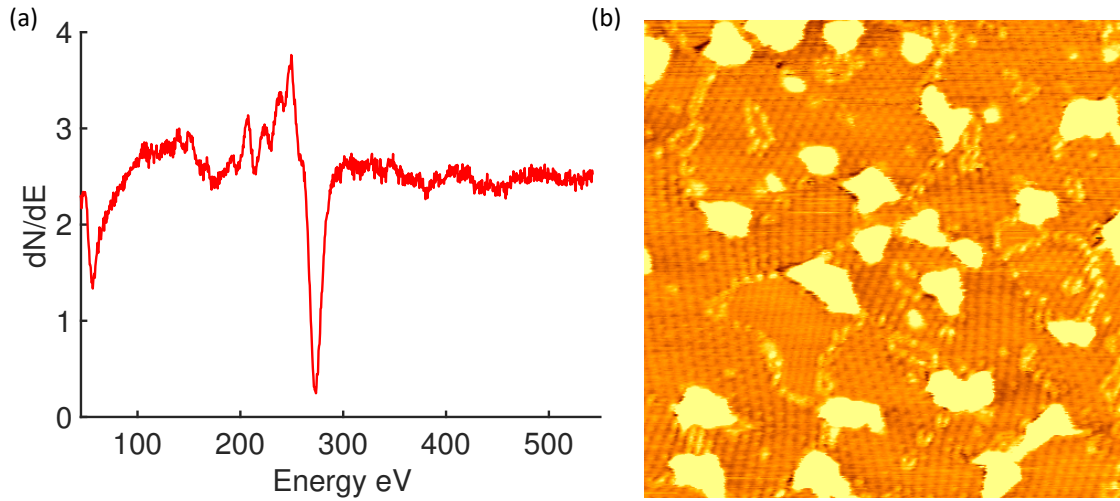
Figure 3.14 – Graphene transferred on Ir(111) and annealed to 1100 ℃ (a) AES spectrum, $I_C/I_{Ir} = 3.3$, equivalent to 1.11 ML of C (b) 1000 Å× 1000 Å STM image ($V_t = -1.4$ V, $I_t = 300$ pA, T = 300 K)

Nevertheless, a PVA-free procedure was necessary for a clean transfer that did not require annealing to high temperature for residue removal nor immersion in water. The most promising transfer media is a multilayer of graphene from which a single layer can be detached. In what follows we describe our results using multilayer graphene on SiC as the transfer media.

3.7 Graphene on SiC for transfer

From private communications in August 2019 with Professor Satoru Tanaka from the university of Kyushu, Japan, we learned that in his group they were able to transfer graphene from one gr/SiC sample to another gr/SiC sample and obtain partial bilayer on one side by pressing them against each other in high vacuum (HV). Their experimental setup consisted of a press placed in a vacuum chamber, which enabled relative positioning of the two surfaces in perfect parallel alignment unlike our experiments performed with the wobble stick. The result of their transfer process is a partial transfer of a layer of graphene. They, however, specified that the side on which the graphene was transferred was random. These results nevertheless motivated the use of graphene on SiC as our graphene source for transfer.

Commercial $7 \times 7 \text{mm}^2$ monolayer graphene on the Si-face of 4H-SiC(0001) was purchased from Graphensic AB [189]. These samples are prepared by Si sublimation from a SiC substrate at high temperature and are described to have a homogenous graphene layer on top of a carbon buffer layer on the Si surface [190]. The bond between the carbon buffer layer and the Si should be stronger than the graphene-buffer layer bond; therefore, the buffer layer should not be transferred with the graphene.

For more adaptability to the underlying target surface, the SiC sample was mounted on top of a PDMS stamp as described in section 2.5.3. The gr/C/SiC was glued onto the PDMS stamp with silicone adhesive (DOWSIL 744 RTV Adhesive Sealant [162]) and left to dry overnight before being inserted into the UHV chamber.

The first transfer experiments were carried out using Ir(111) as target. Using our wobble stick, the gr/C/SiC/PDMS was pressed against the clean crystal (graphene side facing downwards) at room temperature for times varying between 10 seconds and 1 minute with a pressing force of 30 N. None of the AES spectra revealed the presence of C on the Ir(111) surface. This was mainly attributed to the combination of weak interaction between Iridium and graphene, which could be attributed to surface contamination of the SiC sample that had been in air prior to our transfer attempt and had not been annealed in UHV, or to the difficulty of aligning both rigid surfaces for pressing using the wobble stick. Indeed, in contrast with Prof. Tanaka's experiment, our system did not present the same perfectly parallel pressing system. Transfer was attempted with the target sample at 100 ℃ and carbon was present in the Auger spectrum (equivalent to 0.2 ML of C), but similarly to our results using BLG/Cu on the PDMS stamp, an oxygen peak was also visible at 520 eV, again suggesting that carbon and oxygen had been adsorbed on the surface due to degassing of the PDMS stamp during pressing.

To increase the probability of transfer by increasing graphene-target adhesion, a clean Ni(111) crystal was used as a target. The previously described transfer procedure was

Table 3.6 – Effect of annealing gr/SiC samples to 250 ℃ on the Carbon Auger peak intensity.

Sample	Peak-to-peak pristine [a.u.]	Peak-to-peak annealed [a.u.]	variation
SiC 1	0.148	0.134	-10 %
SiC 2	0.169	0.156	- 8 %

repeated and graphene transfer assessed with AES. Again, only the transfer at 100 ℃ was characterized by a carbon peak in the Auger spectrum, along with oxygen.

In an attempt to reduce surface contamination of the graphene on SiC, the gr/C/SiC sample was attached to a Cu sample-holder adapter using silver paste (see fig. 2.13). It was then inserted in the UHV chamber and annealed to 250 ℃ for cleaning. The SiC/gr was then taken out of the vacuum chamber and removed from the Cu before being glued onto the PDMS stamp and reinserted in the UHV chamber. The AES spectrum before and after annealing of two separate SiC samples were acquired at a primary electron energy of 3 kV and a 2.34 A filament current. In both samples, a reduction in carbon content was observed upon annealing. The carbon peak intensities are listed in table 3.6. Annealing decreases the C signal by roughly 10 %. This decrease is attributed to carbon-containing surface pollution that was removed by annealing.

Although this procedure seems to reduce surface contamination (lower carbon content on the surface), we were still unable to transfer the graphene from the SiC after carrying out the same transfer procedure. This could be due to the necessity to re-expose the SiC/gr to air after annealing in order to glue it to the PDMS stamp. Following these negative results, the same scotch-tape procedure used on the TEM grid was carried out. We were unable to delaminate a single layer of graphene from the commercial SiC/gr sample, which demonstrated that this sample was unsuited for our transfer approach.

Following the "34e édition des Journées Surfaces et Interfaces" conference, organized by the institute of nanoscience of Paris, we attempted the transfer of graphene from SiC/gr samples prepared by Yann Girard of the University of Paris Diderot Lab. MPQ (CNRS - UMR 7162). A 5 mm× 5 mm area of multilayer graphene was prepared on the C face of n-doped SiC(000-1) by annealing to 1300 ℃ for 5-10 minutes [191]. Two types of samples were prepared for us, one batch with 1-3 layers of graphene and the other batch with 3-6 layers.

The results obtained using these samples were identical to the previously described commercial gr/C/SiC sample and the same scotch-tape test confirmed that the graphene was strongly bound to the underlying graphene layers, which we were unable to explain, as the interaction between graphene layers should be of the weak vdW type.

3.8   Conclusion

From the results presented in this chapter, we conclude that the use of PVA for the mechanical stacking of two graphene layers was incompatible with our goal to transfer a single graphene layer. Indeed, we were not able to detach the top graphene layer from its support. The PVA somehow enables a strong binding between the graphene layer and the support on which it has been transferred. This would be possible if the graphene has defects which would allow the PVA to reach under the layer of graphene and then bind the graphene to the target supporting layer. This in turn would make it impossible to transfer the graphene layer using the wafer bonding approach.

Furthermore, the rigidity of the graphene support is crucial for transfer. Indeed, when graphene transfer was attempted from a rigid support, such as BLG/Ir(111) or SiC, the graphene layer could not be properly put in contact with the target surface.

Our transfer method therefore requires a flexible support for bilayer graphene that is mechanically stacked without using PVA. We present our transfer method, which meets both of these requirements in the next chapter.

4 PTFE assisted transfer

In this chapter we present our PTFE assisted transfer method with which we were able to transfer a monolayer of clean and high-quality graphene in UHV conditions. We use the weak adhesion between two graphene layers supported by a PTFE tape. The BLG/PTFE stack is mounted on a PDMS stamp which allows flexible adaptability to the target surface. The BLG/PTFE is prepared by repeating the chemical etching of a Cu growth substrate twice using PTFE as the support layer for graphene during etching. For a complete characterization of the transfer method, samples obtained using this transfer procedure were analyzed with AES, STM, XAS, and Raman spectroscopy.

4.1 Transfer procedure

Our transfer procedure was inspired by graphene transfer performed by chemical etching of Cu/gr without the need of a support layer [192]. In this transfer method, graphene is first grown by CVD on a thin Cu sheet, then placed in an $FeCl_3$ solution which etches away the Cu, leaving behind only the graphene layer. Due to its hydrophobic nature, the graphene layer stays on the surface of the etching solution, which is then replaced with DI water for rinsing. It is then fished out with the target sample, by pumping the DI water out. This approach is interesting as it allows BLG to be made by stacking, without leaving residue from a support layer such as PMMA or PVA.

In an attempt to reproduce these results, a 5×5 mm^2 piece of CVD grown gr/Cu was cut and marked on the gr side with a blue pen (to check for graphene presence and potential breaking) and placed marked side up in a 0.1 M $FeCl_3$ solution in a beaker. The hydrophobic nature of graphene on the underside of the Cu kept the sample at the surface of the solution, such that the marked side was never in contact with the etching solution. After etching, the $FeCl_3$ solution was pumped out of the beaker with a syringe and replaced gradually with pure DI water. This experimental setup is extremely sensitive to movement. The air flow in the chemical fume hood was enough to break

the graphene on the surface of the etching solution. After multiple experiments, where the gr/Cu was etched for between 24 and 72 hours, we concluded that this technique required an extremely precise pumping procedure which we were unable to attain.

To support the graphene layer during etching, a piece of Teflon (PTFE) tape was used. Figure 4.1 shows schematically our transfer method which we describe in detail hereafter.
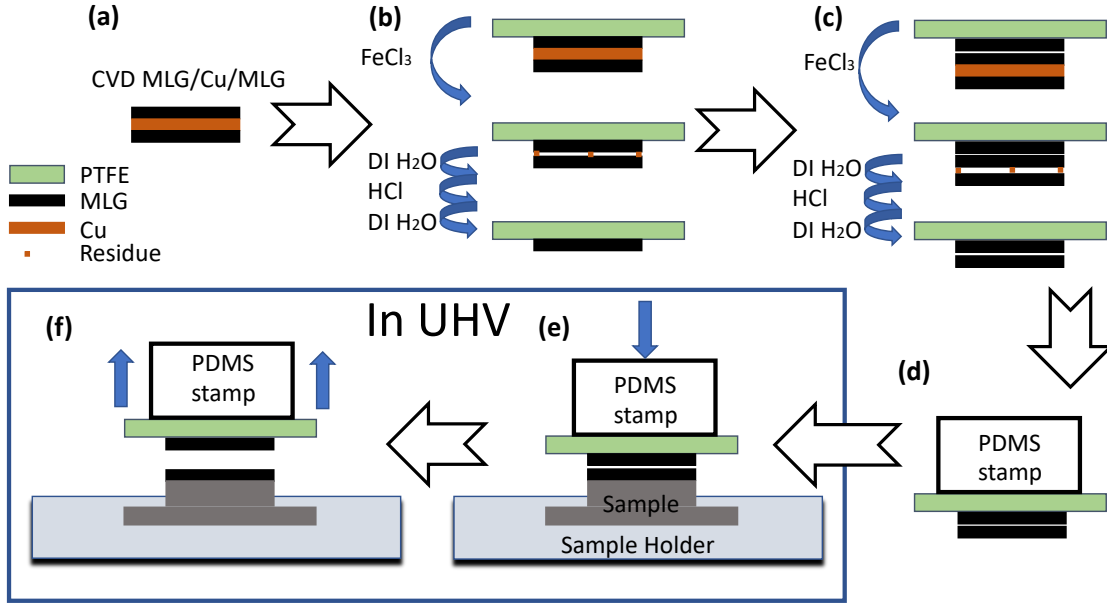
Figure 4.1 – Schematic of the transfer procedure. (a) CVD grown monolayer graphene (MLG) on both sides of Cu. (b) MLG on Cu covered with PTFE tape as a supporting layer. Etching of Cu in FeCl$_3$ solution and rinsing in DI water followed by etching in HCl and rinsing in DI water removes the bottom layer of graphene and residue and leaves a MLG on PTFE. (c) Same procedure as (b) but using PTFE/MLG as support layer. Etching and subsequent rinsing in DI water leaves a BLG on PTFE. (d) Attach PTFE/BLG onto PDMS stamp and transfer into vacuum chamber. (e) Press on clean target sample in UHV. (f) Lift off PDMS/PTFE/MLG leaving behind MLG on target.

We start from a 5×5 mm^2 large sample of CVD grown (see section 2.6.1) graphene on polycrystalline Cu (MLG/Cu/MLG) (fig. 4.1 (a)). This sample is pressed onto a PTFE tape by hand for 5 seconds with a glass plate in an ambient environment. The MLG/Cu/MLG/PTFE stack is placed with the graphene facing downwards in a 0.1 molar (M) FeCl$_3$ solution for 10 hours in order to etch the Cu away (fig. 4.1 (b)). During this process, the PTFE/MLG/Cu/MLG floats on the surface of the etching solution. After etching, a bilayer of graphene covered by PTFE is left floating on the surface. This stack is rinsed in deionized (DI) water for 1 hour. The surface graphene layer is weakly bound to the graphene layer in contact with the PTFE due to intercalation of the etching solution between the two graphene layers and the hydrophobic nature of graphene. Upon contact with the DI water, the change in surface tension causes the top layer of graphene to break in parts along with etching residue (Fe from the FeCl$_3$

solution), which then slide apart, leaving behind a single layer of graphene sticking to PTFE. We confirmed this with Raman spectroscopy by comparing spectra before and after rinsing. This PTFE/MLG sample is then placed with graphene facing downwards in a 0.3 M HCl solution for another 10 hours to achieve further etching of remaining Cu residue and residual Fe ions from the preceding etching solution.

This PTFE/MLG stack is then dried in air after rinsing in DI water. The same procedure is repeated with a second piece of MLG/Cu/MLG, this time using the PTFE/MLG formed in step (b) as the supporting layer (fig. 4.1 (c)). Because the two graphene layers are placed in contact in air, no DI water lies in between and the two layers bind together by van-der-Waals forces. The etching process yields 3 layers of graphene, and again, the top-most layer and etching residues are removed after rinsing in DI water, leaving behind bilayer graphene on PTFE (PTFE/BLG) (see fig. 4.2 (c)). The PTFE/BLG sample is placed with graphene facing downwards in a 0.3 M HCl solution for 10 hours. Finally, after rinsing in DI water, a bilayer of graphene on PTFE tape is obtained (see below for Raman spectroscopy analysis).

The PTFE/BLG stack is subsequently fixed with kapton tape onto a PDMS stamp (see fig. 4.2 (d)), which is then used as the source for a wafer bonding transfer in UHV. First, the entire stamp is introduced into UHV via the load-lock. Using our wobble stick (see section 2.5.1), the PDMS/PTFE/BLG source and target sample are aligned parallel to each other. The BLG is then pressed against the target surface at room temperature for approximately 10 seconds with 30 N force (fig. 4.1 (e)). The vacuum pressure increase during the transfer process is below 1×10^{-10} mbar. After lifting off the stamp, the top layer of graphene is transferred onto the target, as we will show below, while the PTFE with the first graphene layer remains attached to the stamp (fig. 4.1 (f)).

In figure 4.2 (a), the square piece of CVD grown graphene on Cu is placed onto the PTFE tape and pressed gently to flatten the Cu onto the PTFE.

Our Cu etching solution (0.1 M $FeCl_3$) was prepared by mixing solid Iron(III) chloride hexahydrate ($FeCl_3 \cdot 6H_2O$, Sigma Aldrich) with DI water. For complete etching of the 25 μm thick Cu, the sample was immersed in the solution at room temperature for a minimum of 8 hours.

4.2 Auger analysis

We measure the quantity of transferred graphene by *in-situ* AES. The relative intensities of the main transition peaks of carbon and substrate (Ir(111) or Cu(100)) for samples obtained by transfer are compared with reference samples of monolayer graphene grown by CVD on both Ir and Cu. The gr/Ir(111) reference was grown in the UHV chamber (see section 2.6.2), but the graphene on polycrystalline Cu reference was grown in an
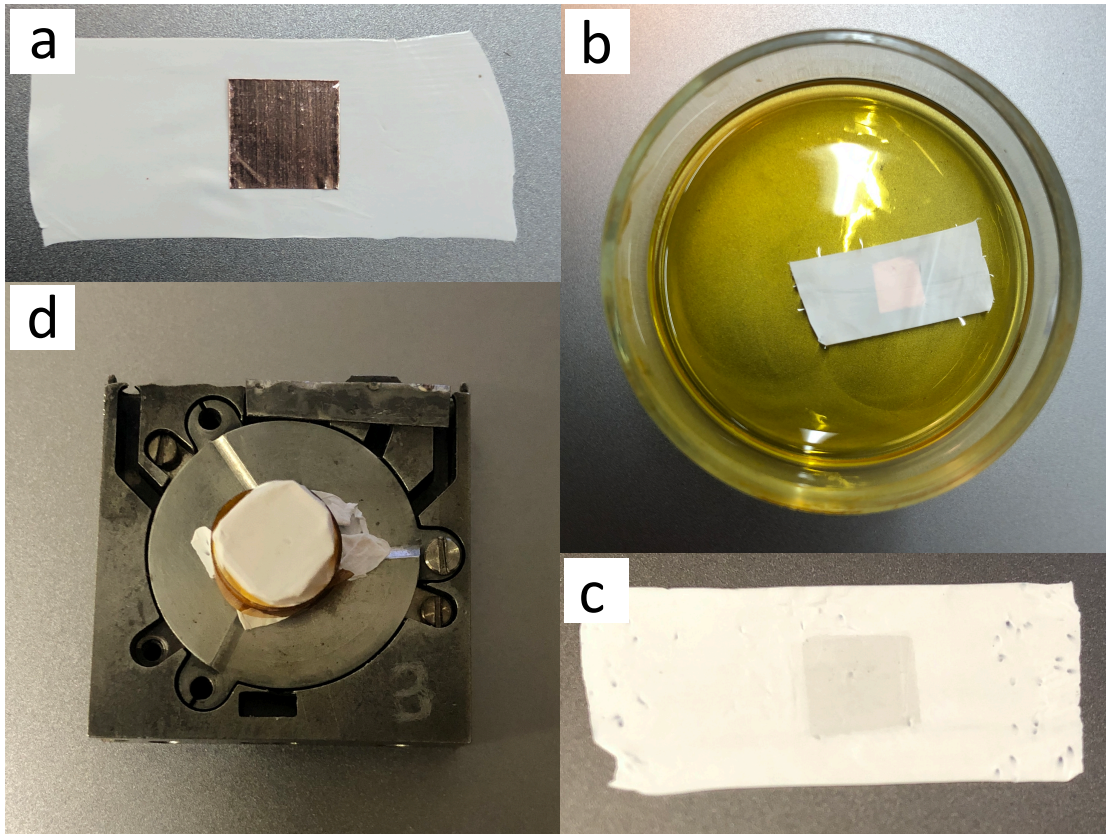
Figure 4.2 – Pictures of the transfer procedure. (a) MLG/Cu/MLG covered with Teflon (PTFE) tape as a supporting layer (upside-down). (b) Etching of Cu in FeCl₃ solution. (c) BLG on PTFE (after step (c) in the transfer procedure). (d) PTFE/BLG onto PDMS stamp mounted on sample holder (step (d) in the transfer procedure).

external reactor (see section 2.6.1) before being inserted into the UHV chamber. This is due to the difficulty in growing graphene on Cu by CVD in our UHV chamber.

In figure 4.3, we show Auger spectra of clean Ir(111), of the reference gr/Ir(111) grown by CVD, and of the gr/Ir(111) sample obtained by our UHV transfer method, the latter immediately after transfer at 80 ℃ and after annealing to 1000 ℃ to study the effect of annealing on the transfer. Each spectrum was normalized to the intensity of the Iridium main peak, and the background was removed by subtraction of a fourth degree polynomial. The most noticeable difference between the pristine and annealed samples obtained by transfer is the shape of the carbon peak. The carbon peak of the pristine sample is broader than the annealed and CVD grown samples, which could be due to the fact that the graphene is floating on the surface and not chemically bound. Indeed, a narrowing of the peak is observed after annealing. The shape of the shoulder at approx. 260 eV is also more similar to the CVD-grown sample upon annealing.

Figure 4.3 – Differential Auger spectra obtained on clean Ir(111), CVD grown graphene on Ir(111), gr/Ir(111) after the PTFE-assisted UHV transfer, and after post-transfer annealing to 1000 ℃. Th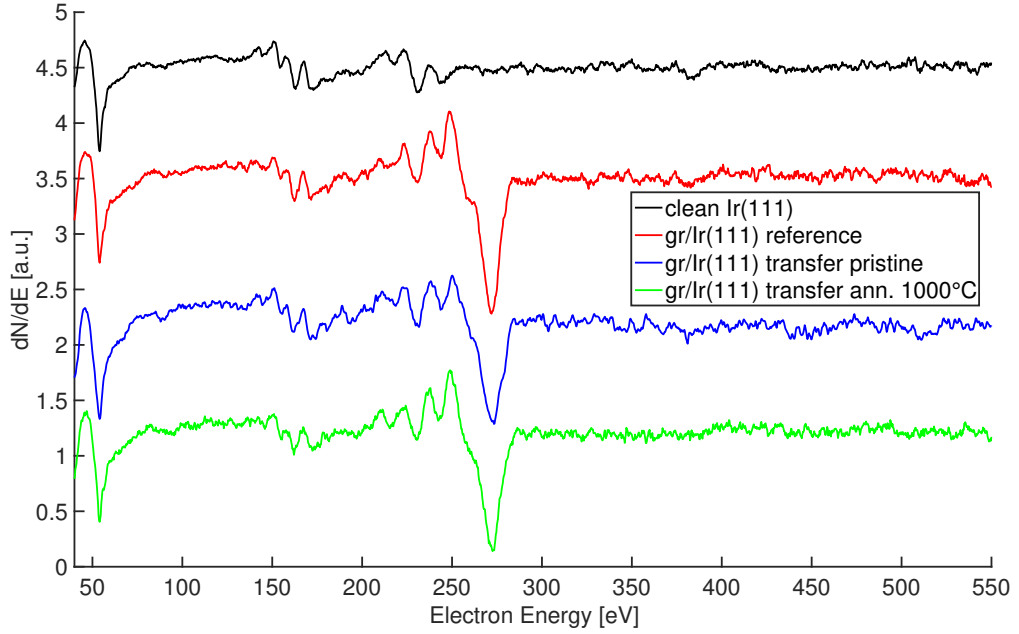e intensity is normalized to the Ir peak height. The spectra are offset for clarity. Primary electron energy 3 kV, 0.3 eV step in analyzer energy and 0.65 μA current on the sample.

Table 4.1 shows the intensity ratios of the main carbon peak to the main peak of Ir, or of Cu (LMM transition at 920 eV) for both CVD grown and transferred graphene (the Cu spectra are not shown in Fig. 4.3). For comparison, we also include the results obtained with our PVA-assisted transfer method described in section 3.6. In order to estimate the amount of transferred graphene, we assumed a linear dependence between the I_C/I_{Ir} (or I_C/I_{Cu}) peak intensity ratios and the coverage. The coverage is given in monolayers (ML) and by definition, for the CVD grown gr/Ir(111) sample, where a self-limiting full monolayer is formed, is 1.0 ML. The pristine transferred sample is characterized by a coverage of 0.8 ML, whereas the sample annealed in UHV is characterized by 0.9 ML. This variation is attributed to the fact that the spectra were not acquired on the exact same area since annealing is performed on the main stage (see section 2.5.1) of our UHV chamber and because we transfer a graphene layer that does not completely cover our sample (7 mm in diameter), the measurement spot could induce variations in the ratio. Indeed, we acquired three Auger spectra on different points of another sample, for which we obtained an average coverage of 0.9 ± 0.1 ML. Segregation of carbon atoms from Ir bulk was excluded by annealing clean Ir(111) to 1000 ℃ which did not cause any AES detectable amounts of C. The same amount of transferred graphene was observed on the Cu(100) surface. Therefore we are able to transfer very close to a full ML of graphene, which after annealing, displays within our resolution the same AES spectrum than CVD

grown graphene.

The last column of Table 4.1 shows the energy separation between C and Ir peaks, averaged over 5 samples and are given with a confidence interval evaluated as the standard deviation of the dispersion of the values measured on different samples. For pristine transferred gr/Ir(111) samples this value is 220 eV, whereas after annealing to 1000 ℃, it decreases to 218 eV, which is the value we find for the CVD grown graphene on Ir(111) reference. Samples annealed to 500 ℃ were also characterized by the same energy separation of 220 eV. The approximately 2 eV chemical shift in the peak positions suggests that the annealing process induces a change in the bonding of graphene to the substrate and makes it identical to the CVD grown graphene/Ir(111). The temperature at which this transition occurs is between 500 ℃ and 1000 ℃.

For the pristine and annealed gr/Cu samples, the difference in energy separation between Cu and C peaks suggests a similar gr/substrate interaction in the two cases.

Because the transfer procedure includes the dissolution of the copper support with FeCl3 acid, we tested if any Cu or Fe residues remain on the surface. High energy resolution (0.1 eV) spectra were acquired post-transfer within close ranges of the main Cu and Fe absorption peaks (920 eV and 710 eV [149] respectively) but no signal has been detected suggesting that both Fe and Cu contamination is below our experimental resolution of about 2-3 % ML.

Table 4.1 – Auger main peak intensity ratios (in brackets the graphene growth/deposition method), I_C/I_{Ir} for graphene on Ir(111) or I_C/I_{Cu} for graphene on amorphous Cu and on Cu(100), estimated graphene coverage in monolayers, and energy difference $\Delta E = E(C)-E(substrate)$ between C and substrate main AES peaks

Substrate	Main peak ratio	Coverage [ML]	ΔE [eV]
Ir(111) (CVD grown in-situ)	1.82 ± 0.06	1.00 ± 0.03	218 ± 0.5
Ir(111) (PTFE, pristine)	1.42 ± 0.07	0.78 ± 0.04	220 ± 0.5
Ir(111) (PTFE, ann. 1000 ℃)	1.62 ± 0.07	0.89 ± 0.04	218 ± 0.5
Ir(111) (PVA, ann. 500 ℃)	2.26 ± 0.12	1.24 ± 0.07	218.5 ± 1.0
Ir(111) (PVA, ann. 1100 ℃)	2.13 ± 0.11	1.17 ± 0.06	217.5 ± 1.0
Polycrystal. Cu (CVD, ann. 150 ℃)	0.57 ± 0.06	1.0 ± 0.1	648.5 ± 0.5
Cu(100) (PTFE, pristine)	0.45 ± 0.05	0.80 ± 0.09	649.3 ± 0.5

It is interesting to compare our PTFE-assisted transfer method with a PVA assisted transfer method [54]. With this latter method we were able to transfer graphene to a target surface both in air (on polycrystalline Cu, SiO_2 and Al_2O_3) and in UHV (on clean Ni(111) and Ir(111)). However, after transfer in UHV, the sample must be exposed to air and placed in hot water for PVA removal, before being reinserted in UHV. After reinserting the sample in the UHV chamber, the Auger spectrum revealed very large amounts of carbon and oxygen on the surface, masking almost entirely the Iridium peaks. This large quantity of carbon (along with oxygen) is attributed to residues of PVA which

are not entirely removed during the immersion in hot water. Annealing to 500 ℃ for 15 minutes partially removes the PVA residues with the I_C/I_{Ir} ratio close to 6.75, in contrast to the reference value of 1.82 (see Table 4.1). Even upon annealing to 1100 ℃, PVA residues are still present, with an excess of 30 % of amorphous C remaining on the surface as shown by the value of the I_C/I_{Ir} ratio in Table 4.1). A similar trend is also observed for the air transferred samples for which it was possible to have a mostly clean graphene layer only after annealing to 450-500 ℃ for 30 minutes in UHV.

4.3 STM analysis of transferred gr/Ir(111)

STM performed in-situ on transferred gr/Ir(111) annealed to 1000 ℃ shows that the surface is mainly covered by the characteristic moiré pattern formed by CVD grown graphene on Ir(111) [24, 193] (see fig. 4.4 (a)). A fraction (2 % in this STM image) of the surface is covered by residue appearing as white islands in the image with a mean apparent height of about 10 Å. Multiple domains (marked with white dotted lines) of the graphene moiré pattern can be seen, as is expected for CVD-grown graphene on polycrystalline Cu used as source for the UHV transfer. The standard deviation of the dispersion of the different domain orientations is 8°. The residue mainly agglomerates at domain boundaries. Statistical analysis of the residue density observed over 30 STM images acquired on different surface areas and on 7 different samples showed an average residue coverage of 4 % (fraction of the surface covered by these residues). The chemical composition of these residues is uncertain; the O and Fe content are below the detection limit of our AES, which suggests that they are mainly composed of amorphous carbon.

For annealing temperatures below 1000 ℃ we were unable to observe the moiré structure formed by gr on Ir(111). This could be due to a change of adsorption strength upon annealing. The bonding of graphene to Ir(111) is mainly due to van der Waals interaction; a weak covalent bond is however formed in the hcp and fcc moiré regions where the distance between C and Ir atoms is reduced [194]. The annealing might structurally rearrange the transferred graphene and transform the interaction with the substrate from exclusively van der Waals into a coexistence of van der Waals and covalent bonded regions in such a way as to enable the formation of the moiré pattern. This hypothesis is supported by the observed shift in the relative position of C and Ir AES peaks (see last column of table 4.1).

The lack of moiré could also be due to the fact that the transferred graphene has too small domains for the moiré to form [14]. A somewhat similar situation reported in the literature is represented by samples with an incomplete graphene layer made of separated islands, obtained by exposing the Ir(111) surface to ethylene at room temperature. This type of method, called temperature programmed growth (TPG) where the precursor molecule is adsorbed at low temperature and annealed afterwards is very different from CVD, where the precursor is adsorbed on the surface at high temperature. For these samples obtained

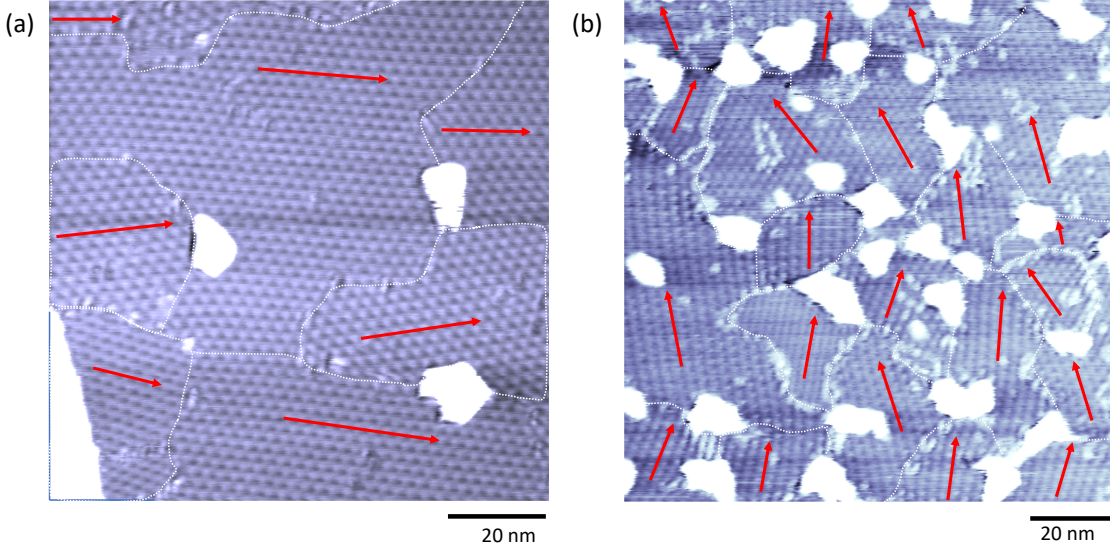by TPG, the moiré structure only appeared upon annealing to 730 ℃ [13].

(a)

(b)

20 nm

20 nm

Figure 4.4 – STM images of UHV transferred graphene on Ir(111). (a) PTFE assisted method 1000 Å× 1000 Å ($V_t = +0.3$ V, $I_t = 10$ nA, $T = 20$ ℃). (b) PVA assisted method 1200 Å× 1200 Å ($V_t = -1.4$ V, $I_t = 300$ pA, T = 20 ℃). In both cases, after transfer at 20 ℃ the sample has been annealed to $T_{ann} = 1000$ ℃.

For comparison, the STM image acquired on a sample produced with the PVA assisted method (see fig. 4.4 (b)) shows approximately 20 domains characterized by different moiré periodicities and orientations. The standard deviation of the dispersion of the different domain orientations is 21°, in contrast to the 8° standard deviation for the PTFE-assisted transfer. In addition, large islands with an apparent height of 15 Å of residue are localized at the boundaries of graphene domains and cover roughly 15 % of the surface. The average size of the graphene domains with the PVA method is 700 nm². In contrast, using the PTFE assisted transfer method, the sample is much less contaminated by carbon and we obtained graphene domains at least twice as large.

These results suggest that the PTFE-supported chemical etching is less damaging than the PVA-supported delamination process. The timescale of the isolation of the graphene layer from its growth substrate (a few minutes for PVA deposition and delamination from Cu and a few hours for PTFE-supported chemical etching) is believed to play a significant role, allowing graphene to slowly adapt to the carrier layer.

4.4   X-ray absorption spectroscopy analysis

The XANES spectra were acquired at the X-Treme endstation (synchrotron) at room temperature at the K-edge of C on both in-situ CVD-grown graphene on Ir(111) (on two

different Ir(111) crystals) and on two (one high and one low quality, due to a bad transfer) gr/Ir(111) samples prepared using our PTFE-assisted transfer method (see figure 4.5). Incident x-rays arrive at 60° incidence on the sample surface and are polarized at 0° and 90° (see fig 2.5). The transferred samples were exposed to air on their way from our lab to the synchrotron. Therefore they were annealed once inserted into the UHV chamber of the X-Treme endstation to 150 ℃ prior to measurements. To take into account pollution of the optical elements of the beam-line, spectra were acquired on a clean Ir(111) sample and subtracted from the gr/Ir(111) samples prepared by CVD or by transfer.

These spectra were acquired at a different beam-time than the one where the samples obtained by the PVA-assisted transfer procedure were analyzed (see XAS analysis in section 3.4.2). During acquisitions, in order to avoid measurement artefacts due to changes in the x-ray beam, the signal of an Au grid placed upstream with respect to the sample is acquired simultaneously. Spectra can then be normalized with respect to the Au grid signal, supposing that the signal is flat around the energies of interest. In the case where this Au grid is polluted, the normalization may lead to erronous data. During this beam-time, we were unable to properly clean this Au grid, and therefore instead of applying the normalization based on the Au grid signal, we plot the difference between the spectra acquired with the two incident x-ray polarizations (90°- 0°), also known as XLD. Both the π electron orbital absorption peak at 285 eV and the σ electron orbital absorption peak at 292 eV are visible.
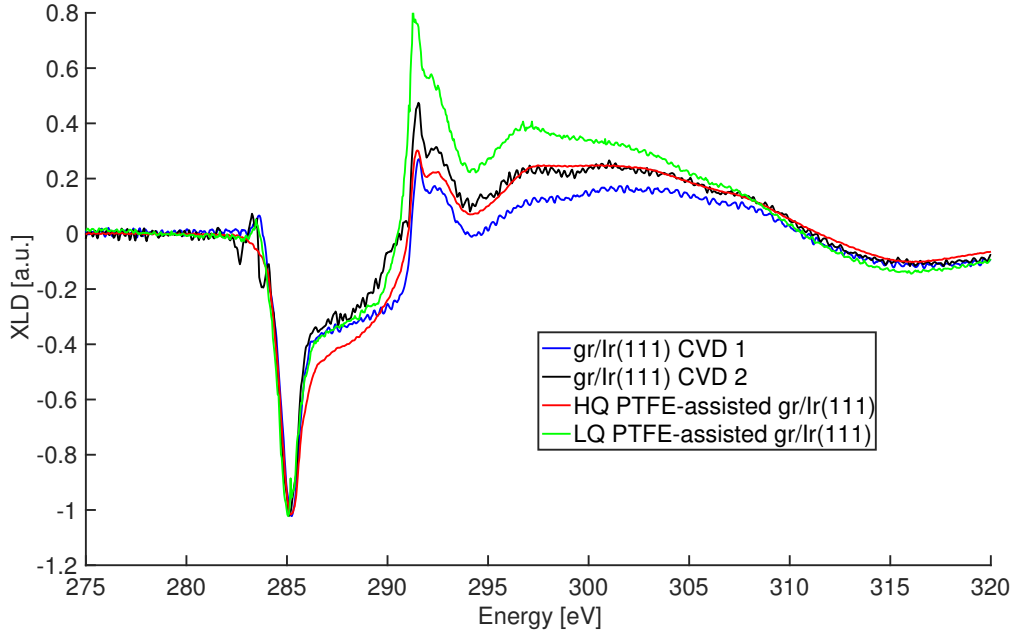

Figure 4.5 – XLD spectra of graphene on Ir(111) by both CVD and by PTFE-assisted transfer (one high-quality (HQ) and one low-quality (LQ)). π orbitals peak at 285 eV and σ orbitals peak at 292 eV. The spectra were acquired at 60° incidence at room temperature and normalized to the π peak intensity.

The spectra acquired on the two CVD-grown samples differ slightly, either because they were grown on different crystals, or because of the alignment of the x-ray incident angle with the surface normal, which is done with a precision of 2-3°. This factor also affects the transferred samples.

The spectrum of the HQ PTFE-assisted gr/Ir(111) is identical to the CVD grown samples, within the errors due to Ir crystal and x-ray incident angle alignment pointing out a high crystalline order and a flat arrangement of the transferred graphene. In contrast, the LQ PTFE-assisted gr/Ir(111) is characterized by a broader σ electron orbital peak and by a higher overall intensity, suggesting a disordered and rough graphene arrangement. These results show that our transfer method allows us to transfer a flat graphene and not a wrinkled layer, thus supporting the hypothesis that the lack of moiré prior to annealing to 1000 ℃ is not due to high rugosity, but that the graphene needs to undergo a change in adsorption type from full physisorption to partial chemisorption.

4.5 Raman analysis

Figure 4.6 shows the comparison between the Raman spectrum acquired on PTFE transferred gr/Cu(100) and on graphene grown by CVD on amorphous Cu. In addition, in order to characterize the graphene quality throughout the different steps of the transfer procedure, figure 4.7 (a) shows the Raman spectra acquired on the first layer of graphene on PTFE (MLG/PTFE), the graphene bilayer on PTFE after the second etching of gr/Cu (BLG/PTFE) and the monolayer of graphene on PTFE after transfer of the top layer onto Cu(100) (MLG/PTFE). For clarity, figures 4.7 (b) and (c) are enlargements of the superposed G and 2D bands, respectively.

From a qualitative inspection of figure 4.6 we note that the two spectra are almost identical, although the $I(D)/I(G)$ peak height ratio is slightly lower for the CVD grown graphene on Cu, indicating a small loss of quality during transfer. Analyzing the spectra more quantitatively, we first note that the peak at 2330 cm^{-1} is an artefact and the peak located at 2450 cm^{-1} is believed to be an overtone, a combination between a band around 1100 cm^{-1} and the D band (1350 cm^{-1}) [140].

The average peak intensity ratios and peak full width at half maximum (FWHM) for the spectra shown in figures 4.6 and 4.7 are given in Table 4.2. The peaks have been fitted by Lorentzian or Gaussian functions (best fit chosen) after background removal and normalization to the area under 2000-2200 cm^{-1}. Each value is given with a confidence interval evaluated as the standard deviation of the dispersion of the values measured in different spots. Depending on the substrates, the difference between monolayer and bilayer is small. This is independent of the quality of the measurement, and depends on the studied system, where small local variations are of the same order of magnitude than the differences between MLG and BLG, hence we rely on the mean values for our
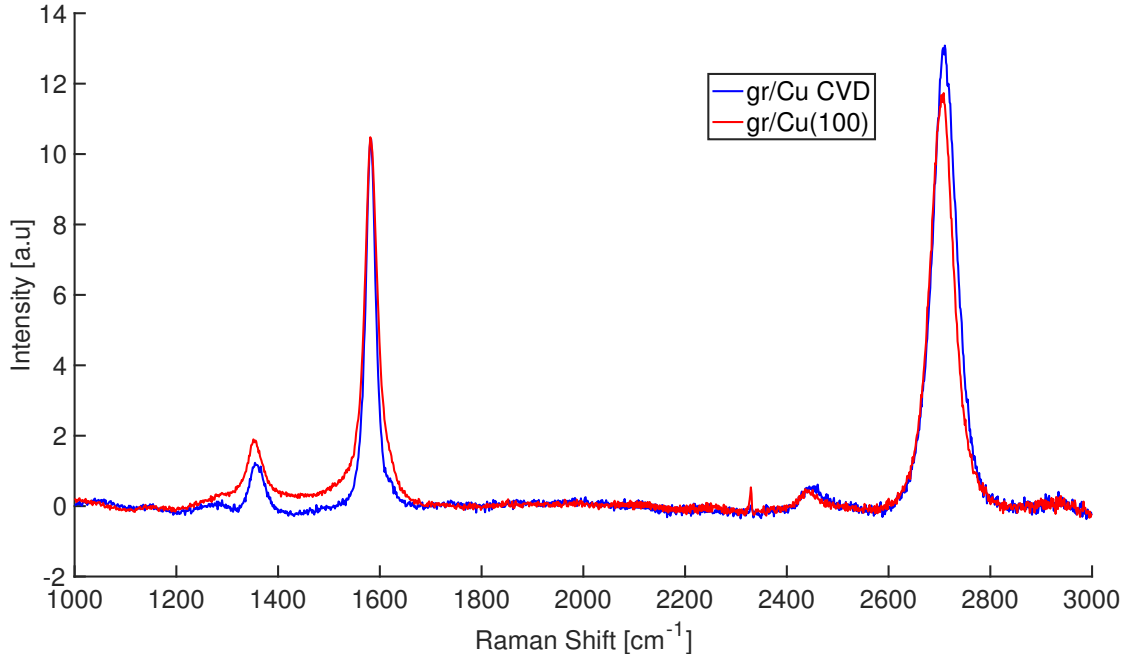
Figure 4.6 – Raman spectra of CVD grown graphene on Cu and PTFE-assisted transferred graphene on Cu(100). 488nm laser wavelength, 2400 l/mm grating, averaged over 5 sample regions.

analysis.

The FWHM of the 2D band increases from 42 cm^{-1} for PTFE/MLG to 49 cm^{-1} for PTFE/BLG and decreases to 44 cm^{-1} for PTFE/MLG after the top layer has been transferred. The $I(G)/I(2D)$ ratio follows the same trend, increasing from 0.72 for PTFE/MLG to 0.79 in PTFE/BLG, and decreasing to 0.71 for PTFE/MLG post-transfer. These numbers clearly demonstrate that we have MLG/PTFE after the first step, BLG/PTFE after the second step and the entire top layer of the bilayer graphene attached to the PTFE stamp is transferred to the target surface during the transfer procedure. Indeed, an increase in both the FWHM of the 2D band and the $I(G)/I(2D)$ ratio has been attributed to an increase in graphene layers [133, 134]. The G band FWHM follows the same trend, increasing from 37 cm^{-1} (for MLG/PTFE) to 44 cm^{-1} (for BLG/PTFE) and reducing back to 27 cm^{-1} (for MLG/PTFE post-transfer).

To characterize the graphene structural quality, the $I(D)/I(G)$ ratio of graphene on Cu(100) post-transfer was compared to the CVD grown graphene on amorphous Cu. The average value of this ratio increases from 0.12 to 0.15, a 20 % increase, suggesting a small average loss in quality during transfer. However, the similar spatial variation implies that we do not stress the graphene layer inhomogeneously during transfer, thanks to the flexibility of the PTFE support layer and the PDMS stamp. The $I(G)/I(2D)$ ratio is identical for both the CVD grown and transferred sample, suggesting that a full
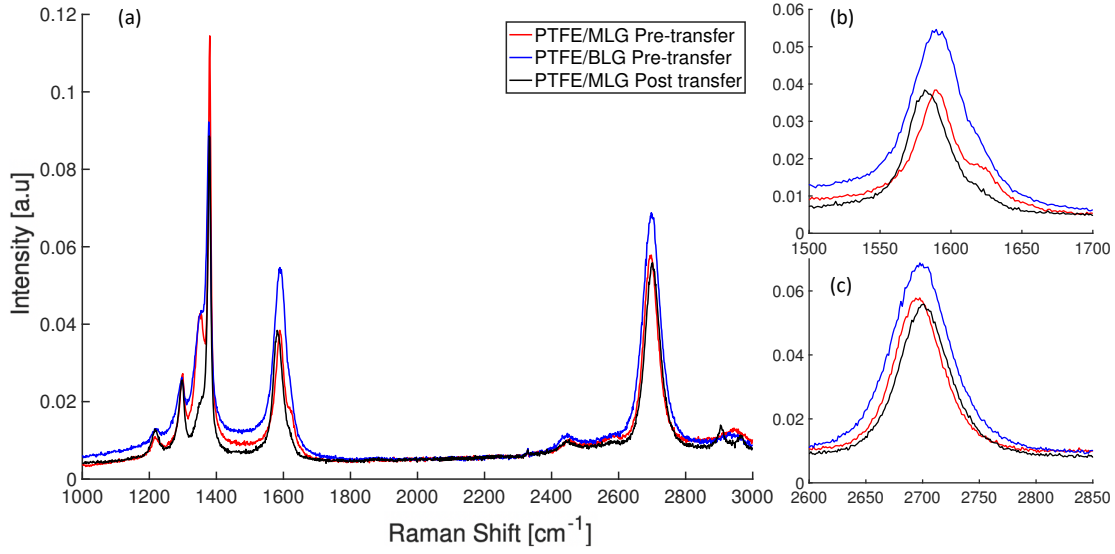
Figure 4.7 – Raman characterization of graphene on the PTFE carrier. (a) MLG/PTFE pre-transfer, BLG/PTFE pre-transfer and MLG/PTFE post-transfer of the top graphene layer in UHV. (b) and (c), enlargements and superpositions of respectively G and 2D bands for all three spectra. 488nm laser wavelength, 2400 l/mm grating, averaged over 8 sample regions.

monolayer is transferred (within the measured areas).

We note that it is difficult to quantify the structural degradation that graphene can suffer due to attachment to the stamp. As can be seen in figure 4.7, the Raman spectrum of PTFE has a large band at around 1380 cm^{-1} making it impossible to distinguish the D band of graphene from the tail of this peak. One could try to subtract a PTFE reference spectrum to dig out the D band, but this would not be straightforward. The $I(\mathrm{D})/I(\mathrm{G})$ ratio can therefore not be used easily as an indicator of graphene quality for this specific case. However, optimizing graphene quality pre-transfer should improve post-transfer quality.

From our experiments, we also conclude that it is mandatory to have the second layer of graphene on top of the first MLG/PTFE. Indeed, if the stacking procedure was not repeated (fig. 4.1 (c)), and we tried transferring graphene from MLG/PTFE to a target by pressing, no graphene was transferred because the adhesion to the PTFE was stronger than the adhesion to the target.

4.6   Damaged graphene on Ir(111)

As has been discussed in section 2.6.2, the growth of graphene on an Ir(111) crystal yields a continuous quasi-defect-free graphene layer characterized by a moiré pattern due to lattice mismatch (see fig. 2.16). However, both our growth (on polycrystalline Cu) and

Table 4.2 – Raman characterization of graphene during the different steps of our UHV transfer method. The FWHM is given in cm^{-1}. The values are the averages on multiple measurement spots and are given with a confidence interval evaluated as the standard deviation of the dispersion of the values measured in different spots. The $I(D)/I(G)$ ratio cannot be calculated for graphene on PTFE due to the large PTFE band at around 1380 cm^{-1}. The observed difference in $I(G)/I(2D)$ ratios for the same number of graphene layers on Cu and PTFE is due to the variation of this ratio depending on the underlying substrate [134–136].

Sample	2D FWHM	G FWHM	$I(G)/I(2D)$	$I(D)/I(G)$
CVD grown gr/Cu (step a)	37 ± 2	18 ± 1	0.28 ± 0.03	0.12 ± 0.04
PTFE/MLG (step b)	42 ± 2	37 ± 2	0.72 ± 0.06	-
PTFE/BLG (step c)	49 ± 1	44 ± 1	0.79 ± 0.05	-
PTFE/MLG post transfer (f)	44 ± 3	27 ± 2	0.71 ± 0.06	-
gr/Cu(100) (step f)	31 ± 2	21 ± 4	0.30 ± 0.04	0.15 ± 0.03

our transfer methods may introduce defects in graphene. To characterize the influence of defects on the moiré pattern of graphene, CVD grown gr/Ir(111) was bombarded with ions to induce defects and subsequently imaged by STM.
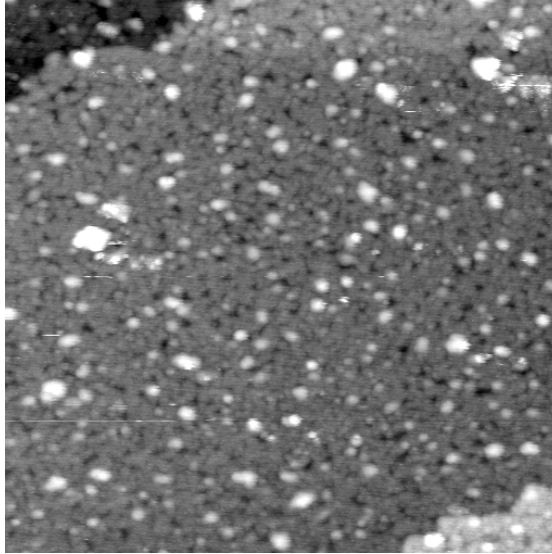
Figure 4.8 – 1000 Å × 1000 Å STM image of gr/Ir(111) damaged by ion bombardment ($V_t = -0.6$ V, $I_t = 100$ nA, T = 300 K)

Graphene was first grown by CVD on Ir(111) as described in section 2.6.2. Following growth, the graphene surface was sputtered with Ar^+ ions at 250 eV at T = 300 ℃ for 240 seconds. The current on the sample was 1 μA. It has been shown that at this energy, the penetration depth of Ar atoms in C is 1-1.5 nm [195] and therefore, both the graphene layer and the underlying iridium are sputtered. To calculate how many atoms were kicked out on average during sputtering from each graphene site, we consider

the sputter yields in normal incidence for Ar^+ ions at 250 eV on both C (0.06) and Ir (0.5) [196]. In our experimental setup, with a 55 ° incidence, this sputtering yield is increased by a factor 2.5 [197]. For bulk Ir, we estimated that 3.75 atoms would be kicked out, whereas for bulk C, this value would be close to 0.45. We considered that the number of atoms kicked out on average for gr/Ir(111) during 240 seconds was in between these two values. As shown in figure 4.8, after sputtering the moiré pattern is no longer visible and instead gives place to a rough grainy structure that covers the Ir(111) surface.

In figures 4.9 (a) and (b), the bombarded sample was annealed in vacuum to respectively 700 ℃ and 1100 ℃. After annealing to 700 ℃, the moiré structure is still not visible and the grainy structure can still be observed on the image, although it seems to be better ordered than before annealing. Indeed, one can see that the grains orient parallel to the Ir(111) step that can be seen on the upper left corner of the image. In contrast, after annealing to 1100 ℃, the moiré structure is clearly visible again. This suggests that at a temperature between 700 ℃ and 1100 ℃, a transition occurs where the graphene layer repairs and the moiré appears. The dark hole visible on the right part of the image is explained by the fact that the sputtering removed part of the C atoms, making their number insufficient to cover the whole Ir(111) surface after the annealing. The 10 Å high white areas that are visible on the upper left of the image are attributed to residue from the sputtering. These may be either Ir atoms or a C-Ir alloy.
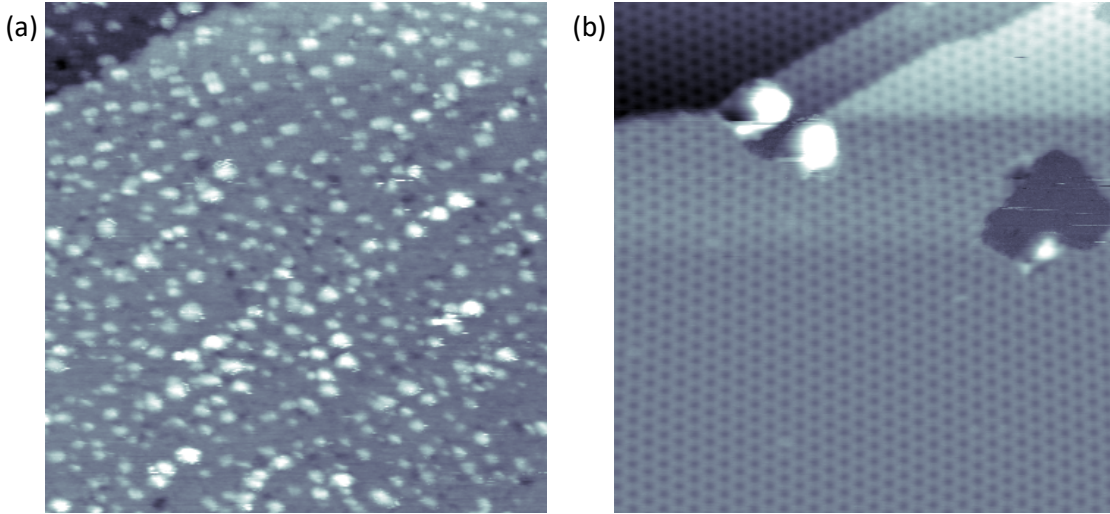
Figure 4.9 – STM images of damaged gr/Ir(111). (a) 1000 Å× 1000 Å, annealed to 700 ℃ (V_t = −0.6 V, I_t = 1 nA, T = 300 K) and (b) 850 Å × 850 Å, annealed to 1100 ℃ (V_t =-0.1 V, I_t = 75 nA , T = 300 K).

A new CVD grown gr/Ir(111) sample was prepared and damaged with the same procedure as described above. Figures 4.10 (a) and (b), show the gr/Ir(111) surface after annealing in ethylene at $3 \cdot 10^{-7}$ mbar for respectively 5 minutes at 850 ℃ and 4 minutes at 1100 ℃. The effect of annealing temperature coincides with what was observed without exposure to C_2H_4. The temperature at which the transition between a seemingly disordered structure
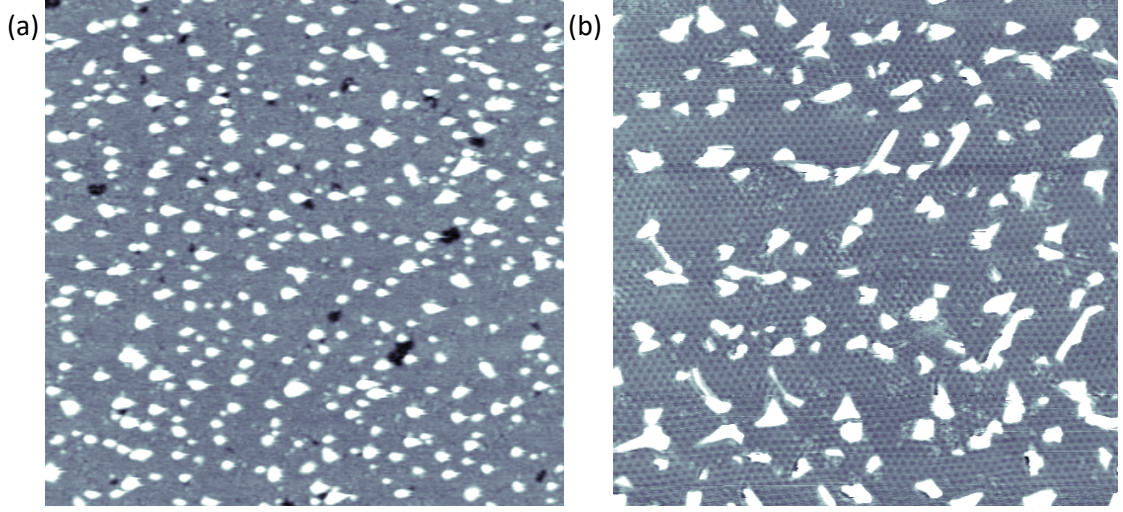
Figure 4.10 – 1500 Å × 1500 Å STM images of gr/Ir(111) (a) annealed to 850 ℃ in $3 \cdot 10^{-7}$ mbar C_2H_4 for 5 min, ($V_t = -0.8$ V, $I_t = 370$ pA, T = 300 K) and (b) annealed to 1100 ℃ in $3 \cdot 10^{-7}$ mbar C_2H_4 for 4 min, ($V_t = -0.8$ V, $I_t = 3$ nA , T = 300 K)

to the appearance of the moiré occurs is between 850 ℃ and 1100 ℃. However, annealing in ethylene allows for a full moiré to form on the surface, without holes as could be seen in figure 4.9 (b). The exposed Ir(111) enables C to deposit on the surface and repairs the holes generated by the sputtering. Residue on the surface is, however, still observed and may be again attributed to C and Ir alloy or to Iridium atoms adsorbed on the surface. In contrast to the STM results obtained in both our PVA assisted transfer method (section 3.6) and the PTFE-assisted transfer method (section 3.6), the orientation of the moiré is uniform on the surface. This again suggests that in our transferred samples, where multiple graphene domains (due to the polycrystalline Cu growth substrate) are visible, the annealing step does not repair the graphene to form continuous domains, but as mentioned previously, induces a change in adsorption from full physisorption to partial chemisorption.

4.7   BLG/Ir(111) by PTFE-assisted transfer

When two graphene layers are stacked on top of eachother with a small twist angle θ, the moiré pattern that arises between the two graphene lattices gives rise to remarkable electrical and optical properties strongly correlated to the twist angle. Such properties include flat bands [35], van Hove singularities [198] and superconductivity [40]. To reach these twist angles, graphene transfer is indispensable. In this section we demonstrate the versatility of our transfer method by transferring a single layer of graphene onto gr/Ir(111) grown by CVD (see section 2.6.2).

The Auger spectrum of the CVD-grown graphene is shown in figure 4.11. This spectrum is characterized by $I_C/I_{Ir} = 2.3$. Following this CVD growth, we used our transfer method to transfer graphene onto gr/Ir(111) to obtain BLG/Ir(111). The Auger spectrum of the BLG/Ir(111) is also shown in figure 4.11. This sample is characterized by $I_C/I_{Ir} = 5$, which is 2.2 times larger than the gr/Ir(111) sample. As was shown in section 2.3, a bilayer of graphene on Ir(111) should be characterized by a ratio 3 times as large as the monolayer. Supposing a linear relation between estimated coverage and ratio, we transferred around 60 % of a graphene monolayer.
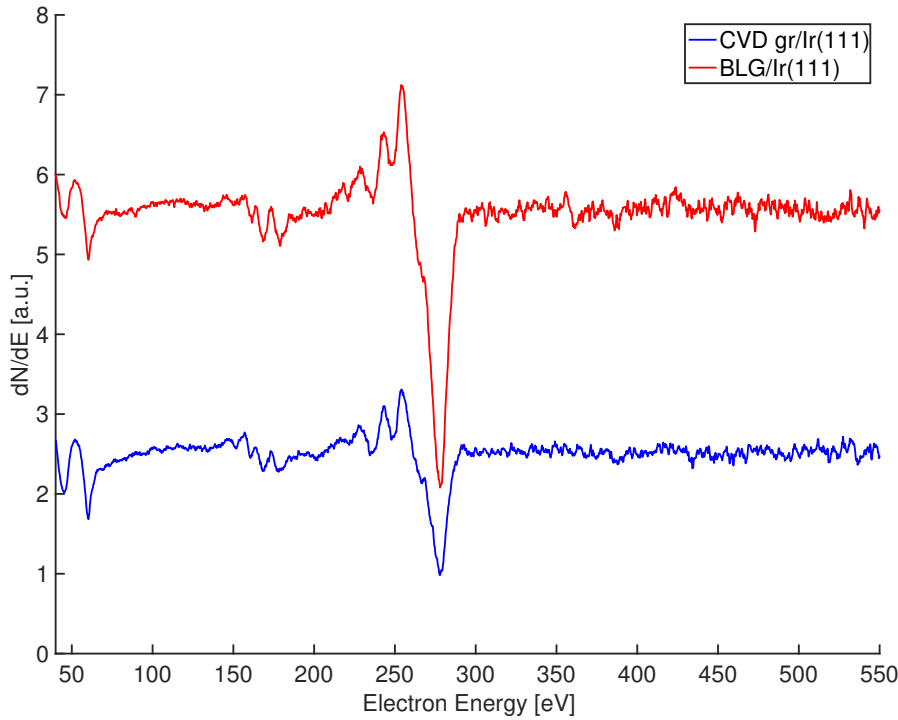
Figure 4.11 – AES spectra of CVD graphene on Ir(111) in blue and BLG/Ir(111) after PTFE-assisted transfer of graphene onto gr/Ir(111) in red. The intensity is normalized to the Ir peak height (at 54 eV). Primary electron energy 3 kV, 0.3 eV step in analyzer energy.

Figure 4.12 shows two STM images of the BLG/Ir(111) sample. The sample was annealed

to 300 ℃ before imaging to desorb air contamination from the surface that could be introduced by the BLG/PTFE stamp.

In figure 4.12 (a), the gr/Ir(111) moiré, with a periodicity of 25.2 Å, can be seen covering most of the surface. In the middle, a larger periodicity moiré, showing contrast inversion, and characterized by a periodicity of 47.6 Å is attributed to tBLG. The height difference is 6 Å, which is attributed to a contribution of the electronic structure. In figure 4.12 (b), the gr/Ir(111) moiré can be seen on the lower right corner, while the majority of the image is covered with a moiré with a periodicity of 68 Å, again, attributed to tBLG. The height difference is 4 Å and contrast inversion is observed between the two regions. These results are similar to what has been obtained by intercalation of C atoms (at a sample temperature of $T = 900 - 950$ ℃), under a CVD grown graphene layer on Ir(111) to form BLG/Ir(111) [113], but differ in the fact that we do not need to anneal the sample to 900 ℃ to deposit the graphene layer.

By growing the source graphene on single crystals, the domain size would be much larger and therefore the defect density would be much lower and would enable large areas of twisted bilayer graphene to be obtained with higher control on twist angles.
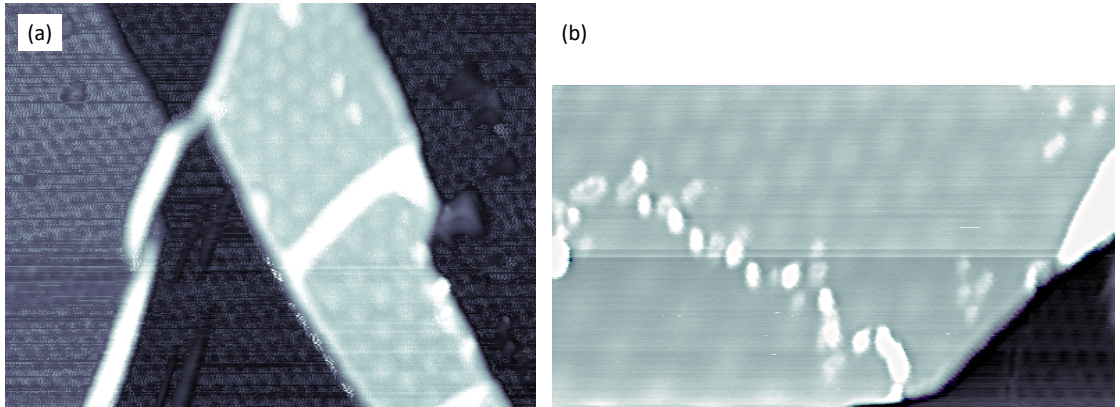
Figure 4.12 – STM images of BLG/Ir(111) on two macroscopically different areas (a) 880 Å× 670 Å ($V_t = +1.9$ V, $I_t = 1$ nA, T = 300 K). (b) 750 Å× 430 Å ($V_t = +0.7$ V, $I_t = 1$ nA, T = 300 K). The BLG/Ir(111) sample has been annealed to $T_{ann} = 300$ ℃.

5 Conclusion and outlook

To the best of our knowledge, this transfer procedure is the first demonstration of a fully UHV-compatible graphene transfer. This enables device fabrication, usually hampered by impurities, to be carried out in UHV, thus enabling fully reproducible and clean results. Further, surface science can be extended to the third dimension, by capping layers and continuing growth etc. under clean conditions. For future studies or improvements, one should investigate if the annealing step needed to get the moiré pattern on Ir(111) is characteristic to Ir(111) as a target or if in general annealing is needed in order to heal graphene or to increase domain sizes. In that case, one might consider growing higher quality graphene on single-crystal Cu in order to start with larger graphene domain sizes.

Further, starting with very high quality graphene would improve control on the orientation of the graphene domain and enable the stacking with a controlled angle of graphene layers for studies in twistronics. This could be combined with improvements to the transfer mechanism, by for instance designing a vertical press, with controlled alignment and pressing force.

Cleanliness of the transfer can be further improved by optimizing the etching procedure or by using alternative graphene isolation procedures with reduced residue such as electrochemical bubbling, especially when using precious single crystals that could be reused for new growths.

Bibliography

[1] B. C. Brodie. *XIII. On the atomic weight of graphite.* Philos. Trans. R. Soc. Lond. **149**, 249–259 (1859).

[2] P. R. Wallace. *The Band Theory of Graphite.* Phys. Rev. **71**, 622–634 (1947).

[3] K. S. Novoselov, A. K. Geim, S. V. Morozov, D. Jiang, Y. Zhang, S. V. Dubonos, I. V. Grigorieva, and A. A. Firsov. *Electric Field Effect in Atomically Thin Carbon Films.* Science **306**, 666–669 (2004).

[4] K. S. Novoselov, A. K. Geim, S. V. Morozov, D. Jiang, M. I. Katsnelson, I. V. Grigorieva, S. V. Dubonos, and A. A. Firsov. *Two-dimensional gas of massless Dirac fermions in graphene.* Nature **438**, 197–200 (2005).

[5] M. Lotya, Y. Hernandez, P. J. King, R. J. Smith, V. Nicolosi, L. S. Karlsson, F. M. Blighe, S. De, Z. Wang, I. T. McGovern, G. S. Duesberg, and J. N. Coleman. *Liquid Phase Production of Graphene by Exfoliation of Graphite in Surfactant/Water Solutions.* J. Am. Chem. Soc. **131**, 3611–3620 (2009).

[6] M. Lotya, P. J. King, U. Khan, S. De, and J. N. Coleman. *High-Concentration, Surfactant-Stabilized Graphene Dispersions.* ACS Nano **4**, 3155–3162 (2010).

[7] E. Rollings, G.-H. Gweon, S. Zhou, B. Mun, J. McChesney, B. Hussain, A. Fedorov, P. First, W. de Heer, and A. Lanzara. *Synthesis and characterization of atomically thin graphite films on a silicon carbide substrate.* J. Phys. Chem. Solids **67**, 2172–2177 (2006).

[8] M. S. A. Bhuyan, M. N. Uddin, M. M. Islam, F. A. Bipasha, and S. S. Hossain. *Synthesis of graphene.* Int. Nano Lett. **6**, 65–83 (2016).

[9] K. E. Whitener and P. E. Sheehan. *Graphene synthesis.* Diam. Relat. Mater. **46**, 25 – 34 (2014).

[10] J.-H. Lee, E. K. Lee, W.-J. Joo, Y. Jang, B.-S. Kim, J. Y. Lim, S.-H. Choi, S. J. Ahn, J. R. Ahn, M.-H. Park, C.-W. Yang, B. L. Choi, S.-W. Hwang, and D. Whang. *Wafer-Scale Growth of Single-Crystal Monolayer Graphene on Reusable Hydrogen-Terminated Germanium.* Science **344**, 286–289 (2014).

Bibliography

[11] Y. Zhang, L. Zhang, and C. Zhou. *Review of Chemical Vapor Deposition of Graphene and Related Applications.* Acc. Chem. Res. **46**, 2329–2339 (2013).

[12] X. Li, W. Cai, J. An, S. Kim, J. Nah, D. Yang, R. Piner, A. Velamakanni, I. Jung, E. Tutuc, and et al. *Large-Area Synthesis of High-Quality and Uniform Graphene Films on Copper Foils.* Science **324**, 1312–1314 (2009).

[13] J. Coraux, A. N'Diaye, M. Engler, C. Busse, D. Wall, N. Buckanie, F. Meyer zu Heringdorf, R. Gastel, B. Poelsema, and T. Michely. *Growth of graphene on Ir(111).* New J. Phys. **11** (2009).

[14] J. Coraux, A. T. N'Diaye, C. Busse, and T. Michely. *Structural Coherency of Graphene on Ir(111).* Nano Lett. **8**, 565–570 (2008).

[15] J. Wood, S. Schmucker, A. Lyons, E. Pop, and J. Lyding. *Effects of Polycrystalline Cu Substrate on Graphene Growth by Chemical Vapor Deposition.* Nano Lett. **11**, 4547–54 (2011).

[16] S. Y. Zhou, G. H. Gweon, A. V. Fedorov, P. N. First, W. A. de Heer, D. H. Lee, F. Guinea, A. H. Castro Neto, and A. Lanzara. *Substrate-induced bandgap opening in epitaxial graphene.* Nat. Mat. **6**, 770–775 (2007).

[17] M. S. Nevius, M. Conrad, F. Wang, A. Celis, M. N. Nair, A. Taleb-Ibrahimi, A. Tejeda, and E. H. Conrad. *Semiconducting Graphene from Highly Ordered Substrate Interactions.* Phys. Rev. Lett. **115**, 136802 (2015).

[18] M. Yankowitz, J. Jung, E. Laksono, N. Leconte, B. L. Chittari, K. Watanabe, T. Taniguchi, S. Adam, D. Graf, and C. R. Dean. *Dynamic band-structure tuning of graphene moirésuperlattices with pressure.* Nature **557**, 404–408 (2018).

[19] A. C. Ferrari, F. Bonaccorso, V. Fal'ko, K. S. Novoselov, S. Roche, P. Bøggild, S. Borini, F. H. L. Koppens, V. Palermo, N. Pugno, J. A. Garrido, R. Sordan, A. Bianco, L. Ballerini, M. Prato, E. Lidorikis, J. Kivioja, C. Marinelli, T. Ryhänen, A. Morpurgo, J. N. Coleman, V. Nicolosi, L. Colombo, A. Fert, M. Garcia-Hernandez, A. Bachtold, G. F. Schneider, F. Guinea, C. Dekker, M. Barbone, Z. Sun, C. Galiotis, A. N. Grigorenko, G. Konstantatos, A. Kis, M. Katsnelson, L. Vandersypen, A. Loiseau, V. Morandi, D. Neumaier, E. Treossi, V. Pellegrini, M. Polini, A. Tredicucci, G. M. Williams, B. Hee Hong, J.-H. Ahn, J. Min Kim, H. Zirath, B. J. van Wees, H. van der Zant, L. Occhipinti, A. Di Matteo, I. A. Kinloch, T. Seyller, E. Quesnel, X. Feng, K. Teo, N. Rupesinghe, P. Hakonen, S. R. T. Neil, Q. Tannock, T. Löfwander, and J. Kinaret. *Science and technology roadmap for graphene, related two-dimensional crystals, and hybrid systems.* Nanoscale **7**, 4598–4810 (2015).

[20] T.-H. Han, H. Kim, S.-J. Kwon, and T.-W. Lee. *Graphene-based flexible electronic devices.* Materials Science and Engineering: R: Reports **118**, 1–43 (2017).

[21] S. Bae, H. Kim, Y. Lee, X. Xu, J.-S. Park, Y. Zheng, J. Balakrishnan, T. Lei, H. Ri Kim, Y. I. Song, Y.-J. Kim, K. S. Kim, B. Özyilmaz, J.-H. Ahn, B. H. Hong, and S. Iijima. *Roll-to-roll production of 30-inch graphene films for transparent electrodes*. Nat. Nanotechnol. **5**, 574–578 (2010).

[22] N. Li, S. Oida, G. S. Tulevski, S.-J. Han, J. B. Hannon, D. K. Sadana, and T.-C. Chen. *Efficient and bright organic light-emitting diodes on single-layer graphene electrodes*. Nat Commun **4**, 2294 (2013).

[23] Y. Song, S. Chang, S. Gradecak, and J. Kong. *Visibly-Transparent Organic Solar Cells on Flexible Substrates with All-Graphene Electrodes*. Adv. Energy Mater. **6**, 1600847 (2016).

[24] A. T. N'Diaye, S. Bleikamp, P. J. Feibelman, and T. Michely. *Two-Dimensional Ir Cluster Lattice on a Graphene Moiré on Ir(111)*. Phys. Rev. Lett. **97**, 215501 (2006).

[25] S. Rusponi, M. Papagno, P. Moras, S. Vlaic, M. Etzkorn, P. M. Sheverdyaeva, D. Pacile, H. Brune, and C. Carbone. *Highly Anisotropic Dirac Cones in Epitaxial Graphene Modulated by an Island Superlattice*. Phys. Rev. Lett. **105**, 246803 (2010).

[26] D. F. Forster, T. O. Wehling, S. Schumacher, A. Rosch, and T. Michely. *Phase coexistence of clusters and islands: europium on graphene*. New J. Phys. **14**, 023022 (2012).

[27] D. Franz, N. Blanc, J. Coraux, G. Renaud, S. Runte, T. Gerber, C. Busse, T. Michely, P. J. Feibelman, U. Hejral, and A. Stierle. *Atomic structure of Pt nanoclusters supported by graphene/Ir(111) and reversible transformation under CO exposure*. Phys. Rev. B **93**, 045426 (2016).

[28] D. Mousadakos, M. Pivetta, H. Brune, and S. Rusponi. *Sm cluster superlattice on graphene/Ir(111)*. New. J. Phys. **19**, 123021 (2017).

[29] Q. Liao, H. J. Zhang, K. Wu, H. Y. Li, S. N. Bao, and P. He. *Nucleation and growth of monodispersed cobalt nanoclusters on graphene moire on Ru(0001)*. Nanotechnol. **22**, 125303 (2011).

[30] C. Carbone, S. Gardonio, P. Moras, S. Lounis, M. Heide, G. Bihlmayer, N. Atodiresei, P. H. Dederichs, S. Blügel, S. Vlaic, A. Lehnert, S. Ouazi, S. Rusponi, H. Brune, J. Honolka, A. Enders, K. Kern, S. Stepanow, C. Krull, T. Balashov, A. Mugarza, and P. Gambardella. *Self-Assembled Nanometer-Scale Magnetic Networks on Surfaces: Fundamental Interactions and Functional Properties*. Advanced Functional Materials **21**, 1212–1228 (2011).

[31] R. Baltic, F. Donati, A. Singha, C. Wäckerlin, J. Dreiser, B. Delley, M. Pivetta, S. Rusponi, and H. Brune. *Magnetic properties of single rare-earth atoms on graphene/Ir(111)*. Phys. Rev. B **98**, 024412 (2018).

Bibliography

[32] R. Baltic, M. Pivetta, F. Donati, C. Wäckerlin, A. Singha, J. Dreiser, S. Rusponi, and H. Brune. *Superlattice of Single Atom Magnets on Graphene.* Nano Lett. **16**, 7610–7615 (2016).

[33] M. Pivetta, S. Rusponi, and H. Brune. *Direct capture and electrostatic repulsion in the self-assembly of rare-earth atom superlattices on graphene.* Phys. Rev. B **98**, 115417 (2018).

[34] A. Nimbalkar and H. Kim. *Opportunities and Challenges in Twisted Bilayer Graphene: A Review.* Nanomicro Lett. **12**, 126 (2020).

[35] S. Lisi, X. Lu, T. Benschop, T. A. de Jong, P. Stepanov, J. R. Duran, F. Margot, I. Cucchi, E. Cappelli, A. Hunter, A. Tamai, V. Kandyba, A. Giampietri, A. Barinov, J. Jobst, V. Stalman, M. Leeuwenhoek, K. Watanabe, T. Taniguchi, L. Rademaker, S. J. van der Molen, M. P. Allan, D. K. Efetov, and F. Baumberger. *Observation of flat bands in twisted bilayer graphene.* Nat. Phys. **17**, 189–193 (2021).

[36] Y. Liu, N. O. Weiss, X. Duan, H.-C. Cheng, Y. Huang, and X. Duan. *Van der Waals heterostructures and devices.* Nat. Rev. Mat. **1**, 16042 (2016).

[37] A. K. Geim and I. V. Grigorieva. *Van der Waals heterostructures.* Nature **499**, 419–425 (2013).

[38] M. Yankowitz, Q. Ma, P. Jarillo-Herrero, and B. J. LeRoy. *van der Waals heterostructures combining graphene and hexagonal boron nitride.* Nat. Rev. Phys. **1**, 112–125 (2019).

[39] S. Carr, D. Massatt, S. Fang, P. Cazeaux, M. Luskin, and E. Kaxiras. *Twistronics: Manipulating the electronic properties of two-dimensional layered structures through their twist angle.* Phys. Rev. B **95**, 075420 (2017).

[40] Y. Cao, V. Fatemi, S. Fang, K. Watanabe, T. Taniguchi, E. Kaxiras, and P. Jarillo-Herrero. *Unconventional superconductivity in magic-angle graphene superlattices.* Nature **556**, 43–50 (2018).

[41] J. T. Robinson, S. W. Schmucker, C. B. Diaconescu, J. P. Long, J. C. Culbertson, T. Ohta, A. L. Friedman, and T. E. Beechem. *Electronic Hybridization of Large-Area Stacked Graphene Films.* ACS Nano **7**, 637–644 (2013).

[42] X.-D. Chen, W. Xin, W.-S. Jiang, Z.-B. Liu, Y. Chen, and J.-G. Tian. *High-Precision Twist-Controlled Bilayer and Trilayer Graphene.* Adv. Mater. **28**, 2563–2570 (2016).

[43] B. Wang, M. Huang, N. Y. Kim, B. V. Cunning, Y. Huang, D. Qu, X. Chen, S. Jin, M. Biswal, X. Zhang, S. H. Lee, H. Lim, W. J. Yoo, Z. Lee, and R. S. Ruoff. *Controlled Folding of Single Crystal Graphene.* Nano Lett. **17**, 1467–1473 (2017).

[44] N. Weiss, T. Cren, M. Epple, S. Rusponi, G. Baudot, S. Rohart, A. Tejeda, V. Repain, S. Rousset, P. Ohresser, F. Scheurer, P. Bencok, and H. Brune. *Uniform Magnetic Properties for an Ultrahigh-Density Lattice of Noninteracting Co Nanostructures.* Phys. Rev. Lett. **95**, 157204 (2005).

[45] A. Lehnert, P. Buluschek, N. Weiss, J. Giesecke, M. Treier, S. Rusponi, and H. Brune. *High resolution in situ magneto-optic Kerr effect and scanning tunneling microscopy setup with all optical components in UHV.* Rev. Sci. Instrum. **80**, 023902 (2009).

[46] S. Vlaic. *Magnetism and Atomic Scale Structure of Bimetallic Nanostructures at Surfaces.* Ph.D. thesis, Ecole Polytechnique de Lausanne (2013).

[47] O. Fruchart, M. Klaua, J. Barthel, and J. Kirschner. *Self-Organized Growth of Nanosized Vertical Magnetic Co Pillars on Au(111).* Phys. Rev. Lett. **83**, 2769–2772 (1999).

[48] A. Cavallin. *Growth and Magnetism of Nanostructures Investigated by STM, MOKE, and XMCD.* Ph.D. thesis, Ecole Polytechnique de Lausanne (2013).

[49] J. Kang, D. Shin, S. Bae, and B. H. Hong. *Graphene transfer: key for applications.* Nanoscale **4**, 5527–5537 (2012).

[50] J. W. Suk, A. Kitt, C. W. Magnuson, Y. Hao, S. Ahmed, J. An, A. K. Swan, B. B. Goldberg, and R. S. Ruoff. *Transfer of CVD-Grown Monolayer Graphene onto Arbitrary Substrates.* ACS Nano **5**, 6916–6924 (2011).

[51] M. Her, R. Beams, and L. Novotny. *Graphene transfer with reduced residue.* Phys. Lett. A **377**, 1455 – 1458 (2013).

[52] L. Gao, W. Ren, H. Xu, L. Jin, Z. Wang, T. Ma, L.-P. Ma, Z. Zhang, Q. Fu, L.-M. Peng, X. Bao, and H.-M. Chenga. *Repeated growth and bubbling transfer of graphene with millimetre-size single-crystal grains using platinum.* Nat. Commun. **3**, 699 (2012).

[53] M. Gao, Y. Pan, L. Huang, H. Hu, L. Z. Zhang, H. M. Guo, S. X. Du, and H.-J. Gao. *Epitaxial growth and structural property of graphene on Pt(111).* Appl. Phys. Lett. **98**, 033101 (2011).

[54] S. Y. Yang, J. G. Oh, D. Y. Jung, H. Choi, C. H. Yu, J. Shin, C.-G. Choi, B. J. Cho, and S.-Y. Choi. *Metal-Etching-Free Direct Delamination and Transfer of Single-Layer Graphene with a High Degree of Freedom.* Small **11**, 175–181 (2015).

[55] Z. Xu, X. Li, B. I. Yakobson, and F. Ding. *Interaction between graphene layers and the mechanisms of graphite's superlubricity and self-retraction.* Nanoscale **5**, 6736–6741 (2013).

Bibliography

[56] J. Y. Howe, C. J. Rawn, L. E. Jones, and H. Ow. *Improved crystallographic data for graphite.* Powder Diffr. **18**, 150–154 (2003).

[57] J. P. Lu. *Elastic Properties of Carbon Nanotubes and Nanoropes.* Phys. Rev. Lett. **79**, 1297–1300 (1997).

[58] M. Hasegawa and K. Nishidate. *Semiempirical approach to the energetics of interlayer binding in graphite.* Phys. Rev. B **70**, 205431 (2004).

[59] X. Chen, F. Tian, C. Persson, W. Duan, and N.-x. Chen. *Interlayer interactions in graphites.* Sci. Rep. **3**, 3046 (2013).

[60] O. Yazyev. *Serie No.1 Physique du solide, Ecole Polytechnique Federale de Lausanne* (2000).

[61] C. Guo, J. Zhang, W. Xu, K. Liu, X. Yuan, S. Qin, and Z. Zhu. *Graphene-Based Perfect Absorption Structures in the Visible to Terahertz Band and Their Optoelectronics Applications.* Nanomat. **8**, 1033 (2018).

[62] A. H. Castro Neto, F. Guinea, N. M. R. Peres, K. S. Novoselov, and A. K. Geim. *The electronic properties of graphene.* Rev. Mod. Phys. **81**, 109–162 (2009).

[63] M. Lazzeri, C. Attaccalite, L. Wirtz, and F. Mauri. *Impact of the electron-electron correlation on phonon dispersion: Failure of LDA and GGA DFT functionals in graphene and graphite.* Phys. Rev. B **78**, 081406 (2008).

[64] L. A. Falkovsky. *Phonon dispersion in graphene.* J. Exp. Theor. Phys. **105**, 397–403 (2007).

[65] M. Dresselhaus, A. Jorio, and R. Saito. *Characterizing Graphene, Graphite, and Carbon Nanotubes by Raman Spectroscopy.* Annu. Rev. Condens. Matter Phys. **1**, 89–108 (2010).

[66] F. Banhart, J. Kotakoski, and A. V. Krasheninnikov. *Structural Defects in Graphene.* ACS Nano **5**, 26–41 (2011).

[67] L. Liu, M. Qing, Y. Wang, and S. Chen. *Defects in Graphene: Generation, Healing, and Their Effects on the Properties of Graphene: A Review.* J. Mater. Sci. Technol. **31**, 599 – 606 (2015).

[68] W. Tian, W. Li, W. Yu, and X. Liu. *A Review on Lattice Defects in Graphene: Types, Generation, Effects and Regulation.* Micromachines **8**, 163 (2017).

[69] J. Ma, D. Alfè, A. Michaelides, and E. Wang. *Stone-Wales defects in graphene and other planar sp^2-bonded materials.* Phys. Rev. B **80**, 033407 (2009).

[70] X.-Y. Wang, A. Narita, and K. Müllen. *Precision synthesis versus bulk-scale fabrication of graphenes.* Nat. Rev. Chem. **2**, 0100 (2018).

[71] Y. Xu, H. Cao, Y. Xue, B. Li, and W.-H. Cai. *Liquid-Phase Exfoliation of Graphene: An Overview on Exfoliation Media, Techniques, and Challenges.* Nanomaterials **8**, 942 (2018).

[72] M. Eizenberg and J. Blakely. *Carbon monolayer phase condensation on Ni(111).* Surf. Sci. **82**, 228–236 (1979).

[73] J. Sun, Y. Nam, N. Lindvall, M. T. Cole, K. B. K. Teo, Y. Woo Park, and A. Yurgens. *Growth mechanism of graphene on platinum: Surface catalysis and carbon segregation.* Appl. Phys. Lett. **104**, 152107 (2014).

[74] M. S. Fuhrer. *Carbon impurities on graphene synthesized by chemical vapor deposition on platinum.* J. Appl. Phys. **116**, 044303 (2014).

[75] P. Yi, S. Dong-Xia, and G. Hong-Jun. *Formation of graphene on Ru(0001) surface.* Chinese Physics **16**, 3151–3153 (2007).

[76] A. L. Vázquez de Parga, F. Calleja, B. Borca, M. C. G. Passeggi, J. J. Hinarejos, F. Guinea, and R. Miranda. *Periodically Rippled Graphene: Growth and Spatially Resolved Electronic Structure.* Phys. Rev. Lett. **100**, 056807 (2008).

[77] K. F. McCarty, P. J. Feibelman, E. Loginova, and N. C. Bartelt. *Kinetics and thermodynamics of carbon segregation and graphene growth on Ru(0001).* Carbon **47**, 1806–1813 (2009).

[78] W. Norimatsu and M. Kusunoki. *Epitaxial graphene on SiC{0001}: advances and perspectives.* Phys. Chem. Chem. Phys. **16**, 3501 (2014).

[79] Q. Yu, J. Lian, S. Siriponglert, H. Li, Y. P. Chen, and S.-S. Pei. *Graphene segregated on Ni surfaces and transferred to insulators.* Appl. Phys. Lett. **93**, 113103 (2008).

[80] K. V. Emtsev, A. Bostwick, K. Horn, J. Jobst, G. L. Kellogg, L. Ley, J. L. McChesney, T. Ohta, S. A. Reshanov, J. Röhrl, E. Rotenberg, A. K. Schmid, D. Waldmann, H. B. Weber, and T. Seyller. *Towards wafer-size graphene layers by atmospheric pressure graphitization of silicon carbide.* Nat. Mater. **8**, 203–207 (2009).

[81] N. Mishra, J. Boeckl, N. Motta, and F. Iacopi. *Graphene growth on silicon carbide: A review.* Phys. Status Solidi A **213**, 2277–2289 (2016).

[82] C. Wang, K. Vinodgopal, and G.-P. Dai. *Large-Area Synthesis and Growth Mechanism of Graphene by Chemical Vapor Deposition.* In P. Mandracci, editor, *Chemical Vapor Deposition for Nanotechnology*, chap. 5. IntechOpen, Rijeka (2019).

[83] S. Bae, H. Kim, Y. Lee, X. Xu, J.-S. Park, Y. Zheng, J. Balakrishnan, T. Lei, H. Ri Kim, Y. I. Song, Y.-J. Kim, K. S. Kim, B. Özyilmaz, J.-H. Ahn, B. H. Hong, and S. Iijima. *Roll-to-roll production of 30-inch graphene films for transparent electrodes.* Nat. Nanotechnol. **5**, 574–578 (2010).

Bibliography

[84] X. Xu, Z. Zhang, J. Dong, D. Yi, J. Niu, M. Wu, L. Lin, R. Yin, M. Li, J. Zhou, S. Wang, J. Sun, X. Duan, P. Gao, Y. Jiang, X. Wu, H. Peng, R. S. Ruoff, Z. Liu, D. Yu, E. Wang, F. Ding, and K. Liu. *Ultrafast epitaxial growth of metre-sized single-crystal graphene on industrial Cu foil.* Sci. Bull. **62**, 1074–1080 (2017).

[85] J. Park, W. C. Mitchel, L. Grazulis, H. E. Smith, K. G. Eyink, J. J. Boeckl, D. H. Tomich, S. D. Pacley, and J. E. Hoelscher. *Epitaxial Graphene Growth by Carbon Molecular Beam Epitaxy (CMBE).* Adv. Mat. **22**, 4140–4145 (2010).

[86] B. Kiraly, E. V. Iski, A. J. Mannix, B. L. Fisher, M. C. Hersam, and N. P. Guisinger. *Solid-source growth and atomic-scale characterization of graphene on Ag(111).* Nat. Comm. **4**, 2804 (2013).

[87] I. Hernández-Rodríguez, J. M. García, J. A. Martín-Gago, P. L. de Andrés, and J. Méndez. *Graphene growth on Pt(111) and Au(111) using a MBE carbon solid-source.* Diam. Relat. Mater. **57**, 58–62 (2015). 25th International Conference on Diamond and Carbon Materials – DCM 2014.

[88] C. Herbig, T. Knispel, S. Simon, U. A. Schröder, A. J. Martínez-Galera, M. A. Arman, C. Teichert, J. Knudsen, A. V. Krasheninnikov, and T. Michely. *From Permeation to Cluster Arrays: Graphene on Ir(111) Exposed to Carbon Vapor.* Nano Lett. **17**, 3105–3112 (2017).

[89] W. Choi, I. Lahiri, R. Seelaboyina, and Y. S. Kang. *Synthesis of Graphene and Its Applications: A Review.* Crit. Rev. Solid State Mater. Sci. **35**, 52–71 (2010).

[90] K. A. Madurani, S. Suprapto, N. I. Machrita, S. L. Bahar, W. Illiya, and F. Kurniawan. *Progress in Graphene Synthesis and its Application: History, Challenge and the Future Outlook for Research and Industry.* ECS J. Solid State Sci. Technol. **9**, 093013 (2020).

[91] B. Aïssa, N. K. Memon, A. Ali, and M. K. Khraisheh. *Recent Progress in the Growth and Applications of Graphene as a Smart Material: A Review.* Front. Mater. **2** (2015).

[92] Y. Song, W. Zou, Q. Lu, L. Lin, and Z. Liu. *Graphene Transfer: Paving the Road for Applications of Chemical Vapor Deposition Graphene.* Small p.2007600 (2021).

[93] T. Hallam, C. F. Moldovan, K. Gajewski, A. M. Ionescu, and G. S. Duesberg. *Large area suspended graphene for nano-mechanical devices: Large area suspended graphene for nano-mechanical devices.* Phys. Status Solidi B **252**, 2429–2432 (2015).

[94] R. Li, Z. Li, E. Pambou, P. Gutfreund, T. A. Waigh, J. R. P. Webster, and J. R. Lu. *Determination of PMMA Residues on a Chemical-Vapor-Deposited Monolayer of Graphene by Neutron Reflection and Atomic Force Microscopy.* Langmuir **34**, 1827–1833 (2018).

[95] J. W. Suk, W. H. Lee, J. Lee, H. Chou, R. D. Piner, Y. Hao, D. Akinwande, and R. S. Ruoff. *Enhancement of the Electrical Properties of Graphene Grown by Chemical Vapor Deposition via Controlling the Effects of Polymer Residue.* Nano Lett. **13**, 1462–1467 (2013).

[96] P. Pham. *Cleaning of graphene surfaces by low-pressure air plasma.* R. Soc. Open Sci. **5** (2018).

[97] E. Mercado, J. Anaya, and M. Kuball. *Impact of Polymer Residue Level on the In-Plane Thermal Conductivity of Suspended Large-Area Graphene Sheets.* ACS Appl. Mater. Interfaces pp.17910–17919 (2021).

[98] M. Chen, R. C. Haddon, R. Yan, and E. Bekyarova. *Advances in transferring chemical vapour deposition graphene: a review.* Mater. Horiz. **4**, 1054–1063 (2017).

[99] L.-P. Ma, W. Ren, and H.-M. Cheng. *Transfer Methods of Graphene from Metal Substrates: A Review.* Small Methods **3**, 1900049 (2019).

[100] G. Lupina, J. Kitzmann, I. Costina, M. Lukosius, C. Wenger, A. Wolff, S. Vaziri, M. Östling, I. Pasternak, A. Krajewska, W. Strupinski, S. Kataria, A. Gahoi, M. C. Lemme, G. Ruhl, G. Zoth, O. Luxenhofer, and W. Mehr. *Residual Metallic Contamination of Transferred Chemical Vapor Deposited Graphene.* ACS Nano **9**, 4776–4785 (2015).

[101] A. Ambrosi and M. Pumera. *The CVD graphene transfer procedure introduces metallic impurities which alter the graphene electrochemical properties.* Nanoscale **6**, 472–476 (2014).

[102] H.-K. Choi, J.-Y. Kim, H. Y. Jeong, C.-G. Choi, and S.-Y. Choi. *Characterization of chemical vapor deposition-grown graphene films with various etchants.* Carbon Lett. **13** (2012).

[103] H. Al-Mumen, F. Rao, W. Li, and L. Dong. *Singular Sheet Etching of Graphene with Oxygen Plasma.* Nano-Micro Lett. **6**, 116–124 (2014).

[104] J. D. Caldwell, T. J. Anderson, J. C. Culbertson, G. G. Jernigan, K. D. Hobart, F. J. Kub, M. J. Tadjer, J. L. Tedesco, J. K. Hite, M. A. Mastro, R. L. Myers-Ward, C. R. Eddy, P. M. Campbell, and D. K. Gaskill. *Technique for the Dry Transfer of Epitaxial Graphene onto Arbitrary Substrates.* ACS Nano **4**, 1108–1114 (2010).

[105] E. Auchter, J. Marquez, S. L. Yarbro, and E. Dervishi. *A facile alternative technique for large-area graphene transfer via sacrificial polymer.* AIP Adv. **7**, 125306 (2017).

[106] Y. Wang, Y. Zheng, X. Xu, E. Dubuisson, Q. Bao, J. Lu, and K. P. Loh. *Electrochemical Delamination of CVD-Grown Graphene Film: Toward the Recyclable Use of Copper Catalyst.* ACS Nano **5**, 9927–9933 (2011).

[107] C. J. L. de la Rosa, N. Lindvall, M. T. Cole, Y. Nam, M. Löffler, E. Olsson, and A. Yurgens. *Frame assisted H_2O electrolysis induced H_2 bubbling transfer of large area graphene grown by chemical vapor deposition on Cu.* Appl. Phys. Lett. **102**, 022101 (2013).

[108] M. G. Hell, Y. Falke, A. Bliesener, N. Ehlen, B. V. Senkovskiy, T. Szkopek, and A. Grüneis. *Combined Ultra High Vacuum Raman and Electronic Transport Characterization of Large-Area Graphene on SiO_2.* Phys. Status Solidi B **255**, 1800456 (2018).

[109] J. Sun, X. Fan, W. Guo, L. Liu, X. Liu, J. Deng, and C. Xu. *Mechanism of Electrochemical Delamination of Two-Dimensional Materials from Their Native Substrates by Bubbling.* Sensors **15**, 31811–31820 (2015).

[110] H. V. Ngoc, Y. Qian, S. K. Han, and D. J. Kang. *PMMA-Etching-Free Transfer of Wafer-scale Chemical Vapor Deposition Two-dimensional Atomic Crystal by a Water Soluble Polyvinyl Alcohol Polymer Method.* Sci. Rep. **6**, 33096 (2016).

[111] P. J. Ko, H. Takahashi, S. Koide, H. Sakai, T. V. Thu, H. Okada, and A. Sandhu. *Simple method to transfer graphene from metallic catalytic substrates to flexible surfaces without chemical etching.* J. Phys. Conf. Ser. **433**, 012002 (2013).

[112] S. Nie, W. Wu, S. Xing, Q. Yu, J. Bao, S.-s. Pei, and K. F. McCarty. *Growth from below: bilayer graphene on copper by chemical vapor deposition.* New J. Phys. **14**, 093028 (2012).

[113] S. Simon, E. Voloshina, J. Tesch, F. Förschner, V. Enenkel, C. Herbig, T. Knispel, A. Tries, J. Kröger, Y. Dedkov, and M. Fonin. *Layer-by-Layer Decoupling of Twisted Graphene Sheets Epitaxially Grown on a Metal Substrate.* Small **14**, 1703701 (2018).

[114] C. F. P. Kastorp, D. A. Duncan, M. Scheffler, J. D. Thrower, A. L. Jørgensen, H. Hussain, T.-L. Lee, L. Hornekær, and R. Balog. *Growth and electronic properties of bi- and trilayer graphene on Ir(111).* Nanoscale **12**, 19776–19786 (2020).

[115] W. Yao, E. Wang, C. Bao, Y. Zhang, K. Zhang, K. Bao, C. Chan, C. Chen, J. Ávila, M. Asensio, J. Zhu, and S. Zhou. *Quasicrystalline 30° Twisted Bilayer Graphene as an Incommensurate Superlattice with Strong Interlayer Coupling.* Proc. Natl. Acad. Sci. U.S.A **115** (2018).

[116] Y. Huang, X. Li, H. Cui, and Z. Zhou. *Bi-layer Graphene: Structure, Properties, Preparation and Prospects.* CGS **2**, 97–105 (2019).

[117] M. Papagno, D. Pacilé, D. Topwal, P. Moras, P. M. Sheverdyaeva, F. D. Natterer, A. Lehnert, S. Rusponi, Q. Dubout, F. Calleja, E. Frantzeskakis, S. Pons, J. Fujii, I. Vobornik, M. Grioni, C. Carbone, and H. Brune. *Two Distinct Phases of Bilayer Graphene Films on Ru(0001).* ACS Nano **6**, 9299–9304 (2012).

[118] Q. Dubout, F. Calleja, G. Sclauzero, M. Etzkorn, A. Lehnert, L. Claude, M. Papagno, F. D. Natterer, F. Patthey, S. Rusponi, A. Pasquarello, and H. Brune. *Giant apparent lattice distortions in STM images of corrugated sp2-hybridised monolayers.* New J. Phys. **18**, 103027 (2016).

[119] W. Fang, A. L. Hsu, Y. Song, and J. Kong. *A review of large-area bilayer graphene synthesis by chemical vapor deposition.* Nanoscale **7**, 20335–20351 (2015).

[120] L. Liu, H. Zhou, R. Cheng, W. J. Yu, Y. Liu, Y. Chen, J. Shaw, X. Zhong, Y. Huang, and X. Duan. *High Yield Chemical Vapor Deposition Growth of High Quality Large-Area AB Stacked Bilayer Graphene.* ACS nano **6**, 8241–8249 (2012).

[121] J. Hass, F. Varchon, J. E. Millán-Otoya, M. Sprinkle, N. Sharma, W. A. de Heer, C. Berger, P. N. First, L. Magaud, and E. H. Conrad. *Why Multilayer Graphene on* $4H-\mathrm{SiC}(000\bar{1})$ *Behaves Like a Single Sheet of Graphene.* Phys. Rev. Lett. **100**, 125504 (2008).

[122] K. Kim, M. Yankowitz, B. Fallahazad, S. Kang, H. C. P. Movva, S. Huang, S. Larentis, C. M. Corbet, T. Taniguchi, K. Watanabe, S. K. Banerjee, B. J. LeRoy, and E. Tutuc. *van der Waals Heterostructures with High Accuracy Rotational Alignment.* Nano Lett. **16**, 1989–1995 (2016).

[123] K. Kim, A. DaSilva, S. Huang, B. Fallahazad, S. Larentis, T. Taniguchi, K. Watanabe, B. J. LeRoy, A. H. MacDonald, and E. Tutuc. *Tunable moiré bands and strong correlations in small-twist-angle bilayer graphene.* Proc. Natl. Acad. Sci. **114**, 3364–3369 (2017).

[124] V. Carozo, C. M. Almeida, E. H. M. Ferreira, L. G. Cançado, C. A. Achete, and A. Jorio. *Raman Signature of Graphene Superlattices.* Nano Lett. **11**, 4527–4534 (2011).

[125] C. Vo-Van, A. Kimouche, A. Reserbat-Plantey, O. Fruchart, P. Bayle-Guillemaud, N. Bendiab, and J. Coraux. *Epitaxial graphene prepared by chemical vapor deposition on single crystal thin iridium films on sapphire.* Appl. Phys. Lett. **98**, 181903 (2011).

[126] *Renishaw inVia confocal Raman microscope.* https://www.renishaw.com/en/invia-confocal-raman-microscope--6260 .

[127] F. Adar. *Depth Resolution of the Raman Microscope: Optical Limitations and Sample Characteristics.* Spectroscopy **25**, 16–23 (2010).

[128] *TED PELLA INC.* https://www.tedpella.com .

[129] A. C. Ferrari and D. M. Basko. *Raman spectroscopy as a versatile tool for studying the properties of graphene.* Nat. Nanotech. **8**, 235 (2013).

115

Bibliography

[130] A. C. Ferrari, J. C. Meyer, V. Scardaci, C. Casiraghi, M. Lazzeri, F. Mauri, S. Piscanec, D. Jiang, K. S. Novoselov, S. Roth, and A. K. Geim. *The Raman Fingerprint of Graphene.* Phys. Rev. Lett. **97** (2006).

[131] R. Beams, L. Gustavo Cançado, and L. Novotny. *Raman characterization of defects and dopants in graphene.* J. Phys. Condens. Matter. **27**, 083002 (2015).

[132] Y. Y. Wang, Z. H. Ni, Z. X. Shen, H. M. Wang, and Y. H. Wu. *Interference enhancement of Raman signal of graphene.* Appl. Phys. Lett. **92**, 043121 (2008).

[133] Y. Hao, Y. Wang, L. Wang, Z. Ni, Z. Wang, R. Wang, C. K. Koo, Z. Shen, and J. T. L. Thong. *Probing Layer Number and Stacking Order of Few-Layer Graphene by Raman Spectroscopy.* Small **6**, 195–200 (2010).

[134] A. Das, B. Chakraborty, and A. K. Sood. *Raman spectroscopy of graphene on different substrates and influence of defects.* Bull. Mater. Sci. **31**, 579–584 (2008).

[135] I. Calizo, W. Bao, F. Miao, J. Lau, and A. Balandin. *The effect of substrates on the Raman spectrum of graphene: Graphene on-sapphire and graphene-on-glass.* Appl. Phys. Lett. **91** (2007).

[136] Z. L. Xiao, C. Li, D. Li, J. Yang, X. Zeng, and W. Yuan. *Preparation of Single- and Few-Layer Graphene Sheets Using Co Deposition on SiC Substrate.* J. Nanomater. **2011**, 319624 (2011).

[137] A. Jorio, E. H. M. Ferreira, M. V. O. Moutinho, F. Stavale, C. A. Achete, and R. B. Capaz. *Measuring disorder in graphene with the G and D bands.* Phys. Status Solidi B **247**, 2980–2982 (2010).

[138] F. Tuinstra and J. L. Koenig. *Raman Spectrum of Graphite.* J. Chem. Phys. **53**, 1126–1130 (1970).

[139] A. Eckmann, A. Felten, A. Mishchenko, L. Britnell, R. Krupke, K. S. Novoselov, and C. Casiraghi. *Probing the Nature of Defects in Graphene by Raman Spectroscopy.* Nano Lett. **12**, 3925–3930 (2012).

[140] Y. Kawashima and G. Katagiri. *Fundamentals, overtones, and combinations in the Raman spectrum of graphite.* Phys. Rev. B Condens. Matter **52**, 10053–10059 (1995).

[141] J. Yano and V. K. Yachandra. *X-ray absorption spectroscopy.* Photosynth. Res **102**, 241 (2009).

[142] G. v. d. Laan. *Applications of soft x-ray magnetic dichroism.* J. Phys.: Conf. Ser. **430**, 012127 (2013).

[143] C. Piamonteze, U. Flechsig, S. Rusponi, J. Dreiser, J. Heidler, M. Schmidt, R. Wetter, M. Calvi, T. Schmidt, H. Pruchova Blaettler, J. Krempaský, C. Quitmann, H. Brune, and F. Nolting. *X-Treme beamline at SLS: X-ray magnetic circular and linear dichroism at high field and low temperature.* J. Synchrotron Radiat. **19**, 661–74 (2012).

[144] H. Uchikawa. *20 - Specialized Techniques.* In V. Ramachandran and J. J. Beaudoin, editors, *Handbook of Analytical Techniques in Concrete Science and Technology*, pp.820 – 934. William Andrew Publishing, Norwich, NY (2001).

[145] Y. Dahman. *Chapter 2 - Generic Methodologies for Characterization**By Yaser Dahman, Caroline Halim, Oswaldo Matos, and Louisa Chan.* In Y. Dahman, editor, *Nanotechnology and Functional Materials for Engineers*, Micro and Nano Technologies, pp.19 – 45. Elsevier (2017).

[146] S. Andrieu and P. Müller. *les surfaces solides: concepts et méthodes.* CNRS editions (2005).

[147] R. P. Gunawardane and C. R. Arumainayagam. *AUGER ELECTRON SPECTROSCOPY*, pp.451–483. Springer US, Boston, MA (2006).

[148] M. P. Seah and W. A. Dench. *Quantitative electron spectroscopy of surfaces: A standard data base for electron inelastic mean free paths in solids.* Surf. Interface Anal. **1**, 2–11 (1979).

[149] L. E. Davis, N. C. MacDonald, P. W. Palmberg, G. E. Riach, and R. E. Weber. *Handbook of Auger Electron Spectroscopy.* Physical Electronics Division, Perkin-Elmer Corporation (1976).

[150] R. Nyholm, K. Helenelund, B. Johansson, and S.-E. Hörnström. *Transition from bandlike to quasiatomic behavior in the $N_6,7O_4,5O_4,5$ Auger spectra of iridium, platinum, and gold.* Phys. Rev. B **34**, 675–679 (1986).

[151] B. Lesiak, P. Mrozek, A. Jabloński, and A. Jóźwik. *Analysis of the Auger KLL spectra of carbon by the pattern recognition method.* Surf. Interface Anal. **8**, 121–126 (1986).

[152] C. Powell, N. Erickson, and T. Madey. *Results of a joint auger/esca round robin sponsored by astm committee E-42 on surface analysis. Part II. Auger results.* J. Electron Spectros. Relat. Phenomena **25**, 87–118 (1982).

[153] G. Binnig, H. Rohrer, C. Gerber, and E. Weibel. *Tunneling through a controllable vacuum gap.* Appl. Phys. Lett. **40**, 178–180 (1982).

[154] N. Weiss. *Propriétés magnétiques de nanostructures de cobalt adsorbées.* Ph.D. thesis, Ecole Polytechnique de Lausanne (2004).

[155] P. Buluschek. *Submonolayer growth of cobalt on metallic and insulating surfaces studied by scanning tunneling microscopy and kinetic Monte-Carlo simulations.* Ph.D. thesis, Ecole Polytechnique de Lausanne (2007).

[156] T. Hagedorn, M. E. Ouali, W. Paul, D. Oliver, Y. Miyahara, and P. Grütter. *Refined tip preparation by electrochemical etching and ultrahigh vacuum treatment to obtain atomically sharp tips for scanning tunneling microscope and atomic force microscope.* Rev. Sci. Instrum. **82**, 113903 (2011).

[157] J. Tersoff and D. R. Hamann. *Theory of the scanning tunneling microscope.* Phys. Rev. B **31**, 805–813 (1985).

[158] J. Bardeen. *Tunnelling from a Many-Particle Point of View.* Phys. Rev. Lett. **6**, 57–59 (1961).

[159] D. Mousadakos. *Rare Earth and Bimetallic Transition Metal Islands at Surfaces.* Ph.D. thesis, Ecole Polytechnique de Lausanne (2017).

[160] *Surface preparation laboratory.* https://www.spl.eu .

[161] *Dow SYLGARD 184 Silicone Elastomer Kit.* https://www.dow.com/en-us/pdp.sylgard-184-silicone-elastomer-kit.01064291z.html .

[162] *DOWSIL 744 RTV Adhesive Sealant.* https://www.dow.com/en-us/pdp.dowsil-744-rtv-adhesive-sealant.03321916h.html .

[163] W. Zhang, P. Wu, Z. Li, and J. Yang. *First-Principles Thermodynamics of Graphene Growth on Cu Surfaces.* J. Phys. Chem. C **115**, 17782–17787 (2011).

[164] R. M. Jacobberger and M. S. Arnold. *Graphene Growth Dynamics on Epitaxial Copper Thin Films.* Chem. Mater. **25**, 871–877 (2013).

[165] M. Losurdo, M. M. Giangregorio, P. Capezzuto, and G. Bruno. *Graphene CVD growth on copper and nickel: role of hydrogen in kinetics and structure.* Phys. Chem. Chem. Phys. **13**, 20836–20843 (2011).

[166] Y. Bleu, F. Bourquard, A.-S. Loir, V. Barnier, F. Garrelie, and C. Donnet. *Raman study of the substrate influence on graphene synthesis using a solid carbon source via rapid thermal annealing.* J. Raman Spectrosc. **50**, 1630–1641 (2019).

[167] A. T. N'Diaye, J. Coraux, T. N. Plasa, C. Busse, and T. Michely. *Structure of epitaxial graphene on Ir(111).* New J. Phys. **10**, 043033 (2008).

[168] M. Shimbo, K. Furukawa, K. Fukuda, and K. Tanzawa. *Silicon-to-silicon direct bonding method.* J. Appl. Phys. **60**, 2987 (1986).

[169] J. B. Lasky. *Wafer bonding for silicon-on-insulator technologies.* Appl. Phys. Lett. **48**, 78 (1986).

[170] W. P. Maszara, G. Goetz, A. Caviglia, and J. B. McKitterick. *Bonding of silicon wafers for silicon-on-insulator.* J. Appl. Phys. **64**, 4943 (1988).

[171] U. Gösele and Q.-Y. Tong. *Semiconductor wafer bonding.* Annu. Rev. Mater. Sci. **28**, 215–241 (1998).

[172] M. Alexe and U. Gösele. *Wafer Bonding: Applications and Technology.* Springer Berlin Heidelberg, Berlin, Heidelberg (2004).

[173] D. Jariwala, T. J. Marks, and M. C. Hersam. *Mixed-dimensional van der Waals heterostructures.* Nat. Mater. **16**, 170–181 (2017).

[174] S. Das, D. Lahiri, D.-Y. Lee, A. Agarwal, and W. Choi. *Measurements of the adhesion energy of graphene to metallic substrates.* Carbon **59**, 121–129 (2013).

[175] J. Schwan, S. Ulrich, V. Batori, H. Ehrhardt, and S. R. P. Silva. *Raman spectroscopy on amorphous carbon films.* J. Appl. Phys. **80**, 440–447 (1996).

[176] M. Marton, M. Vojs, E. Zdravecká, M. Himmerlich, T. Haensel, S. Krischok, M. Kotlár, P. Michniak, M. Veselý, and R. Redhammer. *Raman Spectroscopy of Amorphous Carbon Prepared by Pulsed Arc Discharge in Various Gas Mixtures.* J Spectrosc. **2013**, 1–6 (2013).

[177] I. Vlassiouk, M. Regmi, P. Fulvio, S. Dai, P. Datskos, G. Eres, and S. Smirnov. *Role of Hydrogen in Chemical Vapor Deposition Growth of Large Single-Crystal Graphene.* ACS Nano **5**, 6069–6076 (2011).

[178] Q. Liu, Y. Gong, J. S. Wilt, R. Sakidja, and J. Wu. *Synchronous growth of AB-stacked bilayer graphene on Cu by simply controlling hydrogen pressure in CVD process.* Carbon **93**, 199–206 (2015).

[179] M. Chen, D. Stekovic, W. Li, B. Arkook, R. C. Haddon, and E. Bekyarova. *Sublimation-assisted graphene transfer technique based on small polyaromatic hydrocarbons.* Nanotechnology **28**, 255701 (2017).

[180] Y.-H. Deng. *Transfer of graphene onto arbitrary substrates via sublimable carrier* (2020). ArXiv: 2010.11534.

[181] *Sigma-Aldrich Naphthalene.* https://www.sigmaaldrich.com/CH/en/product/aldrich/147141 .

[182] A. Shivayogimath, P. R. Whelan, D. M. Mackenzie, B. Luo, D. Huang, D. Luo, M. Wang, L. Gammelgaard, H. Shi, R. S. Ruoff, P. Bøggild, and T. J. Booth. *Do-It-Yourself Transfer of Large-Area Graphene Using an Office Laminator and Water.* Chem. Mater. **31**, 2328–2336 (2019).

[183] *Sigma-Aldrich Poly(vinyl alcohol).* https://www.sigmaaldrich.com/CH/en/product/aldrich/341584 .

Bibliography

[184] Q. Li, J. Lu, P. Gupta, and M. Qiu. *Engineering Optical Absorption in Graphene and Other 2D Materials: Advances and Applications.* Adv. Opt. Mater **7**, 1900595 (2019).

[185] A. Das, S. Pisana, B. Chakraborty, S. Piscanec, S. K. Saha, U. V. Waghmare, K. S. Novoselov, H. R. Krishnamurthy, A. K. Geim, A. C. Ferrari, and A. K. Sood. *Monitoring dopants by Raman scattering in an electrochemically top-gated graphene transistor.* Nature Nanotech **3**, 210–215 (2008).

[186] P. Poncharal, A. Ayari, T. Michel, and J.-L. Sauvajol. *Raman spectra of misoriented bilayer graphene.* Phys. Rev. B **78**, 113407 (2008).

[187] I. Y. Prosanov and A. A. Matvienko. *Study of PVA thermal destruction by means of IR and Raman spectroscopy.* Phys. Solid State **52**, 2203–2206 (2010).

[188] A. Dahal and M. Batzill. *Graphene nickel interfaces: a review.* Nanoscale **6**, 2548–2562 (2014).

[189] *Graphenesic.* https://graphensic.com .

[190] X. Shan, Q. Wang, X. Bian, W.-q. Li, G.-h. Chen, and H. Zhu. *Graphene layers on Si-face and C-face surfaces and interaction with Si and C atoms in layer controlled graphene growth on SiC substrates.* RSC Adv. **5**, 78625–78633 (2015).

[191] F. m. c. Varchon, P. Mallet, L. Magaud, and J.-Y. Veuillen. *Rotational disorder in few-layer graphene films on* $6H-\text{SiC}(000-1)$*: A scanning tunneling microscopy study.* Phys. Rev. B **77**, 165415 (2008).

[192] M. K. Alam, C. Niu, Y. Wang, W. Wang, Y. Li, C. Dai, T. Tong, X. Shan, E. Charlson, S. Pei, X.-T. Kong, Y. Hu, A. Belyanin, G. Stein, Z. Liu, J. Hu, Z. Wang, and J. Bao. *Large graphene-induced shift of surface-plasmon resonances of gold films: Effective-medium theory for atomically thin materials.* Phys. Rev. Research **2**, 013008 (2020).

[193] E. N. Voloshina, E. Fertitta, A. Garhofer, F. Mittendorfer, M. Fonin, A. Thissen, and Y. S. Dedkov. *Electronic structure and imaging contrast of graphene moiré on metals.* Sci. Rep. **3**, 1072 (2013).

[194] C. Busse, P. Lazić, R. Djemour, J. Coraux, T. Gerber, N. Atodiresei, V. Caciuc, R. Brako, A. T. N'Diaye, S. Blügel, J. Zegenhagen, and T. Michely. *Graphene on Ir(111): Physisorption with Chemical Modulation.* Phys. Rev. Lett. **107**, 036101 (2011).

[195] J. A. V. Pomoell, A. V. Krasheninnikov, K. Nordlund, and J. Keinonen. *Ion ranges and irradiation-induced defects in multiwalled carbon nanotubes.* J. Appl. Phys. **96**, 2864–2871 (2004).

[196] *A Simple Sputter Yield Calculator.* https://www.iap.tuwien.ac.at/www/surface/sputteryield .

[197] R. Mark Bradley and H. Hofsäss. *A modification to the Sigmund model of ion sputtering.* J. Appl. Phys **116**, 234304 (2014).

[198] G. Li, A. Luican, J. M. B. Lopes dos Santos, A. H. Castro Neto, A. Reina, J. Kong, and E. Y. Andrei. *Observation of Van Hove singularities in twisted graphene layers.* Nature Phys. **6**, 109–113 (2010).

Darius Constantin Merk

Date of birth: 07/06/1993 | **Nationality:** Swiss | **Gender** Male | (+41) 0792392994 |

dmerkc@gmail.com | 117 chemin des Marionnettes, 1093, La Conversion, Switzerland

About me: I am an open-minded, resourceful positive-thinker with a strong passion for aviation, science, space and drones. I have strong communication skills and am always taking on new challenges, striving to be the best version of myself. I have solid theoretical and experimental skills in a wide range of physical phenomena, an analytical mind with strong problem solving skills and a hands-on approach for building and fixing.

WORK EXPERIENCE

01/06/2017 – CURRENT – Ecublens, Switzerland
PHD CANDIDATE IN PHYSICS – LABORATORY OF NANOSTRUCTURES AT SURFACES, ECOLE POLYTECHNIQUE FÉDÉRALE DE LAUSANNE

We have developed a method to transfer large-area graphene (monoatomic layer of honeycomb-packed carbon) in ultra-high vacuum (UHV) conditions with the aim of enabling the creation of novel multilayered systems that may improve nano-scale technologies, such as single-atom magnets for high-density data storage. In parallel I worked as a teaching assistant, planning and assisting classes of 30 students weekly.
Experimental techniques mastered :
Ultra-High Vacuum, Scanning Tunneling Microscopy, X-ray absorption, Auger and Raman spectroscopy, Chemistry, Cryogenics.

01/01/2012 – CURRENT – Lausanne, Switzerland
MATHEMATICS AND PHYSICS TUTOR (PRIVATE SECTOR) – PRIVATE

I coach high school and secondary students weekly to help them complete their tasks and understand the concepts they are studying by adapting my methodology with respect to each student.
Average grades in math/physics increased by 20-30%.

01/09/2015 – 28/02/2016 – Cheseaux-sur-Lausanne, Switzerland
INTERNSHIP IN INDUSTRIALIZATION, EBEE RISK MANAGEMENT – SENSEFLY

SenseFly is a mapping drone company. My main project was the statistical analysis of the performance of the eBee for a risk assessment, which later facilitated the use of eBee drones around Switzerland. Flight tests of a quadcopter-type drone and quality check procedures on the production line were optimized decreasing the time per unit by 50% and 20% respectively.

02/2016 – 07/2016 – Lausanne, Switzerland
MASTER THESIS : A BIO-INSPIRED COLLISION AVOIDANCE ALGORITHM FOR COLLISION FREE NAVIGATION IN CLUTTERED ENVIRONMENTS – LABORATORY OF INTELLIGENT SYSTEMS, EPFL

We designed and implemented a collision avoidance algorithm on a homebuilt drone equipped with 360° cameras. The algorithm enabled it to successfully navigate in controlled cluttered environments while flying in a target direction.

EDUCATION AND TRAINING

2018 – 2019
PRIVATE PILOT LICENSE – Air-Club Yverdon, LSGY, Switzerland

2014 – 2016
MASTER IN PHYSICS – Ecole Polytechnique Fédérale de Lausanne, Physics Department

123

2011 – 2014
BACHELOR IN PHYSICS – Ecole Polytechnique Fédérale de Lausanne, Physics Department

https://www.coursera.org/learn/machine-learning

● LANGUAGE SKILLS

Mother tongue(s): ENGLISH │ FRENCH

Other language(s):

	UNDERSTANDING		SPEAKING		WRITING
	Listening	Reading	Spoken production	Spoken interaction	
GERMAN	B1	B1	B1	B1	B1
SPANISH	B1	B1	B1	B1	B1

Levels: A1 and A2: Basic user; B1 and B2: Independent user; C1 and C2: Proficient user

● DIGITAL SKILLS

Microsoft Office │ MATLAB&Simulink │ C, C++c C# │ Autodesk Fusion360 │ Machine learning algorithm

● HOBBIES AND INTERESTS

Private pilot

180 hours - SEP - variable pitch propeller, retractable landing gear and tailwheel extensions.

Skydiving and wind tunnel

Since fall 2020 - Completed AFF level 7, 22 solo jumps, 2h wind tunnel.

FPV drone pilot

Building, tuning and racing FPV drones for the past 5 years and built drones for those interested.

Pianist

Quasi-professional level in classical music, played at Conservatoire de Lausanne for 10 years, still play for pleasure

Scooba diving

PADI Open water license.

Sports

Competitive swimming for 12 years, national level, 14 hours weekly training.
Competitive golf at national level at 16 years old, handicap 8.3.
Daily fitness routine.